Fast Trailed Vorticity Modeling for Wind Turbine Aerodynamics and its Influence on Aeroelastic Stability

Pirrung, Georg; Aagaard Madsen , Helge; Kim, Taeseong

Publication date:
2014

Document Version
Publisher's PDF, also known as Version of record

Citation (APA):
Pirrung, G., Aagaard Madsen , H., & Kim, T. (2014). Fast Trailed Vorticity Modeling for Wind Turbine Aerodynamics and its Influence on Aeroelastic Stability. DTU Wind Energy.

Fast Trailed Vorticity Modeling for Wind Turbine Aerodynamics and its Influence on Aeroelastic Stability

Georg Raimund Pirrung

Monday 10 November, 2014

Author: Georg Raimund Pirrung

Title: Fast Trailed Vorticity Modeling for Wind Turbine Aerodynamics and its Influence on Aeroelastic Stability

Department: DTU Wind Energy

The dissertation is submitted to the Technical University of Denmark, in partial fulfilment of the requirements for the obtainment of the PhD degree from the PhD School DTU Wind Energy.
The PhD project was carried out in the years 2011-2014 at the Aeroelastic Design Section of DTU Wind Energy, Department of Wind Energy (formerly Risø DTU, Wind Energy Department). The dissertation was submitted in November 2014.

Main Supervisor:
Helge Aa. Madsen, DTU Wind Energy
Co-Supervisor:
Taeseong Kim, DTU Wind Energy

DTU Wind Energy PhD-xxxx(en)
November 2014

ISBN:
978-87-92896-59-9

pages: 120
tables: 2
figures: 33
references: 34

Technical University of Denmark
DTU Wind Energy
Risø Campus
Frederiksborgvej 399
Building 118
DK-4000 Roskilde
gepir@dtu.dk

Abstract

In this work, an aerodynamic model for the use in aeroelastic wind turbine codes is presented. It consists of a simplified lifting line model covering the induction due to the trailed vorticity in the near wake, a 2D shed vorticity model and a far wake model using the well known blade element momentum (BEM) theory. The model is an extension of unsteady BEM models, which provides a radial coupling of the aerodynamic sections through the trailed vorticity. The model is very fast and slows down aeroelastic wind turbine simulations by only few percent, compared to an unsteady BEM model. Compared to earlier implementations, the model has been improved in several ways: Among other things, the need for model-specific user input has been removed, the effect of downwind convection of the trailed vorticity is modeled, the near wake induction is iterated to stabilize the computations and the numerical efficiency is increased.

The model is validated against results from full rotor CFD and free wake panel code computations, which show that the model yields improved results in steady and unsteady simulations compared to unsteady BEM modeling. Especially the aerodynamic work due to prescribed in-plane and out-of-plane vibrations agrees much better with high fidelity models. Further, the trailed vorticity effects on the aerodynamic work are found to be of the same order of magnitude as the shed vorticity effects. The trailed vorticity effects are, however, mainly important close to the tip in the investigated cases, which is where the major part of the aerodynamic work is generated.

The aerodynamic model is further applied to determine the critical speed of a freely rotating wind turbine rotor with respect to the aeroelastic instability classical flutter. The NREL 5MW reference turbine is used for the computations, but the torsional and flapwise stiffness are varied between 70% and 130% of their original value to obtain more general results. In all computed cases, the trailed vorticity increases the critical rotor speeds by four to ten percent.

Future work is to compute a full load basis using the new aerodynamic model to evaluate the impact of trailed vorticity modeling on fatigue and extreme loads. The model will further be implemented in the aeroelastic stability tool HAWCStab2.

Resumé

Denne afhandling omhandler udvikling af en ny aerodynamisk model, som er implementeret i det aeroelastiske beregningsprogram HAWC2, udviklet ved DTU Vindenergi. Overordnet er modellen en forenklet udgave af en lifting line hvirvelmodel, som normalt anses for at være for beregningstung til at indgå i et aeroelastisk program. Modellen beregner induktionen ud fra tre bidrag: 1) fra hvirvelsystemet i nærkølvandet; 2) fra en 2D model for Theodorsen effekter (shed vorticity) og 3) fra en model baseret på blade element momentum (BEM) teori, der beregner induktionen fra resten af kølvandet. Den nye model giver en radial kobling mellem de aerodynamiske vingesektioner gennem hvirvelsystemet til forskel fra den normalt benyttede BEM model, hvor induktionen i de enkelte sektioner er uafhængige af hinanden. Modellen kører meget hurtigt og nedsætter kun beregningstiden for aeroelastiske beregninger med få procent sammenlignet med en instationær BEM model. I forhold til tidligere implementeringer er modellen blevet forbedret på en række områder. Blandt andet er behovet for model-specifik bruger input blevet fjernet, og hvirvlerne antages ikke længere at forblive i rotorplanet. Nærkølvandets induktion bliver itereret, hvilket stabiliserer beregningerne og øger den numeriske effektivitet.

Modellen er valideret med resultater fra rotor CFD beregninger og fra en mere kompleks vortex panel kode. Valideringen viser, at den nye model giver nøjagtigere resultater i forskellige simulationer sammenlignet med BEM modellen. Især det beregnede aerodynamiske arbejde på grund af vibrationer af vingerne er i bedre overensstemmelse med de mere avancerede modeller. Beregningen af nærkølvandet i den nye model har vist sig at være vigtigt især tæt på vingespidserne.

Den aerodynamiske model er yderligere anvendt til at bestemme den kritiske hastighed af en frit roterende vindmølle med hensyn til den aeroelastiske ustabilitet, der kaldes klassisk flutter. Beregningerne er foretaget på NREL 5 MW møllen, men vridnings- og flapvis stivhed er varieret mellem 70 % og 130 % af deres oprindelige værdi, for at få mere generelle resultater. Modelleringen af hvirvelsystemet i nærkølvandet øger den kritiske rotorhastighed med fire til ti procent.

Preface

This dissertation has been prepared in the time period from November 2011 to October 2014. It is a partial fulfillment of the requirements for the degree of Doctor of Philosophy in Engineering at the Technical University of Denmark (DTU).

The work has been supervised by research specialist Helge Aagaard Madsen, associate professor Taeseong Kim, and, during the first 14 months, professor Morten Hartvig Hansen, all affiliated with the DTU Wind Energy Department.

The thesis is mainly based on four scientific papers. The work in two of these papers has been presented at the conferences 'The Science of Making Torque from Wind' in the years 2012 and 2014, while the other papers have been submitted to the international journal 'Wind Energy'. The papers are referred to by roman numbers:

I Pirrung GR, Hansen MH, Madsen HA. *Improvement of a near wake model for trailing vorticity*, Proceedings of the science of making torque from wind, Oldenburg, 2012.

II Pirrung GR H A Madsen, Kim T, Heinz J. *A Coupled Near and Far Wake Model for Wind Turbine Aerodynamics*, submitted, September 2014.

III Pirrung GR, Riziotis V, Madsen HA, Hansen MH, Kim T. *Comparison of a Coupled Near and Far Wake Model With a Free Wake Vortex Code*, submitted, November 2014.

IV Pirrung GR, Madsen HA, Kim T. *The influence of trailed vorticity on flutter speed estimations*, Journal of Physics: Conference Series (Online) 2014; 524, doi:10.1088/1742-6596/524/1/012048.

Acknowledgements

I would like to thank my supervisors Helge and Taeseong for the discussions, reviews, support and guidance in the last years. I further want to thank my part-time supervisor and project initiator Morten for getting me started and for reviewing my work with unparalleled honesty and attention to detail. Thank you to Vasilis for the great collaboration and to Joachim for providing the CFD results.

I also have to say that the work atmosphere here at DTU Wind Energy has been absolutely outstanding due to a lot of other great people, among them: Carlo, Leo, Andreas, Alex, David, Witold, the Colombian Juan, the other Colombian Juan, Pierre and Paul. Actually, David deserves to be thanked again for sharing his thesis template. I would also like to thank Mac for demonstrating that you can be a great scientist and musician at the same time!

It would have been very difficult to go through three years without great company (including great food and drinks!) at home. I have been fortunate to live with very nice people in the two incarnations of 'The House', such as Susana, Thomas, Geoffrey, Zuzana, Andrew, Sebastian, Laia, Yannick, Moritz and Isabell.

I am also very thankful for the distractions provided by the rest of the Friday Bar team, Anna and Jay, and the fellow krachmachers at KLUBB, Copenhagen showband and discourse bigband.

Last but definitely not least I want to thank my parents and my sister for their continuous love and support and for even trading the warmth of southern Germany (and, well, the Netherlands...) for the Danish weather just to come and visit!

Contents

CHAPTER 1

Introduction

1.1 Motivation

The development of wind turbines is focused on reducing the cost of energy. This focus has led to an increase in wind turbine rotor size in the last decades while keeping the blade mass and stiffness relatively low. To further develop efficient blade designs, the aeroelastic load computations need to become more accurate, which includes a requirement for improved aerodynamic models [1]. The aerodynamic forces can be computed with a high accuracy using advanced models, such as free wake codes, [2], or full rotor CFD [3, 4]. However, to certify a modern turbine, a large number of load cases with varying conditions has to be computed [5]. Many of these simulations require a simulated time of 600 seconds, therefore it is, even with the currently available computational resources, not possible to compute a load basis using high fidelity models. Fast aerodynamic models are needed, which are mainly based on blade element momentum (BEM) theory.

With the longer and more flexible blades comes an increased risk of a self-induced vibrations, mainly classical flutter [6–8]. Also backward sweep for additional flap-torsion coupling with the purpose of passive load reduction has been found to reduce the critical rotor speed at which flutter occurs [9]. Further, edgewise modes can exhibit low or even negative aeroelastic damping even in normal operating conditions for modern, pitch-regulated turbines [6]. These issues can be investigated using linear aeroelastic models of wind turbines [9–11], which also require simple aerodynamic modeling.

The unsteady BEM models of current aeroelastic wind turbine codes include a dynamic inflow model, which is essentially a low pass time filter modeling the wake dynamics [12], and 2D unsteady airfoil aerodynamics models. These model the so-called 'Theodorsen effect' [13], a delayed aerodynamic force response to airfoil motion due to vorticity shed into the wake, and dynamic stall, which denotes a delay in separation and reattachment of the unsteady flow at high angles of attack. Tip loss effects due to trailed vorticity are usually modeled by a tip loss factor [14].

This state of the art fast aerodynamic modeling has several shortcomings: the BEM theory assumes that the rotor is divided into concentric annular elements that are not coupled through the aerodynamics. Therefore a section of the blade would not notice if for example a neighboring flap is moving or a neighboring part of the blade is subject to variations of the incoming flow velocity due to atmospheric turbulence. In reality, the trailed vorticity due to these disturbances would lead to an effect that is felt on the whole blade [15]. Moreover, large radial loading gradients, for example due to partial pitch or aerodynamic devices on the blade, result in locally trailed vorticity. This vorticity causes a force distribution along the blade that can not be computed using a BEM model. Also the dynamics of the tip vortex induction are not accurately modeled by applying a tip loss factor on the thrust, that is then driving the dynamic inflow model.

In this work, these shortcomings are adressed by further development of an aerodynamic model combining an unsteady BEM method for the far wake induction with trailed vorticity computations according to a model by Beddoes [16, 17]. The model is fast enough to be used for load computations in aeroelastic wind turbine codes and can be written in state space form to be applied in stability computations in the future.

1.2 Outline

This thesis is structured as follows:

In the next chapter, a brief overview of the state of the art of fast aerodynamic modeling for aeroelastic wind turbine computations is presented, including a description of the previous implementation of the coupled near and far wake model.

In Chapter 3, the aerodynamic model developed in the course of the PhD study is described in detail. The chapter is a summary of the respective sections in manuscripts [II-IV].

Chapter 4 is a comparison of steady state results from the coupled near and far wake model with results from a BEM model and full rotor CFD computations. The chapter is based on manuscripts [I] and [II].

Chapter 5 presents the validation of the model against unsteady BEM models and the free wake panel code GENUVP for pitch step and prescribed vibration cases. These validations are described in more detail in [III]. However, additional results of an unsteady BEM model without unsteady airfoil aerodynamics computations are added to better compare the trailed vorticity effects with the shed vorticity effects. Further, the chapter contains new results of full rotor CFD computations in selected cases.

The influence of trailed vorticity on the critical rotor speeds of the NREL 5 MW reference turbine has been investigated in [IV], and the main findings are shown in Chapter 6.

The conclusions of the work conducted during this PhD project are presented in Chapter 7.

The manuscripts [I-IV] are included in full length in the appendix.

CHAPTER 2

State of the art in fast aerodynamics modeling

In the first section of this chapter a short overview of fast aerodynamic models for wind turbines is given. Because the chapter is meant to act as a basis for the modified aerodynamic model presented in the next chapter, some details of the modeling are specific to the aeroelastic wind turbine code HAWC2 [18–20]. The different components of the aerodynamic model, meaning the BEM equations, the dynamic inflow modeling and the unsteady aerodynamics model, are used in similar implementations in all BEM based aeroelastic wind turbine codes. Therefore, the model developed in this work should be generally applicable. The sections on dynamic inflow and unsteady airfoil aerodynamics are based on [III].

The second section of this chapter the main features of previous implementations of the coupled near and far wake model are described to provide the basis for the work conducted during this PhD. This description is a compilation of the corresponding sections in [II] and [III].

2.1 Unsteady BEM theory

2.1.1 BEM basics

In blade element momentum theory, it is assumed that the rotor can be subdivided in annular sections. Each section of the rotor is exerting a force on only the corresponding stream tube of air and does not interact with the other sections through the aerodynamics. This force slows the air down, and the out-of-plane velocity of the air v_{oop} at the rotor plane is defined using a so-called axial induction factor a:

$$v_{oop} = v_\infty(1 - a) + v_{oop,b}, \tag{2.1}$$

where v_∞ is the free wind speed. The velocity $u = v_\infty a$ is known as the axial induced velocity. The velocity $v_{oop,b}$ denotes the movement of a flexible blade in the out-of-plane direction, thus it will only be relevant for application in an aeroelastic wind turbine code. A corresponding tangential induction factor a' is defined such that:

$$v_{ip} = \Omega r_s(1 + a') + v_{ip,b}, \tag{2.2}$$

where v_{ip} is the in-plane velocity component, Ω the rotor speed in [rad/s], r_s the radial position of the investigated blade section and $v_{ip,b}$ the velocity due to blade deformation. Note that v_{ip} denotes only the velocity component perpendicular to the blade axis.

From these velocities follow the inflow angle φ, the angle of the flow relative to the rotor plane, the relative velocity v_r and the quasi-steady angle of attack α_{QS} at the blade section

$$\tan\varphi = \frac{v_{oop}}{v_{ip}}, \quad v_r = \sqrt{(v_{oop})^2 + (v_{ip})^2} \tag{2.3}$$

$$\alpha_{QS} = \varphi - \theta, \tag{2.4}$$

where θ denotes the sum of blade pitch and twist, as well as torsional deformation. The quasi-steady lift L, drag D and moment M can be determined from α_{QS} and v_r as:

$$L_{QS} = \frac{\rho}{2} c v_r^2 C_{L,QS}, \quad D_{QS} = \frac{\rho}{2} c v_r^2 C_{D,QS}, \quad M_{QS} = \frac{\rho}{2} c^2 v_r^2 C_{M,QS}, \tag{2.5}$$

where $C_{L,QS}$, $C_{D,QS}$ and $C_{M,QS}$ are airfoil specific lift, drag and moment coefficients that are functions of α_{QS} and usually determined by table look-up. Further, ρ is the air density and c the chord length.

The sectional out-of-plane force, the thrust per meter blade radius dT, has a component due to the airfoil lift and drag, depending on the inflow angle,

$$dT = \frac{\rho}{2} c N_B v_r^2 C_{oop}, \quad \text{where} \tag{2.6}$$

$$C_{oop} = C_L \cos\varphi + C_D \sin\varphi. \tag{2.7}$$

In the above equation, it is assumed that the relative velocities are identical at all blades and N_B denotes the number of blades. The quotient of this force over the dynamic pressure of the incoming air at the blade section is the so-called thrust coefficient C_T.

$$C_T = \frac{dT}{\frac{\rho}{2} v_\infty^2 2\pi r} = \frac{v_r^2 c N_B C_{oop}}{2\pi r v_\infty^2} \tag{2.8}$$

Because the thrust coefficient is a measure of the force exerted on the incoming air flow by the rotor section, there is a relation between the thrust coefficient and the induced velocity, which described how much the velocity of the air decreases when passing through the rotor disc.

For inductions $a < 1/3$, the induction can be found as a function of the thrust coefficient as

$$C_T = 4a(1 - a). \tag{2.9}$$

This equation is not valid for higher induction values, where empirical relations are used instead [1].

In the aeroelastic wind turbine code HAWC2, the axial induced velocity u_{QS} is computed based on a BEM model that uses a polynomial to relate the thrust coefficient with the axial induction factor:

$$u_{QS} = u_\infty a \tag{2.10}$$

$$a = k_3(C_T/F)^3 + k_2(C_T/F)^2 + k_1(C_T/F), \tag{2.11}$$

where F is the tip loss factor taking into account the finite number of blades [14]. The coefficients k_i have been determined to provide an approximation for the induction at low thrust according to BEM theory and the Glauert correction at high thrust. They are $k_3 = 0.08921$, $k_2 = 0.05450$ and $k_1 = 0.25116$.

The induced velocity from Equation (2.11) leads to a new velocity triangle, Equation (2.3) and thus a new thrust coefficient and induction factor. To find the steady state induced velocities, an iteration scheme would be necessary. In aeroelastic wind turbine codes for time series computations, the iteration is not necessary, instead a low pass time filter is commonly applied on the induced velocities to model the unsteady behavior of the wind turbine wake.

2.1.2 Dynamic inflow modeling

Because the wind turbine wake does not react immediately, a so-called dynamic inflow model is applied to the induced velocities according to BEM theory [12]. This work uses the dynamic inflow model used in HAWC2, where two parallel first order low pass filters are applied on the quasi steady induced velocities $u_{QS} = au_\infty$ from the BEM model, [21]:

$$u^i_{dyn} = A_1 u^i_1 + A_2 u^i_2 \tag{2.12}$$

$$u^i_1 = u^{i-1}_1 e^{-\Delta t/\tau_1} + u^i_{QS}(1 - e^{-\Delta t/\tau_1}) \tag{2.13}$$

$$u^i_2 = u^{i-1}_2 e^{-\Delta t/\tau_2} + u^i_{QS}(1 - e^{-\Delta t/\tau_2}), \tag{2.14}$$

where the factors $A_1 = 0.6$ and $A_2 = 0.4$ are applied to divide the induction into a faster and slower reacting part, corresponding to a faster time constant τ_1 and the slower time constant τ_2. Both time constants are a function of the position of the blade section defined by the radius r_s and mean rotor induction:

$$\tau_1 = \tau^* \frac{1.8R}{v_\infty \mathrm{MIN}\left[1 + 3\frac{u_{FW,QS}}{v_\infty}, 2.0\right]}, \tag{2.15}$$

$$\tau_2 = \tau^* \frac{R}{v_\infty \mathrm{MAX}\left[1 - 3\frac{u_{FW,QS}}{v_\infty}, 0.2\right]}, \tag{2.16}$$

$$\tau^* = k_2(\frac{r_s}{R})^2 + k_1(\frac{r_s}{R}) + k_0, \tag{2.17}$$

where R is the radius of the wind turbine rotor.

The constants A_i and τ_i have been tuned to the actuator disc simulations of step changes in uniform loading [22].

Induction grid

In the BEM and dynamic inflow models presented in the previous sections, a uniform inflow has been assumed, as well as uniformity in the motion of the individual blades. This case never occurs in reality, and the non-uniformity of the inflow and the blade motion, for example due to wind shear, yaw error, rotor whirling modes and cyclic or individual pitch control has to be taken into account in the computations.

Different BEM implementations follow different approaches to enable a non-uniform induces velocity at the rotor [23]. In HAWC2, the induced velocities are calculated on an induction grid, that divides the annular elements used in BEM theory with lines of constant azimuth angle [21], as shown in Figure 2.1. The induced velocities are computed at each individual grid point, following this procedure:

1. The wind speed at the grid point is determined.
2. The two wind turbine blades closest to the grid point are found.
3. Two thrust coefficients, cf. Equation (2.8), are computed using the relative speeds, pitch and twist angles of both of these closest blades and the dynamic induction at the grid point.
4. The thrust coefficients are azimuthally averaged at the grid point location.
5. The average thrust coefficient leads to the induced velocity, cf. Equation (2.11).
6. This induced velocity at this grid point is time filtered according to the dynamic inflow model presented before, based on rotor wide mean induction and free wind speed.

2.1.3 Unsteady airfoil aerodynamics modeling

If the AOA at an airfoil section changes, the aerodynamic forces are not immediately reaching their steady values [15, 24]. Instead, the time gradient of the bound circulation of the airfoil, which is related to the lift, causes vorticity to be shed into the wake of the airfoil. This shed vorticity delays the variation of the AOA at the airfoil; an effect that is commonly modeled in aeroelastic wind turbine codes by means of low pass filters. The sketch in Figure 2.2 illustrates how the shed vorticity due to the time variation of the bound circulation induces a downwash $w_{3/4}$ at the three quarter chord point, the so-called collocation point, of an airfoil. This downwash will change the angle of attack and thus the lift, drag and moment coefficients according to the airfoil polars, as well as the directions of the aerodynamic forces. The inviscid part of the unsteady airfoil aerodynamics model in Hansen et al. [25] treats the shed vorticity effects as a time lag on the angle of attack according to Jones' function for a flat plate [26]. Jones' function is valid for airfoil motion, which means that the whole flow field changes relative to the airfoil. When computing the variations of AOA due to atmospheric turbulence, another function should be applied, for example Kuessner's function for a sharp-edged gust [15]. This is not relevant for the cases investigated in this work, but for loads simulation it will have an impact, although it is estimated to be of minor importance

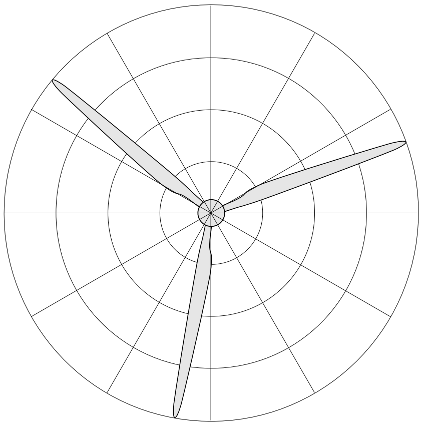

Figure 2.1: Scheme of the induction grid in HAWC2.

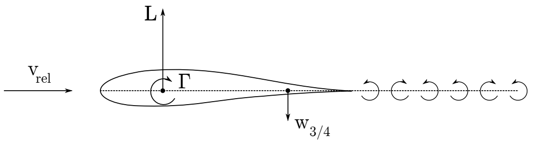

Figure 2.2: Cambered airfoil in parallel inflow to the chord line.

by Buhl et al. [27].

In [25], the effective angle of attack α_{eff}, which determines the magnitude and direction of the unsteady aerodynamic forces, is computed as:

$$T_0^i = \frac{c}{2v_{rel}^i} \tag{2.18}$$

$$x_1^i = x_1^{i-1} e^{-0.0455\frac{\Delta t}{T_0^i}} + \frac{1}{2}(\alpha_{QS}^i + \alpha_{QS}^{i-1})0.165 v_{rel}^i (1 - e^{-0.0455\frac{\Delta t}{T_0^i}}) \tag{2.19}$$

$$x_2^i = x_2^{i-1} e^{-0.3\frac{\Delta t}{T_0^i}} + \frac{1}{2}(\alpha_{QS}^i + \alpha_{QS}^{i-1})0.335 v_{rel}^i (1 - e^{-0.3\frac{\Delta t}{T_0^i}}) \tag{2.20}$$

$$\alpha_{eff}^i = \frac{1}{2}\alpha_{QS}^i + (x_1^i + x_2^i)/v_{rel}^i, \tag{2.21}$$

where the superscript i denotes the time step, α_{QS} is the quasi steady angle of attack resulting from the velocity triangle at the blade section and v_{rel} denotes the corresponding relative velocity.

2.2 Previous work on coupled near and far wake model

The structure of the previous implementation, [17, 28], of the coupled near and far wake model is shown in Figure 2.3. From the velocity triangle, denoted as VT, follows a geometric angle of attack (AOA) α_{QS} and a relative velocity v_r. An effective AOA α_{eff} is obtained through a 2D modeling of the shed vorticity effects, as described in the previous section. This effective AOA is used to determine the aerodynamic forces and the thrust coefficient C_T. In Section 2.2.2 will be shown how the thrust coefficient leads to a far wake induction factor a_{FW}, requiring a coupling factor k_{FW} as input.

Using this far wake induction, and the near wake induction from the previous time step, a new quasi steady AOA and relative velocity are determined. These lead to the bound circulation Γ_{QS}. The difference in Γ_{QS} between adjacent blade sections, denoted as $\Delta\Gamma$ in the following, determines the trailed vorticity. In the next section is shown how the induced velocity W due to the near wake, which is added to u_{FW} to obtain the total induced velocity at each blade section, follows from the trailed vorticity.

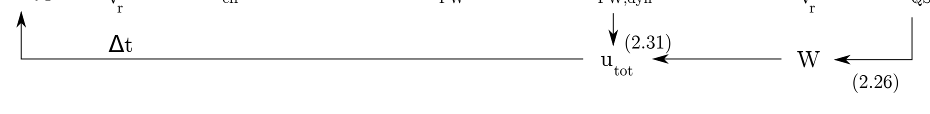

Figure 2.3: The previous implementation of the coupled near and far wake model, as described by Madsen and Rasmussen [17] and Andersen [28]. Relevant equation numbers and references are included. Adapted from [III].

2.2.1 Near wake model by Beddoes

The purpose of the near wake model (NWM) is to approximate the induction at a blade due to the vorticity trailed from that blade in a quarter of a rotor revolution. To make an efficient computation possible, Beddoes [16], assumes that the trailed vorticity follows prescribed circular arcs in the rotor plane. Using the Biot-Savart law, the induction dw from a vortex element with the length ds on a circular arc trailed at radius r at a point on the blade at a distance h from the vortex trailing point, cf. Figure 2.4 can be found as:

$$dw = \frac{\Delta\Gamma ds}{4\pi r^2} \frac{1-\left(1-\frac{h}{r}\right)\cos(\beta)}{\left[1+\left(1-\frac{h}{r}\right)^2 - 2\left(1-\frac{h}{r}\right)\cos(\beta)\right]^{3/2}}, \tag{2.22}$$

where $\beta = \Omega t$ is the angle the blade has moved since the element has been trailed. Equation (2.22) is derived in Section 3 for the more general case including downwind convection. To obtain the induction from a vortex arc, Equation (2.22) could be integrated numerically. But it is very expensive to obtain the induction from the trailed wake along the blade in this way: If the blade is discretized into n sections, and $n+1$ vortices are trailed at the root and tip of the blade and in between the sections, $n(n+1)$ integrations of Equation (2.22) are necessary to obtain the induction due to every trailed vortex arc at every blade section.

A fast trailing wake algorithm has been developed by Beddoes to speed up these integrations. The basic idea is to compute the induction from a vortex element at the lifting line and let that value decrease as the blade rotates away from that element. This decay of the induction can then be efficiently computed using exponential functions. The induction from an element at the lifting line follows directly from Equation (2.22):

$$dw_0 = dw(\beta = 0) = \frac{\Delta\Gamma ds}{4\pi r^2} \frac{1-\left(1-\frac{h}{r}\right)}{\left[1+\left(1-\frac{h}{r}\right)^2 - 2\left(1-\frac{h}{r}\right)\right]^{3/2}} = \frac{\Delta\Gamma r d\beta}{4\pi h|h|}. \tag{2.23}$$

The spatial decay function that gives the fraction of the induction from an element of its value at the lifting line is obtained through division of Equation (2.22) by (2.23).

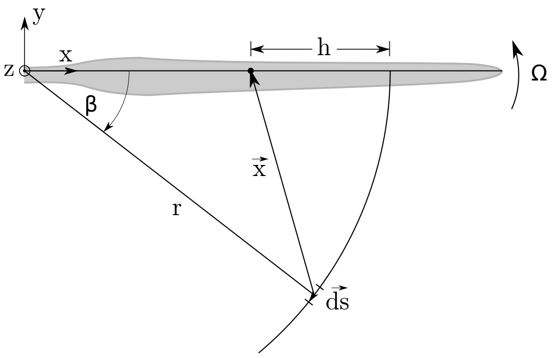

Figure 2.4: Sketch of the blade geometry with vorticity trailed at radius r. Since the vortex element $\vec{ds}$ has been trailed the blade has moved by an angle β at the angular velocity Ω. The induction is to be computed at a blade section the distance h inboard from the vortex trailing point. Figure from [II].

Beddoes proposed to approximate it using exponential functions:

$$\frac{dw}{dw_0} = \frac{\left(\frac{h}{r}\right)^2 \left[1 - \left(1 - \frac{h}{r}\right)\cos(\beta)\right]}{\left[1 + \left(1 - \frac{h}{r}\right)^2 - 2\left(1 - \frac{h}{r}\right)\cos(\beta)\right]^{3/2}} \approx 1.359e^{-\beta/\Phi} - 0.359e^{-4\beta/\Phi}, \tag{2.24}$$

where Φ is a geometrical factor depending on r and h. In this work, an improved definition of Φ by Wang and Coton [29] is used. This definition leads to a reduced error if the vortices are trailed further inboard than the blade section where the induction shall be computed, which is defined as $h/r < 0$.

$$\Phi = \frac{\pi}{4}\left|\left(1 + \frac{h}{2r}\right)\ln\left(1 - \frac{h}{r}\right)\right| \qquad \text{for } 0 < h/r < 1 \tag{2.25a}$$

$$\Phi = \frac{1 - \frac{h}{r}}{1.5 + \ln(1 - \frac{h}{2r})} \qquad \text{for } h/r < 0. \tag{2.25b}$$

The trailing wake algorithm proposed by Beddoes determines the near wake induction W at a point on the blade at a given time step i as:

$$W^i = X_w^i + Y_w^i, \tag{2.26}$$

with the slowly decaying component X_w and the faster decaying component Y_w. The value of these components depends both on their values at the previous time steps, which are decreasing during a time step according to the exponential functions, and the new contributions D_w from the vortex element trailed in the time step:

$$X_w^i = X_w^{i-1}e^{-\Delta\beta/\Phi} + 1.359D_w e^{-\Delta\beta/2\Phi} \tag{2.27a}$$

$$Y_w^i = Y_w^{i-1}e^{-4\Delta\beta/\Phi} - 0.359D_w e^{-2\Delta\beta/\Phi}. \tag{2.27b}$$

Assuming a straight element perpendicular to the lifting line and applying the Biot-Savart law, the induction due to the new element trailed during the time step is found as:

$$D_w = \frac{\Delta\Gamma\left(\frac{\Delta s}{|h|}\right)}{4\pi h\left[1 + \left(\frac{\Delta s}{h}\right)^2\right]^{1/2}}. \tag{2.28}$$

Exponential functions evaluated at half a time step are used to determine the fractions of D_w driving the faster and slower decaying parts of the induction in Equations (2.27). The resulting fractions of D_w are added to the decreased contributions from all previous components included in X_w^{i-1} and Y_w^{i-1}.

To account for the movement of the vortices out of the rotor plane in the presence of downwind convection, Wang and Coton [29] introduced the angle φ of the helix formed by the trailed vortex filaments in the calculation of D_w, which is identical to the inflow angle. Andersen [28] proposed to model the tangential induction in a corresponding way as the axial induction:

$$D_{w,a} = D_w\cos(\varphi), \quad \text{and} \tag{2.29}$$

$$D_{w,t} = D_w\sin(\varphi). \tag{2.30}$$

The subscripts a and t denote the axial and tangential induction. The values for the induction from the first element are then inserted in Equations (2.27) replacing D_w.

2.2.2 Far wake model

The NWM, which only computes a fraction of the total rotor induction, is complemented by a modified BEM model for the far wake. The total induced velocity at a blade section is computed as

$$u_{tot} = u_{FW} + W, \tag{2.31}$$

where u_{FW} is the far wake component of the induced velocity and W is the near wake component, cf. Equation (2.26).

To avoid to account multiple times for the near wake induction, the far wake model is not using a tip loss correction and it is based on a thrust coefficient C_T that is reduced by the coupling factor k_{FW} [17]. The quasi steady far wake induction factor is thus found as:

$$a_{FW}(C_T) = k_3(k_{FW}C_T)^3 + k_2(k_{FW}C_T)^2 + k_1(k_{FW}C_T), \tag{2.32}$$

where k_{FW} has been provided as input from a large amount of preliminary simulations [28].

The previous implementations used the dynamic inflow model as in HAWC2, treating the far wake induction in the same way as the induction from the BEM model.

CHAPTER 3

Model description

This chapter is a synopsis of manuscripts [II,III,IV], where different parts of the model have been described. The structure of the current implementation of the coupled near and far wake model is shown in Figure 3.1. The changes to the previous implementation, cf. Figure 2.3 are:

- The computation of α_{eff} according to shed vorticity effects is improved for cambered airfoils, which is explained in Section 3.1.
- The coupling factor is no longer needed as input, but instead continually updated during the computation, as described in Section 3.2.1
- The weighting factors A_i of the far wake dynamic inflow are adjusted during the computation to account for the induction computed by the near wake model, which is explained in Section 3.2.2.
- Several modifications of the near wake model are presented in Section 3.3:
  - The trailed vorticity is no longer based on the quasi steady bound circulation Γ_{QS}, but instead on a dynamic bound circulation Γ_{dyn}. The computation of the dynamic bound circulation is shown in Section 3.3.1.
  - The trailing functions have been improved so that the results are less time step dependent and the computation is more efficient, which is described in Section 3.3.2.
  - The accuracy of the induced velocities close to the blade root due to the tip vortex has been improved, which is shown in Section 3.3.3.
  - The trailed vorticity is assumed to follow helix arcs to account for the downwind convection of the trailed vorticity. To achieve this, Φ, Equation (2.25), is multiplied with a correction function f, depending on the blade section and vortex trailing point, as well as the helix angle at which the vortex is trailed. The details of this modification are given in Section 3.3.4.
  - It is shown in Section 3.3.5 how the near wake model has been accelerated by simplifying Beddoes' approximation of the Biot-Savart law.
  - The near wake induction is computed in an iteration loop, which is detailed in Section 3.4.

3.1 Influence of camber on the unsteady airfoil aerodynamics

When determining the effective angle of attack, cf. Section 2.1.3, any change in bound circulation Γ, which is a function of $v_{rel}C_L$, as described in Section 3.3.1, should lead to the corresponding shed vorticity. The implementation of the shed vorticity model according to Hansen et al. [25], cf. Equations (2.19-2.21), is based on the term $\alpha_{QS}v_{rel}$. The camber of the airfoil is neglected in this computation of the shed vorticity effects. In the present model,α_{QS} in Equations (2.19 to 2.21) is replaced by $\alpha_{QS,camber}$, with

$$\alpha_{QS,camber} = \alpha_{QS} - \alpha_0, \tag{3.1}$$

where α_0 is the zero lift angle of the airfoil. The effect of this modification is demonstrated for the basic cases of a step change and an oscillation of the relative velocity of an airfoil section similar to the outboard region of the NREL 5MW blades in [III]. The induced drag caused by the shed vorticity due to airfoil camber is found to be of the same order of magnitude as the viscous drag in case of the relative velocity oscillation.

3.2 Modifications of the far wake model

3.2.1 Determining the coupling factor

Because different operating conditions change the ratio of induction from the near and far wake, the coupling factor k_{FW}, cf. Section 2.2.2, is not constant. An example for this is the operation of a turbine above rated wind speed. If the wind speed increases, the helical pitch angle increases. This has a bigger influence on the induction from the far wake than from the near wake, therefore the coupling factor decreases.

Andersen [28] has proposed to compute the coupling factor beforehand for each turbine in a number of cases with varying tip speed ratio and thrust coefficient, but in [II] a different approach is suggested to avoid these preliminary computations: in each time step, in addition to compute the axial far wake induction with reduced thrust coefficient, a second reference BEM induction with complete thrust coefficient and tip loss correction are computed. This reference BEM induction a_{ref} is the induction following from Equation (2.11). The objective is to choose a coupling factor for each blade section, so that the induction predicted by the coupled near and far wake model matches the induction predicted by a BEM model for the same thrust coefficient:

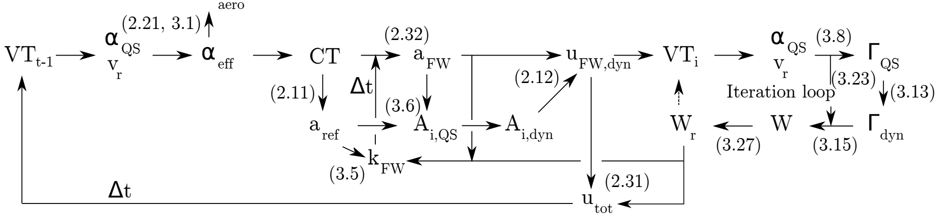

Figure 3.1: Overview of one time step in the coupled near and far wake model used in this work, adapted from [III]. Relevant equation numbers and references are included.

$$a_{ref,QS} = a_{FW,QS} + a_{NW}, \tag{3.2}$$

where quasi steady values of the far wake and reference induction are used to reduce slow changes of the coupling factor due to the different dynamic behavior of the BEM model and the coupled model. The near wake induction reacts faster than the far wake induction and thus the dynamic near wake induction is used for the computation of the coupling factor.

A new value for the coupling factor k_{FW} can be determined every time step for each blade section with the goal of fulfilling Equation (3.2) as:

$$k^{i+1}_{FW,j} = k^{i}_{FW,j} + \frac{a_{ref,QS,j} - (a_{FW,QS,j} + a_{NW,j})}{\partial a / \partial k_{FW}}, \quad \text{with} \tag{3.3}$$

$$\partial a / \partial k_{FW} = 3k_3 C_T^3 k_{FW}^2 + 2k_2 C_T^2 k_{FW} + k_1 C_T, \tag{3.4}$$

where the subscript j indicates the blade section. A time lag with the same time constant as the near wake part of the dynamic inflow model used in HAWC2 is applied on the coupling factors to avoid introducing numerical instabilities. If these sectional coupling factors were used in the coupled model, the induction along the blade would reach the same distribution as with the BEM model with tip loss correction. Since one purpose of using the coupled model is to achieve an induction distribution due to the whole trailed vortex system including the tip vortex, an average coupling factor is used for the entire blade. In order to closely match the complete thrust of a BEM computation, the coupling factors are averaged weighted by the sectional thrust forces:

$$k_{FW} = \frac{\sum_{j=1}^{n} (k_{FW,j} dT_j)}{\sum_{j=1}^{n} dT_j}. \tag{3.5}$$

Further, before averaging a maximum for the sectional coupling factor of 1.0 and a minimum of 0.5 has been implemented, to limit the influence of sections close to strong trailed vorticity on the whole blade.

With the approach presented here preliminary runs to determine the coupling factor can be avoided. The necessary additional computation time is very small, since the reference induction value is not subject to dynamic inflow or shed vorticity effects and is not used to calculate any aerodynamic forces or the velocity triangle.

3.2.2 Adapting the dynamic inflow model

The far wake model only accounts for a part of the full induction. However, the dynamic inflow model described in Section 2.2.2 has been tuned to fit measurements and computations [22]. Therefore the coupled model should achieve a similar slow dynamic inflow response as the unsteady BEM model, which requires a modification of the dynamic inflow model.

In [III], a modification of the constants A_1 and A_2 in Equation (2.12) has been presented. The new constants $A_{i,FW}$ are computed based on the far wake induction factor a_{FW} from Equation (2.32) and the reference induction factor a_{ref}, Equation (2.11). The weighting constants for the far wake model are determined such that roughly 40 %

of the total induction are considered to be reacting slowly, as in the original dynamic inflow model for BEM computation, Equation (2.12):

$$A_{1,FW} = \frac{0.4a_{ref}}{a_{FW}} \tag{3.6}$$

$$A_{2,FW} = 1 - A_{1,FW}. \tag{3.7}$$

The factors are continuously updated during the computations. A first order low pass filter with the far wake time constant τ_2 of the dynamic inflow model is applied on $A_{1,FW}$ to make sure this model does not introduce unphysical rapid induction variations due to instantaneous changes of the weighting factors.

3.3 Modifications of the near wake model

3.3.1 Unsteady circulation modeling

The influence of shed vorticity on the bound circulation buildup has to be considered when determining the strength of the trailed vortices of the NWM. Joukowski's relation between quasi steady lift L_{QS} and circulation Γ_{QS},

$$\Gamma_{QS} = \frac{L_{QS}}{\rho v_r} = \frac{1}{2} v_{rel} c C_L, \tag{3.8}$$

which has been used by Madsen and Rasmussen [17] and Andersen [28] to determine the bound vorticity, is not valid for unsteady conditions. The error of calculating the circulation based on the unsteady lift at an airfoil section depends on the reduced frequency $k = \omega c/(2v_{rel})$, where ω is the angular frequency, c is the chord length, and v_{rel} is the relative flow speed. For an airfoil pitching harmonically about the three-quarter chord point, the error has been estimated by Madsen and Gaunaa [30] to be 10% at $k = 0.1$ and 100 % at $k = 0.8$, which for the NREL 5 MW reference turbine at rated wind and rotor speed corresponds to frequencies of about 1.2 and 9.8 Hz at 60 m rotor radius with a chord of 2 m. Except for the first flapwise and edgewise bending frequencies, most relevant modal frequencies for modern blades are between these values, which shows that it is important to include a modeling of the unsteady circulation.

The step response of the circulation is approximated by the three term indicial function used in Madsen and Gaunaa [30].

$$\Gamma_{dyn}/\Gamma_{QS} = 1 - A_{\Gamma,1}e^{-b_{\Gamma,1}\tau} - A_{\Gamma,2}e^{-b_{\Gamma,2}\tau} - A_{\Gamma,3}e^{-b_{\Gamma,3}\tau}, \quad \text{where} \tag{3.9}$$

$$\tau = \Delta t\frac{2v_{rel}}{c}, \quad A_{\Gamma,1} = 0.5547, \quad A_{\Gamma,2} = 0.1828, \quad A_{\Gamma,3} = 0.2656, \tag{3.10}$$

$$b_{\Gamma,1} = 0.3064, \quad b_{\Gamma,2} = 0.0439, \quad b_{\Gamma,3} = 3.227. \tag{3.11}$$

The algorithm is implemented analogue to the computation for the effective angle of attack in Equations (2.18)-(2.21):

$$x^i_{\Gamma,j} = x^{i-1}_{\Gamma,j} e^{-b_{\Gamma,j}\frac{\Delta t}{T^i_0}} + \frac{A_{\Gamma,j}}{2}(\Gamma^i_{QS} + \Gamma^{i-1}_{QS})(1 - e^{-b_{\Gamma,j}\frac{\Delta t}{T^i_0}}) \tag{3.12}$$

$$\Gamma^i_{dyn} = x^i_{\Gamma,1} + x^i_{\Gamma,2} + x^i_{\Gamma,3}, \tag{3.13}$$

where the quasi steady circulation is computed from the quasi steady lift using Equation (3.8).

3.3.2 Improved trailing functions

The contribution from the newest element can be computed by integrating Beddoes' approximation function, Equation (2.24), over the length of the element.

$$\begin{aligned} D_w &= \Delta\Gamma \frac{r}{4\pi h|h|} \int_0^{\Delta\beta} \frac{dw}{dw_0}\, d\beta \\ &= \Delta\Gamma \frac{r}{4\pi h|h|} \Phi[1.359(1 - e^{-\Delta\beta/\Phi}) - \frac{0.359}{4}(1 - e^{-4\Delta\beta/\Phi})] \\ &\equiv \Delta\Gamma \left[D_X(1 - e^{-\Delta\beta/\Phi}) + D_Y(1 - e^{-4\Delta\beta/\Phi}) \right] . \end{aligned} \tag{3.14}$$

Now the induction of the first element is divided into slow and fast decaying components, which can be directly inserted into Equation (2.27):

$$W_i = X_w^i + Y_w^i \tag{3.15a}$$

$$X_w^i = X_w^{i-1} e^{-\Delta\beta/\Phi} + D_X \Delta\Gamma (1 - e^{-\Delta\beta/\Phi}) \tag{3.15b}$$

$$Y_w^i = Y_w^{i-1} e^{-4\Delta\beta/\Phi} + D_Y \Delta\Gamma (1 - e^{-4\Delta\beta/\Phi}). \tag{3.15c}$$

A comparison of the original way to calculate the induction from the newest element and the proposed modification is shown in Figure 3.2. The X and Y components associated with D_w, the right terms of Equations (2.27) and (3.15), are plotted depending on the time step for $h/r = 0.01$. The plot shows that the original evaluation is showing a decreasing induction for increasing element length for time steps bigger than approximately 0.003 seconds. The new formulation is consistently approaching the asymptotic value of induction due to a quarter circle of trailed vorticity.

Another advantage is that D_X and D_Y only depend on the point distribution, which is constant during a simulation, and not on Δs, like the original D_w, cf. Equation (2.28). Therefore D_X and D_Y can be computed in the initialization of the program, which greatly improves the computational speed.

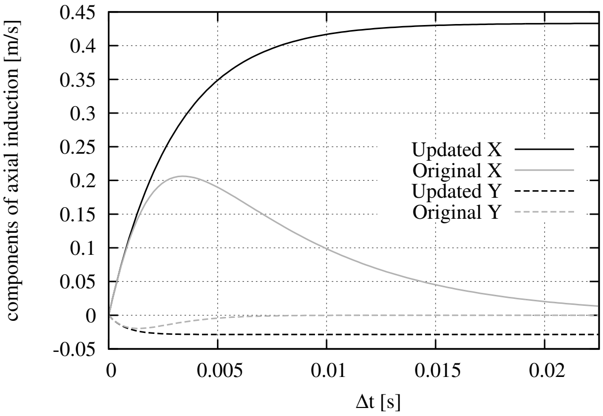

Figure 3.2: Comparison of the induction from the newest element, divided in the X and Y components depending on the chosen time step. The vortex with $\Delta\Gamma = 1$ is trailed from r=60 m, the blade rotates with 12.1 rpm and the calculation point is placed at r=59.4 m, so $h/r = 0.01$.

3.3.3 Root correction

For small, positive values of h/r, which means the vortex trailing point and the calculation point are close with the trailing point further outboard, both the analytical spatial decay function and Beddoes' approximation, Equation (2.24), reach small values within the first 90 degrees. If the calculation point moves further inboard, that means h/r gets closer to one, the function values decrease slower, as seen in the Figure 3.3. Thus the near wake model, integrating Beddoes' functions to infinity, gives a higher induction than the value of a quarter circle.

The goal of the correction here is to limit the steady state induction the NWM gives to that of a quarter circle and to reduce the dynamic effects afterwards.

In [II], the correction factor is then found as:

$$C = \frac{D_{w,\pi/2}}{D_{w,\infty}} = \frac{D_X(1 - e^{-\pi/(2\Phi)}) + D_Y(1 - e^{-2\pi/\Phi})}{D_X + D_Y}. \tag{3.16}$$

The root correction factor is applied in the near wake model by correcting Φ, which leads to corrected D_X and D_Y in the initialization of the program:

$$\Phi_C = \Phi C, \quad D_{X,C} = 1.359 \frac{r}{4\pi h|h|} \Phi_C, \quad D_{Y,C} = -\frac{0.359}{4} \frac{r}{4\pi h|h|} \Phi_C. \tag{3.17}$$

It is shown in Figure 3.4 how this approach limits the induction to the value reached after a quarter rotation.

3.3.4 Convection correction

In Beddoes' original model, Equation (2.24) describes how the influence of trailed vorticity diminishes as it moves away from the blade. This equation is only valid for axial induction, and in its derivation, the vortices have been assumed to stay in the rotor plane. Thus an error is introduced when Equation (2.24) is also used to model

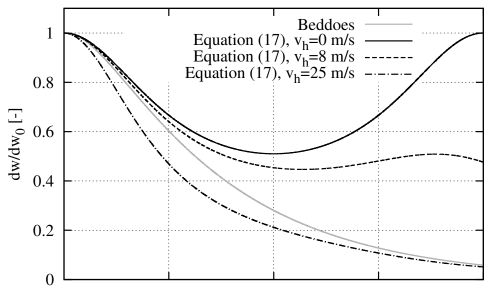

Figure 3.3: Comparison of the analytical trailing function, Equation (3.18), and Beddoes' approximation, Equation (2.24) and $h/r = 0.8$. Zero is clearly not reached within a quarter rotation at large h/r, even at high hub wind speeds.

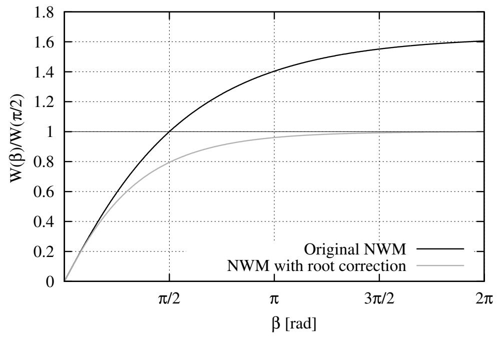

Figure 3.4: Induction due to constant trailed vorticity of length β as fraction of the induction due to a quarter circle at $h/r = 0.8$. The black curve shows the behavior of the original near wake model. Applying the correction factor on the value leads to the response shown in the gray curve.

the tangential induction, as proposed by Andersen [28]. Further, at high wind speeds Beddoes' modeling leads to erroneous results due to neglecting the downwind convection speed of the trailed vorticity. To evaluate theses errors, Equation (2.24) is derived in [II] based on the Biot-Savart law in the cases of axial and tangential induction and assuming helical vortex paths instead of circular arcs in the rotor plane.

Assuming a constant downwind convection velocity v_h the axial induction can be expressed as:

$$\frac{dw_z}{dw_{0,z}} = \frac{\left(\frac{h}{r}\right)^2 \left[1 - \left(1 - \frac{h}{r}\right)\cos\beta\right]}{\left(1 + \left(1 - \frac{h}{r}\right)^2 - 2\left(1 - \frac{h}{r}\right)\cos\beta + \left(\frac{v_h\beta}{\Omega r}\right)^2\right)^{3/2}}. \tag{3.18}$$

The only difference between Equation (3.18) and Equation (2.24) is the term $((v_h\beta)/(\Omega r))^2$, which describes the increasing distance from vortex trailing point to calculation point because of the downwind convection.

The equation for the induced velocity in the rotor plane perpendicular to the blade is derived analogue to the axial velocity in [II] and found as:

$$\frac{dw_y}{dw_{0,y}} = \frac{\left(\frac{h}{r}\right)^2 \left(1 - \frac{h}{r} - \cos\beta - \beta\sin\beta\right)}{\left(1 + \left(1 - \frac{h}{r}\right)^2 - 2\left(1 - \frac{h}{r}\right)\cos\beta + \left(\frac{v_h\beta}{\Omega r}\right)^2\right)^{3/2}}. \tag{3.19}$$

The inductions computed using Equations (3.18) and (3.19) differ for not small β and h/r. This is because the angle of the in-plane induction, and therefore the fraction of the induction that is perpendicular to the blade and contributes to the velocity triangle, changes as the vorticity moves away from the blade. There is also an in-plane component of the induction due to the vorticity parallel to the rotor plane that increases as the vorticity convects downstream. The error due to using the same approximation for dw/dw_0 for axial and tangential induction is quantified in the following.

The influence of the downwind convection of the vortices can be included in the near wake model with the helix angle as additional parameter. This additional parameter is here included in the decay rate Φ, which is then not only a function of h/r, cf. Equation (2.25), but also a function of the tangent of the helix angle φ.

Wang and Coton, [29], proposed to obtain an optimal value for Φ by integration of both sides of equation (2.24) and numerically determining the value of Φ for which the integral of the approximation equals the integral of the Biot-Savart law. The same approach is used in this work to determine optimal values of Φ in the presence of downwind convection, where the exact solution of the induction decay is given by Equation (3.18). The optimal Φ for computing the axial induction solves the following Equation:

$$\int_0^{pi/2} \left(\frac{\left(\frac{h}{r}\right)^2 \left[1 - \left(1 - \frac{h}{r}\right)\cos\beta\right]}{\left(1 + \left(1 - \frac{h}{r}\right)^2 - 2\left(1 - \frac{h}{r}\right)\cos\beta + \left(\frac{v_h\beta}{\Omega r}\right)^2\right)^{3/2}} \right) d\beta \tag{3.20}$$

$$= \int_0^{pi/2} \left(1.359e^{-\beta/\Phi_{opt,z}} - 0.359e^{-4\beta/\Phi_{opt,z}}\right) d\beta. \tag{3.21}$$

For the tangential induction computation, the optimal Φ follows accordingly from Equation (3.19).

The correction for downwind convection is developed as an additional factor that the Φ according to Wang and Coton, Equation (2.25), is multiplied with:

$$\Phi^* = \Phi \frac{\Phi_{opt,z}(\tan\varphi \neq 0)}{\Phi_{opt,z}(\tan\varphi = 0)} \approx \Phi f(h/r, \tan\varphi). \tag{3.22}$$

The correction function f is an exponential function approximation that has been obtained through curve fitting:

$$f = (1.1e^{-b_1(h/r)\tan\varphi} + a_2(h/r)e^{-b_2(h/r)\tan\varphi} - 0.1 - a_2(h/r)). \tag{3.23}$$

The dependency of the parameters b_1, a_2 and b_2 on h/r is as well approximated by exponential functions, as described in [II].

The approximation function f is compared against the numerically obtained values of $\Phi_{opt}(\tan\varphi \neq 0)/\Phi_{opt}(\tan\varphi = 0)$ in Figure 3.5. The purpose of f is to improve the accuracy of the axial induction computation when downwind convection is present, and this is clearly achieved. Also the optimal Φ for tangential induction is matched well for $|h/r| << 1$. For $h/r \to 1$ and low downwind convection speeds, the analytical expression for $dw_y/dw_{0,y} \geq 1$ for angles $\beta < \pi/2$, so an approximation using Beddoes' approach is not possible.

In principle, an optimal Φ for the tangential induction would be necessary for accurate results. This would, however, increase the computation time in a way that is not reflected by the benefits of the increased accuracy considering the small importance of a precise tangential induction computation. Therefore it is recommended to use the same approximation for Φ as for the axial induction.

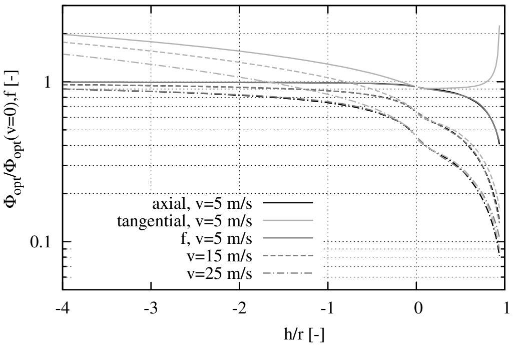

Figure 3.5: Comparison of the exact axial and tangential $\Phi/\Phi(v = 0)$ with the approximation function f to the axial induction, cf. Equation (3.22). Results are shown for different convection speeds. Vortices are trailed at $r = 10m$, the rotation speed is $\Omega = 12.1rpm$. The functions are not evaluated at h/r=0 and h/r=1, where the optimal Φ without convection tends to zero and infinity, respectively.

3.3.5 Near wake model acceleration

It is shown in [III] that the approximation of the spatial decay function , Equation (2.24), can be simplified by reducing the number of exponential functions from two to one. This halves the computation time because only one induction component has to be computed for the influence of each vortex on each blade section, as opposed to the X_w and Y_w components in the trailing wake algorithm, Equations (3.15b and 3.15c).

The reduced approximation function is defined as:

$$\frac{dw}{dw_0} \approx 1.359e^{-\beta/\Phi} - 0.359e^{-4\beta/\Phi} \approx A^* e^{-\beta/\Phi^*}. \tag{3.24}$$

Two requirements are used to find A^* and Φ^* [II]: the simplified approximation shall lead to the same quasi steady induction as the two term approximation. Further, the time integral of the difference between dynamic and quasi steady induction is required to be identical to the original model.

These requirements are fulfilled by choosing

$$A^* = \frac{(1.359 - 0.359/4)^2}{1.359 - 0.359/16}, \qquad \Phi^* = \Phi \frac{1.359 - 0.359/16}{1.359 - 0.359/4}. \tag{3.25}$$

A comparison of the buildup of induction in time, corresponding to the integral of the exponential functions, is shown in Figure 3.6. The largest deviations of the reduced model from the original model are below 2.5 % of the quasi steady induction $W(\beta = \infty)$.

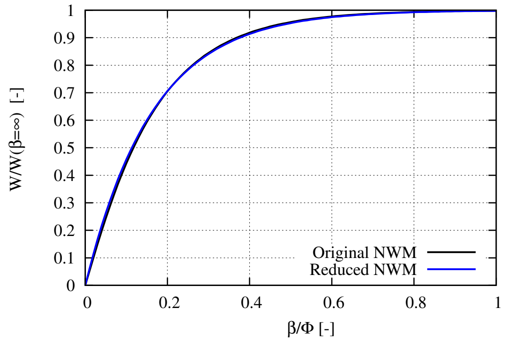

Figure 3.6: Comparison of induction buildup between full NWM and reduced NWM, depending on the length of a trailed vortex filament with constant circulation.

3.3.6 Radial point distribution

The importance of the radial discretization has been investigated in [I]. Two kinds of points are defined: vortex trailing points and calculation points. At the calculation points, the downwash, lift and circulation are determined. The circulation difference of two neighboring calculation points is then trailed at the vortex trailing point between them. At root and tip of the blade the vortex strength is the complete circulation of the nearest calculation point. Three different ways of distributing the points along the blade have been investigated:

- The **equidistant** distribution gives a constant resolution along the blades. The vortices are trailed from the root and tip of the blade, which is discretized in n sections, each with a vortex trailing point at both ends and a calculation point in the middle.
- The **cosine** distribution places the vortex trailing points at equal angle of a half circle over the blade, cf. Figure 3.7. The calculation points of the sections are placed in the middle of two trailed vortices.

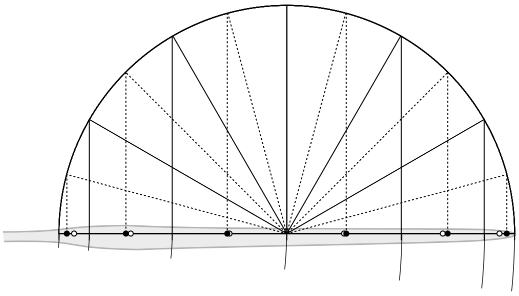

Figure 3.7: Sketch of the cosine and full cosine point distribution. The calculation points are placed at the positions marked by white (cosine) or black (full cosine) dots.

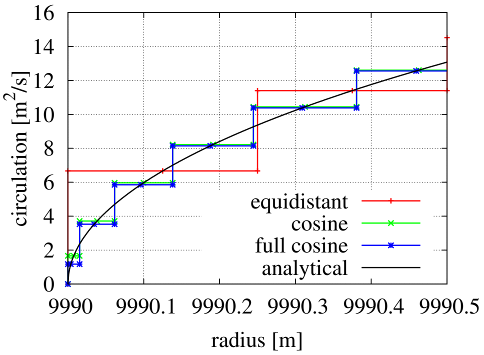

Figure 3.8: Resolution of an elliptical circulation close to the edge of the wing investigated in Section ?? for the different point distributions.

- The **full cosine** distribution, which is also used in the AWSM code [31] places the calculation points and vortex positions at equi-angle increments, also shown in Figure 3.7.

Figure 3.8 shows an example of how a continuous elliptical circulation is represented by constant values at the calculation points for the different point distributions.

3.4 Iteration of near wake and unsteady airfoil aerodynamics modeling

3.4.1 Iteration scheme

The NWM can become numerically unstable depending on the time step, operating point of the turbine, blade geometry and point distribution, [I]. Figure 3.10 shows the maximum time step where a stable computation is possible for a fine and coarse geometry definition, shown in Figure 3.9, of the NREL 5 MW blade. The coarse geometry definition is a blade geometry typically distributed for BEM computations and the fine distribution is more suitable for computations with higher fidelity codes. The aerodynamic calculation points and vortex trailing points follow a cosine distribution, which means they are placed at equi-angle increments. The time steps have been determined in a numerical experiment, where the time step has been decreased until large oscillations of the induction disappear. The results are accurate to the first significant digit. It can be seen that the finer blade geometry leads to a more stable computation. This can be explained by the smoother blade tip, where the blade chord is approaching zero. Thus the radial circulation gradient at the very blade tip is smaller and the vortex strength of the tip vortex is distributed to several weaker trailed vortices in the tip region that are less likely to cause numerical instabilities. In a coupled aeroelastic simulation, the small stable time steps for resolutions of 30 to 60 points would lead to a very slow computation especially in case of the coarser blade geometry. The numerical instability which occurs at larger time steps can be explained as follows: The axial induction due to trailed vortices typically reduces the angle of attack at a blade section, which in attached flow leads to a reduced lift. In the original implementation of the NWM the constant circulation trailed during a time step is only depending on the flow

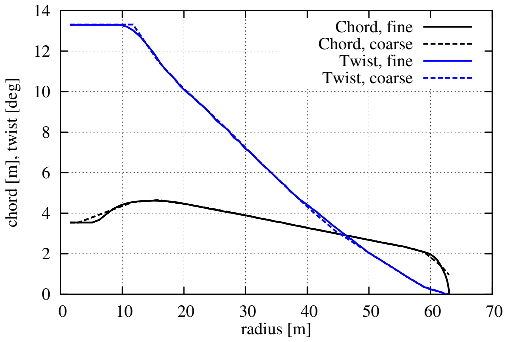

Figure 3.9: Coarse and fine blade geometry for the NREL 5MW reference turbine. The coarse definition is a typical geometry definition for BEM based computations. The finer geometry is smoothed for use in computational fluid dynamics and free wake codes.

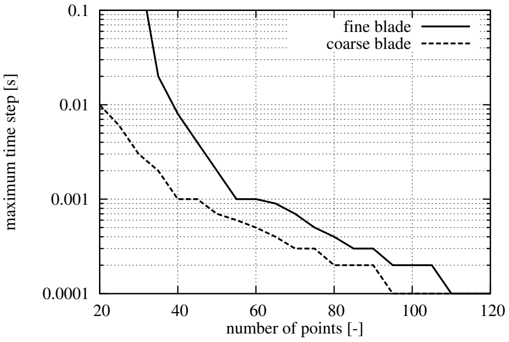

Figure 3.10: Maximum stable time step depending on number of points for the coarse and fine blade geometries of the NREL 5 MW reference turbine. The points are distributed using a full cosine distribution, as shown in section 3.3.6. The results are obtained through numerical experiment.

conditions at the blade at the beginning of a time step. Thus a longer time step will lead to a bigger induction and thus a further reduction in lift in the next time step. If the time step is too large, the induction can become big enough to create a negative lift in the next time step, that is bigger in absolute value than the previous positive lift. This in turn leads to stronger trailed vortices of opposite sign, which will cause even bigger induced velocities in the opposite direction, which again leads to stronger vortices.

To stabilize the NWM the balance between trailed vortex strength based on the sectional circulation and the induced velocities are iterated to equilibrium in each time step, which removes the need for small time steps to stabilize the aerodynamics model. The iteration is structured as follows:

1. The quasi-steady circulation is computed according to Joukowski's law using the velocity triangle at the airfoil section based on the induction from the last iteration.
2. The unsteady circulation after half a time step is computed including shed vorticity effects, cf. Section 3.3.1.
3. This unsteady circulation defines the constant vortex strengths trailed during a time step
4. These constant vortex strengths lead to an induction at all airfoil sections.
5. The new induction is combined from the inductions from step 1 and 4 by applying a relaxation factor: $w_i = w_{i-1}r + w_i(1-r)$, where the subscript i indicates the iteration number. If w_i is sufficiently close to w_{i-1}, it is the desired converged induction.

The BEM model for the far wake is excluded from this iteration procedure. The AOA and relative velocity used to compute the far wake induction are the values from the converged iteration in the previous time step. This is accelerating the computation and is feasible because the near wake effects are on a much faster time scale than the dynamic inflow effects in the BEM model.

3.4.2 Estimation of the necessary relaxation factor

An approach to estimating a relaxation factor for the iteration of near wake model and unsteady circulation buildup is presented in [III]. To ensure a conservative estimation, it is based on the least stable case which is characterized by the following properties:

- One single blade section with one vortex trailing from each side. Adjacent sections would tend to have similar circulations and therefore reduce the vortex strengths and the corresponding induction at the blade section. The trailed vortices on both sides of the section depend only on the bound circulation Γ of that section.
- The lift coefficient is linearly dependent on the angle of attack, $C_L = 2\pi\alpha$. A reduced but still positive gradient due to stall would stabilize the model.
- No prior trailed vorticity is present. It would stabilize the model, because the induction would not only be determined by the momentary circulation at the section, but also by the decaying influence of the wake trailed before. If the model converges in the very first time step, with a given induction at the section from the previous iteration then the iterations will also converge with prior trailed vorticity.
- The helix angle at which the vortices are trailed is assumed to be small. Thus all the induction due to trailed vorticity is assumed to be axial induction.

With these assumptions, the following expression for the necessary relaxation factor r for each blade section is derived in [III]:

$$r = -\frac{1 + \frac{dw_i}{dw_{i-1}}}{1 - \frac{dw_i}{dw_{i-1}}}, \tag{3.26}$$

where dw_i/dw_{i-1} is the derivative of the downwash at a blade section at one iteration with respect to the downwash in the previous iteration. It is determined as:

$$\frac{dw_i}{dw_{i-1}} = \frac{\Gamma_{dyn}}{\Gamma_{QS}}\pi c(B_1 - B_2)\left(\frac{\alpha(v_\infty - w_{i-1})}{v_{rel}} + \frac{v_{rel}}{\Omega r\left(\left(\frac{v_\infty - w_{i-1}}{\Omega r}\right)^2 + 1\right)}\right), \quad \text{where} \tag{3.27}$$

$$B_v = (-1)^v(D_{X,v}(1 - e^{-\Delta\beta/\Phi_v}) + D_{Y,v}(1 - e^{-4\Delta\beta/\Phi_v})), \tag{3.28}$$

where Γ_{dyn}/Γ_{QS} follows from Equation (3.9) and the subscript v denotes the vortex trailed inboard ($v = 1$) and outboard ($v = 2$) of the blade section. The gradient is mainly depending on the time step and point density (through B_1 and B_2) and the rotational speed.

In the initial phase of the simulation, the maximum relaxation factor for all blade sections can be quickly determined by setting $w_{i-1} = 0$ in Equation (3.27) and looping through the sections. The highest necessary relaxation factor for one section that has been found is then used for the whole blade. As the simulation continues, the relaxation factor can be updated whenever there are big changes in rotational speed, induction, or blade pitch. If the relaxation factor is updated every several time steps, determining the relaxation factor takes negligible computation time. Choosing a slightly more conservative relaxation factor than what has been estimated will ensure stability also in different conditions than the ones the factor was based on.

3.5 Interaction with the dynamic inflow induction grid

Because the near wake model gives the induction at the blade position due to the vorticity trailed from the respective blade, the induced velocity from the near wake is in HAWC2 treated in the same way as blade velocity and pitch angle, that is as a local blade parameter. This means that the total induction is consisting of one part that is computed in the fixed polar grid, the far wake induction, and one part that is rotating with the blades, the near wake induction. To obtain the far wake induction, the BEM induction is scaled by a coupling factor that is smaller than one. The coupling factor is determined so that the integral thrust force of HAWC2 NW matches the HAWC2 BEM model with tip loss correction. The near wake model needs to be iterated to ensure a stable operation. One call of the aerodynamic model HAWC2 NW is structured as follows:

1. BEM induction
    a) Find the two closest blades to each grid point.
    b) Calculate thrust coefficient using blade velocity, pitch angles and near wake induction of each of the two closest blades.
    c) Interpolate thrust coefficient at the grid point based on azimuth angle.
    d) Calculate far wake induction.
2. Near wake induction
    a) Find closest grid points to each blade section.
    b) Interpolate far wake induction and wind speed.
    c) Iterate until convergence:
        i. Compute angles of attack and relative velocity.
        ii. Compute length and helix pitch angle of trailed vorticity.
        iii. Compute quasi-steady circulation at each blade section.
        iv. Apply time lags to account for dynamic circulation buildup.
        v. Compute induction from trailed vorticity in the near wake.
        vi. Apply relaxation factor on near wake induction.
3. Calculate dynamic lift, drag and moment coefficients, using the dynamic stall model in [25]. These coefficients do not feed back back to the BEM induction, but are used to determine the forces on the structure.

CHAPTER 4

Steady state results, [I,II]

The main findings from [I] and [II] are presented in this chapter. The influence of the spacial discretization on the steady downwash at an elliptical wing, published in [I], is shown in the next section.

Section 4.2 illustrates the time step independence of the steady results due to the modified trailing functions presented in Section 3.3.2 for the NREL 5MW reference turbine in an exemplary normal production case, [II].

The main results of [II] are given in Section 4.3.1. The section includes a validation of the root correction, convection correction and the coupling factor computation, as well as a comparison of the radial load distribution for selected normal production cases of the NREL 5MW reference turbine against full rotor CFD.

4.1 Spatial discretization, [I]

A wing with a prescribed elliptical circulation has been used to investigate the influence of the spatial discretization. It is modeled as a 10 m long section at the end of a 10 km long blade to approximate a parallel free stream, similar to the case presented by Madsen and Rasmussen, [17]. The circulation at radius r is given as

$$\Gamma = 30\sqrt{(1-((r-9995)/5)^2)}, \tag{4.1}$$

which results in a constant downwash of 1.5 m/s along the wing according to lifting line theory. The blade rotates with 0.03359 rpm, which is equivalent to a free stream velocity at the wing of about 35 m/s.

To investigate the effect of the different spatial discretizations introduced in Section 3.3.6, Figure 4.1 shows the downwash of the near wake model in steady state for a 175 m long wake. The wing is discretized with 40 (left plot) or 80 (right plot) calculation points, corresponding to 41 and 81 vortex trailing points. While all spatial distributions perform well in the middle sections, the equidistant and cosine distribution lack accuracy close to the edges of the wing. They even lead to negative downwash in the outer sections of the wing.

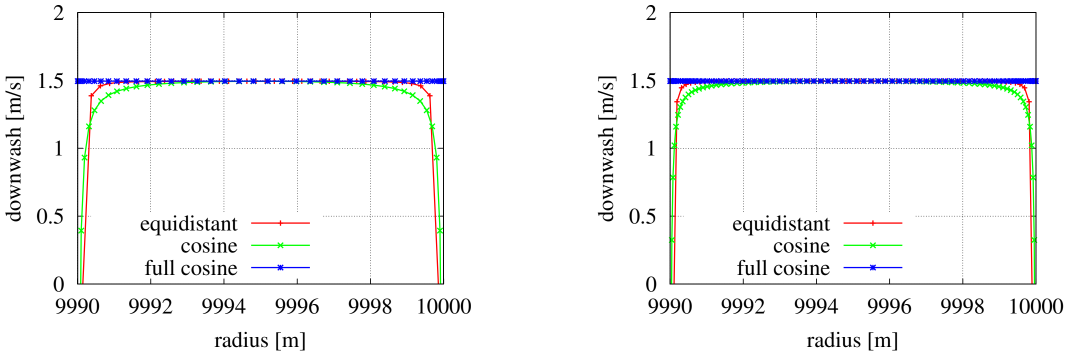

Figure 4.1: Comparison of the steady downwash at an elliptical wing with a wake of 175 m length. The calculation points and vortex trailing points have been distributed using the distribution methods described in Section 2.4. The wing has been discretized using 40 (left plots) or 80 (right plots) calculation points.

4.2 Modified trailing functions, [II]

The modified trailing functions proposed in Section 3.3.2 lead to a time step independent steady induction from the NWM. This is illustrated in Figure 4.2, where the steady axial induction of the NREL 5 MW turbine at 8 m/s is shown for different time steps computed with the original trailing functions aside the induction predicted by the modified trailing functions. The result of the original model clearly converges to the result of the modified model if the time step is reduced. For commonly used time steps mainly the induction at the outer part of the blade deviates from the time step independent result, but through the coupling factor, cf. Section 3.2.1, the whole blade is affected by a change of the induction close to the tip. Note that the modification of the functions not only removes the need for a fine time step to achieve an accurate steady induction, but also reduces the computation time per time step compared to the original model, as shown in Section 3.3.2.

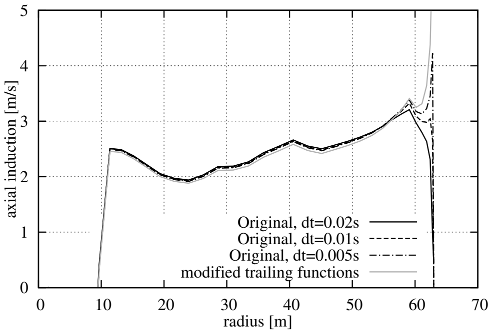

Figure 4.2: Results from the coupled model at 8 m/s. The effect of the tip vortex varies with time step in the original model and converges to the time step independent results of the modified model presented in Section 3.3.2.

4.3 Validation steady corrections and loads, [II]

In the following Section 4.3.1, the NWM is first compared with the induction following directly from the Biot-Savart law for the NREL 5 MW reference turbine, [32], to evaluate the improvement due to the modifications of the NWM. Cases with wind speeds above and below rated are investigated.

The coupled model is validated in Section 5.2 against a BEM model and full rotor CFD results from EllipSys3D [3] in steady cases.

4.3.1 Comparison of near wake model with induction from Biot-Savart law

Root correction

The root correction is demonstrated for the NREL 5 MW turbine in a normal operation case with $\Omega = 9.2$ rpm, uniform inflow with $v_\infty = 8$ m/s and unpitched blades in Figure 4.3. The results have been obtained in the following way: the axial and tangential induction, as well as the vortex strengths, at sections distributed over the blade from a run of the coupled model with all modifications presented in this thesis has been used as input for a numerical integration of Equation (3.18) over a quarter rotation. The result from this integration is then compared to the near wake induction using either the integral of Beddoes functions from zero to infinity, which is equivalent to $D_X + D_Y$ or the corresponding integral of the functions corrected for the root error, $D_{X,C} + D_{Y,C}$, cf. Section 3.3.3.

The improvement clearly appears in Figure 4.3, where the results according to the Biot-Savart law are closer to the results from the NWM with root correction up to a blade radius of 35 meters.

Convection correction

The effect of the convection correction is investigated for two cases above rated wind speed, again based on the NREL 5 MW turbine. In these cases, the uniform wind speeds are $v_\infty = 15$ m/s and $v_\infty = 25$ m/s, the turbine is rotating with its rated speed of $\Omega = 12.1$ rpm and the blade pitch is 10.54° and 23.195°, respectively. The induction and

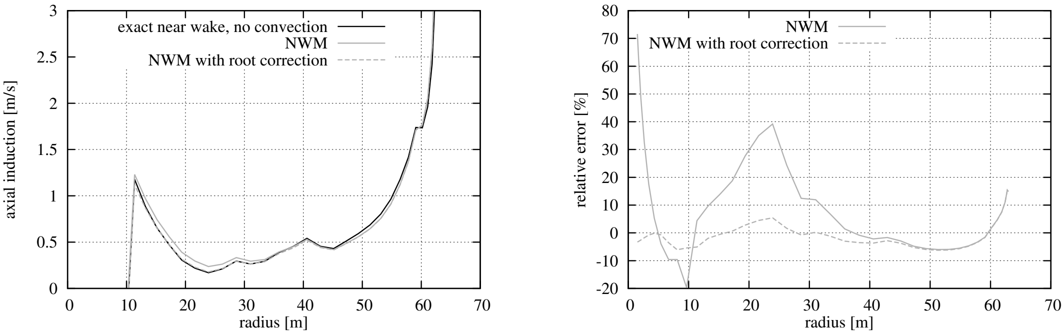

Figure 4.3: Effect of the root correction on the induction from the near wake for normal operation at 8 m/s. Near wake induction (left) and relative error (right).

vortex strength from the coupled model are used as input for the numerical integration of the induction from circular arcs and helical arcs, cf. Equations (2.24) and (3.18). The inductions from these integrations are then compared with the near wake induction from the NWM, without and with the correction for downwind convection of the vortices.

As shown in Figure 4.4, the convection correction can account for the helix angle, which is most dominant close to the root of the blade.

4.3.2 Comparison of the coupled model with a BEM model and CFD

Steady power and thrust

The thrust and power in steady operation of the NREL 5 MW reference turbine predicted by the coupled model and a BEM model are compared for different wind speeds of 4 to 25 m/s in Figure 4.5, along with the coupling factor computed for the different cases. The power and thrust agree with deviations smaller than 1.5 % and 2.5 %, respectively. The coupling factor stays almost constant where the tip speed ratio and the helical pitch angle are fixed, and then gets reduced at higher wind speeds. This can be explained by the faster convection of the wake away from the turbine at higher wind speeds and the corresponding bigger fraction of the induction due to the near wake.

Radial load distribution

The radial in-plane and out-of-plane load distributions along the NREL 5 MW blade are shown in Figure 4.6 for normal operation at wind speeds of 8 and 25 m/s. The HAWC2 BEM model is compared with the coupled near and far wake model and full rotor CFD. The CFD results have been computed with the incompressible RANS solver EllipSys3D [3] assuming fully turbulent flow and using the K-omega SST turbulence model by Menter to close the RANS equations. The computations are done on a structured grid in which each blade exhibits 256 cells in the chord wise, 128 cells in the span wise and 128 cells in the normal direction. This results in approximately 14 million mesh cells for the entire rotor mesh.

At 8 m/s, the thrust force agrees very well between all the aerodynamic models. There

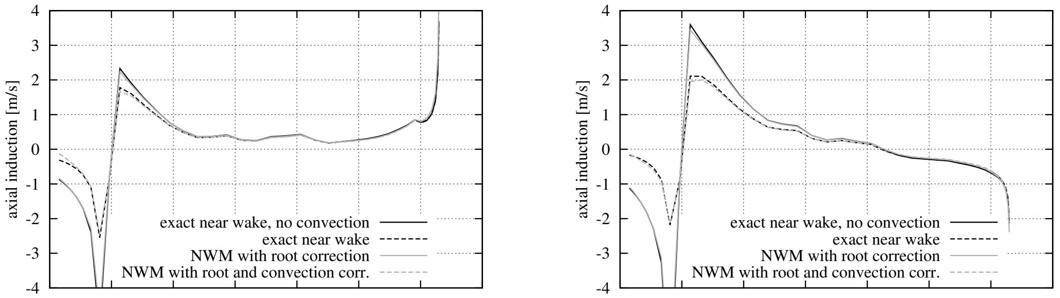

Figure 4.4: Steady near wake induction at 15 m/s (left) and 25m/s (right), NREL 5 MW reference turbine. The correction of the downwind convection improves the result significantly.

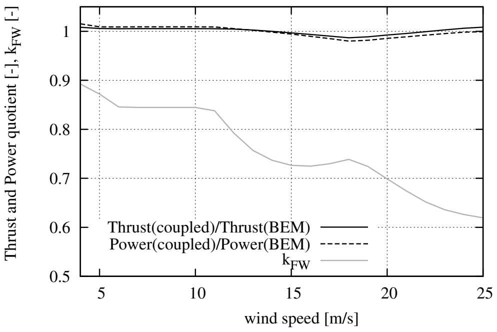

Figure 4.5: Agreement of power and thrust of coupled model with BEM model and the coupling factors automatically chosen for different wind speeds. The aerodynamic power of the NREL 5 MW rotor agrees within 2.5%, the thrust within 1.5%.

are some differences between the faster models and CFD close to the root and tip of the blade, which can be explained by differences between the lift coefficients from the airfoil polars and the corresponding forces obtained in the 3D CFD computation. The differences seem to be largest for the thick DU airfoils used up to 19.95 m blade radius and the NACA64 airfoil with 17 % relative thickness used on the outboard part of the blade.

The tangential forces are in close agreement between the models, with the coupled model over predicting the tangential forces on the mid blade. Close to the root and tip of the blade, the coupled model results are closer to CFD than the BEM results.

The forces from the CFD computations deviate strongly at 25 m/s wind speed for airfoils with more than 30 % thickness up to a blade radius of 25 m, which is in agreement with the steady state results at high wind speeds for flexible blades presented by Heinz [4]. The results from the coupled model clearly show the effect of the strong root vortex that is present in this case, and the loads are in between the BEM and CFD results.

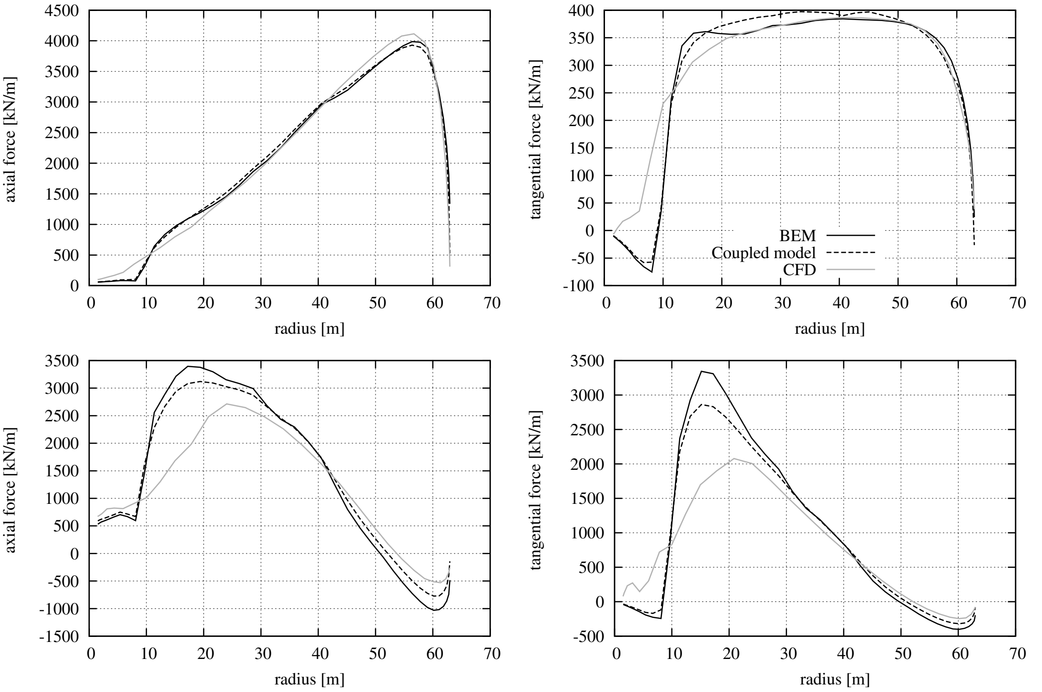

Figure 4.6: Comparison of axial and tangential forces in normal operation at 8 m/s (top) and 25 m/s (bottom) of a BEM model, the coupled near and far wake model and full rotor CFD.

CHAPTER 5

Unsteady results, [III]

This chapter contains the main findings from manuscript [III], which is mainly concerned with the validation of the iterative procedure for the near wake model and a comparison of the unsteady force response of the coupled model with a BEM model and the free wake panel code GENUVP.

In the following section, the effectiveness of the iteration procedure is demonstrated for a horseshoe vortex. Then in Section 5.2 the unsteady induction predicted by the coupled near and far wake model is compared with results from a BEM model including dynamic inflow and the free wake code described in Section 5.2.1 for pitch steps and prescribed vibrations of the blades of the NREL 5 MW reference turbine.

5.1 Effectiveness of iteration procedure

To illustrate the efficiency of the iterative implementation, induction buildups for a simplified case are shown in Figure 5.1. The simple test case is a wing with a span of 0.3 m and a constant bound circulation, so that only two vortices with opposite vortex strength are trailed at the edges. To use the NWM, the wing is modeled as the only aerodynamic section at the end of a 10 km long blade. Therefore the air is moving almost orthogonal to the wing in its proximity. The free stream velocity is 70 m/s. At t=1 s, the geometric AOA of the wing with a symmetrical profile is increased from 0 to 5 degrees within 0.02 s. The lift coefficient is that of a flat plate, $c_L = 2\pi\alpha$, the chord is 1 m. The buildup of the circulation is modeled as in the coupled model, cf. Equation (3.13). The left side of Figure 5.1 shows the induction buildup for different time steps without iterating, the right side shows the effect of the iteration procedure. Both the overshoot of the induction for a time step of 0.002 s and the oscillations for a time step of 0.02 s are reduced by the iteration procedure. The result with a time step of 0.02 s is not perfect, but the iterative model is clearly more stable and computes less time step dependent results in this demanding test case.

In [III], it is further shown that the estimated relaxation factors, Equation (3.26), are conservative at normal operation at wind speeds of 8 m/s and 25 m/s for both coarse and fine blade geometries shown in Figure 3.9.

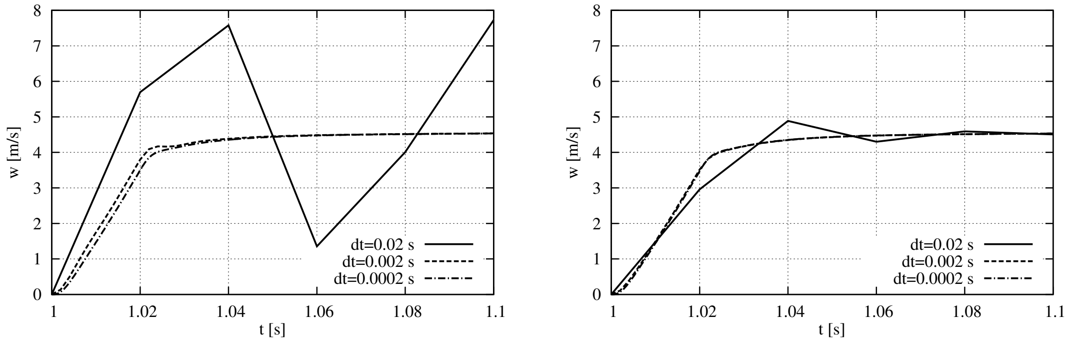

Figure 5.1: Buildup of the downwash for a horseshoe vortex depending on the time step. The NWM tends to be unstable (left) but can be stabilized by iterating to convergence of the downwash (right).

5.2 Comparison with a BEM model and a free wake code

In this section the induction and loads predicted by the coupled model are compared with other codes in different cases, namely pitch steps in Section 5.2.2 and blade vibrations in Section 5.2.3. The spatial and temporal resolutions used for the computations are not included here. These simulation parameters are detailed in [III].

5.2.1 GENUVP

GENUVP is a potential flow solver combining a panel representation of the solid boundaries (blades) with a vortex particle representation of the wake. In the present work, the blades are considered as thin-lifting surfaces carrying piecewise constant dipole distribution (equivalent to horseshoe type vortex filaments). Blades shed vorticity in the wake along their trailing edges and their tips (vorticity emission line). In the model a hybrid wake approach is followed. The near wake part, consisting of the newly shed vorticity trailed within the current time step, is modeled as a vortex sheet also carrying piecewise constant dipole distribution. Within every time step, a strip of wake panels is released that are in contact with the emission line. Applying the no-penetration boundary condition at the center of each solid panel and the Kutta condition along the emission line the unknown dipole intensities are determined. Then at the end of each time step, the newly shed vorticity is transformed into vortex particles and then all vortex particles are convected downstream with the free flow velocity (free wake representation) into their new positions. The layout of the modeling is shown in Figure 5.2. Details of the model can be found in [2]. Since GENUVP is defined as a potential flow solver, the loads need correction in order to account for viscous effects. This is done by means of the generalized ONERA unsteady aerodynamics and dynamic stall model [33]. The potential load is calculated by integrating pressures (pressure differences between pressure and suction side) over the lifting surfaces. Then, through a consistent definition of the local flow angle of attack and relative flow velocity corrections are applied on the potential loads on the basis of the ONERA model. Thereby, the effects of viscous drag and flow separation are taken into account [34]. In the case of aeroelastic coupling, the aerodynamic part will receive the deformed geometry and the deformation velocity and feedback the loading. The deformed geometry as well as the deformation velocities are introduced into the boundary conditions and therefore the flow is accordingly adjusted.

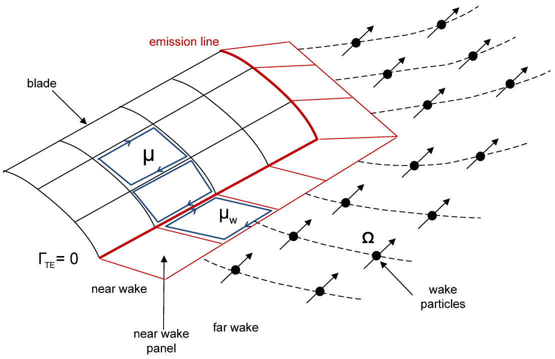

Figure 5.2: Layout of the free-wake modeling of a blade: black lines define the blade surface panels; red lines define the wake generated within a time step; symbols represent freely moving particles.

5.2.2 Pitch steps

Pitch steps with a stiff blade have been performed to compare the performance of the coupled aerodynamic model to a less complex unsteady BEM model and the more complex free wake panel code. The NREL 5 MW reference turbine is operating at a wind speed of 8 m/s and a rotation speed of 9.2 rpm. The turbine starts with blades that are pitched by 5 degrees to feather. After 60 seconds simulation time, the blades are pitched to 0 degrees with a constant pitch rate in either 1 or 4 seconds. Because the radial force distributions before and after the pitching are not in exact agreement for the three aerodynamic models, the forces are normalized in the following comparisons. To normalize, the values of the axial force immediately before the pitch step have been subtracted from each respective time series, which is then divided by the corresponding axial force at 45 seconds.

In Figures 5.3 and 5.4, the axial force response at a position at mid blade and close to the blade tip is shown. In case of the fast pitch step, the free wake code predicts a slower force response during the pitch step than the BEM model. The results of the coupled model during the pitch step lie in between the other codes. In the free wake code results, some oscillations due to the changing wake geometry are present after the pitch step that can not be seen in the results of the less complex codes, especially at the mid blade section. These oscillations make it difficult to judge if the BEM model or

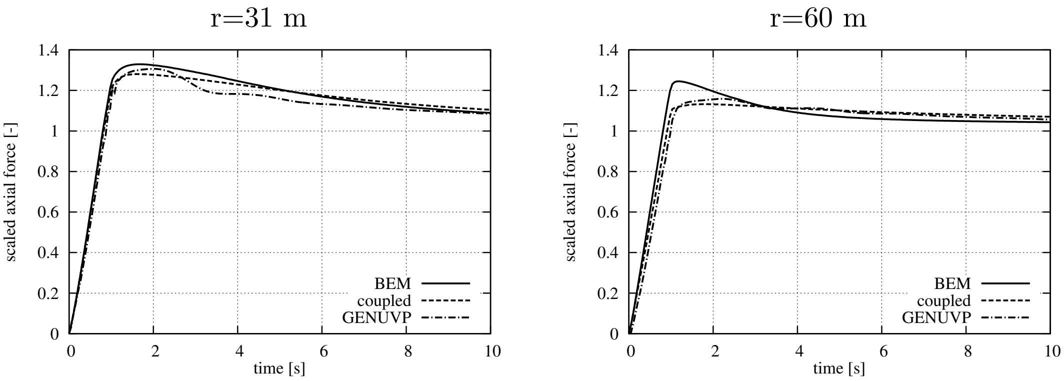

Figure 5.3: Scaled axial force at different radial positions during and after a pitch step by 5 degrees in 1 s.

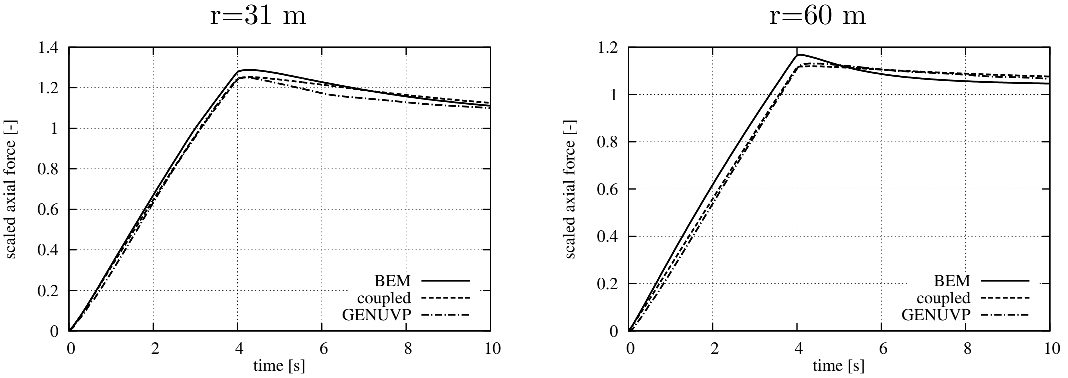

Figure 5.4: Scaled axial force at different radial positions during and after a pitch step by 5 degrees in 4 s.

the coupled model are predicting the overshoot closer to the free wake code, the results of which are in between the two. However, at the tip section the oscillations are less pronounced and the agreement between the coupled model and the free wake model is better.

The results of the slower pitch step in Figure 5.4 show less oscillations of the free wake code results, but they are still visible at the mid blade section. The coupled model and the free wake code agree well on the slope of the force increase during the pitching motion. The steeper slope predicted by the BEM model can be explained by a slower reaction of the induction than in the other codes. In this case, the results from the coupled model agree better with the free wake code than the BEM results, both during the pitching motion and on the predicted overshoot.

Axial force distributions for a partial pitch comparison are shown in Figure 5.5. This comparison used the same starting conditions as the comparisons above (8 m/s wind speed and the blade pitched by 5 degrees to feather), but only the outer half of the blade is pitched to zero degrees during 1 second. As shown in the left plot of Figure 5.5, the effect of the cross sectional coupling due to the trailed vorticity at the mid blade is predicted by both the coupled aerodynamics model and the free wake code at a similar degree. Compared to the BEM model, these codes predict a smoothing of the radial load distribution around the discontinuity of the blade pitch.

In the right plot of Figure 5.5, the time history of the axial force between the coupled model and the free wake code is compared at a radius of 21.6 meters. Because this part of the blade is not pitching, the force predicted by the BEM model is constant, therefore it is not included in this comparison. The behavior of the coupled model and GENUVP shows a similar time scale, but the overshoot is under predicted by the coupled model by around 40%.

5.2.3 Vibrations

In this section the aerodynamic response to blade vibrations is investigated for normal operation at 8 and 25 m/s. The corresponding rotor speeds are 9.2 rpm and 12.1 rpm and the pitch angles 0 degrees and 23.2 degrees, respectively. The load response to the prescribed vibration cases is compared in terms of radial distributions of aerodynamic work during one oscillation, where a positive aerodynamic work corresponds to a positive aerodynamic damping of the vibration. The mode shapes are chosen as the

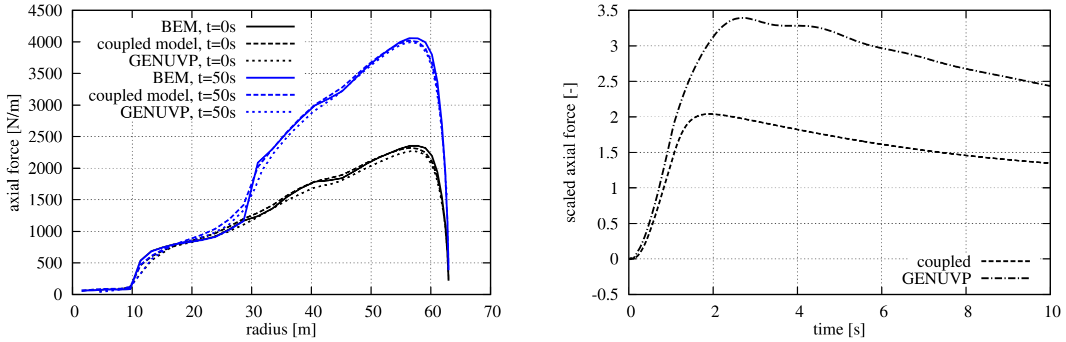

Figure 5.5: Left plot: Force distribution before the pitch step and 50 seconds after. Right plot: Time history of the axial force comparing coupled model and GENUVP at 21.6 meter radius. The BEM gives a constant force.

Mode	freq. [Hz]	modal mass [kg]
1st flap	0.66	905
1st edge	1.0	1480
2nd flap	1.82	594
2nd edge	3.2	793

Table 5.1: Frequencies f and modal masses m of the prescribed mode shapes for the work comparison.

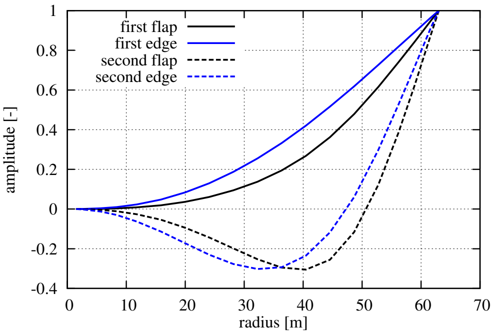

Figure 5.6: Mode shapes used in the work computations, which are simplified to be purely in-plane or out-of-plane deflections.

first and second structural mode shapes of the NREL 5 MW reference turbine blade at stand still, cf. Figure 5.6. To simplify the comparison, the vibrations have been prescribed either purely in-plane or out-of-plane for the edgewise and flapwise vibrations, respectively. The frequencies used for the computations are shown in Table 5.1, as well as the modal masses that are used for damping estimations.

In this thesis, only the results for a tip amplitude of 0.25 m are shown. In [III], the aerodynamic response for the first flap mode with an amplitude of 0.5 m and the first edge mode with an amplitude of 1 m is also included. The aerodynamic work in these cases was roughly a factor of 4 and 16 higher than in the flap and edge modes with 0.25 m, as expected according to Equation 5.1.

In addition to the results shown in [III], this section includes results from two further models: full rotor CFD for the cases at 8 m/s and a BEM model without shed vorticity modeling in all cases. The comparison with full rotor CFD provides additional validation of the BEM and vortex model results. The results BEM model without shed vorticity, on the other hand, make it possible to directly compare the effects of the trailed vorticity modeling that this work is concerned about with the more well known shed vorticity modeling.

In the BEM and coupled model, the blade section velocities due to the vibrations are applied on the aerodynamic models as additions to the relative wind speed. The

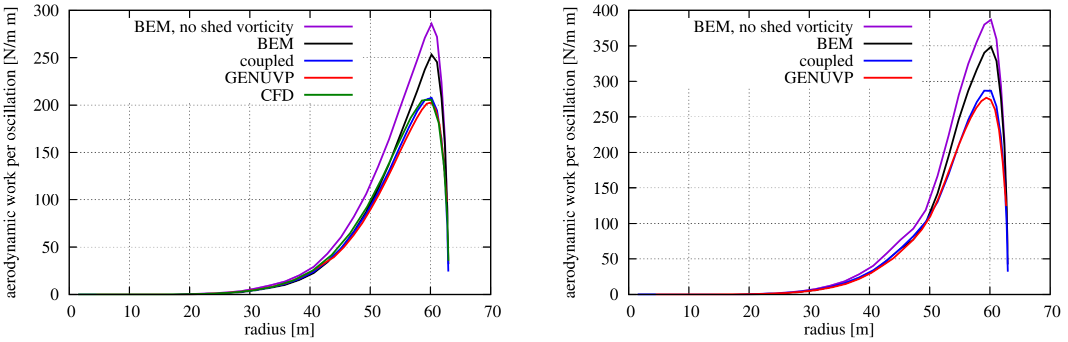

Figure 5.7: Comparison of aerodynamic work during one oscillation of first flap motion at 8 m/s (left plot) and 25 m/s (right plot).

deflection of the blade and the resulting change of the section positions and the geometric parameter Φ of the NWM have been neglected because the amplitudes are small compared to the blade radius.

The aerodynamic work during out-of-plane motion according to the first flap mode shape is shown in Figure 5.7. The work integrated over the blade is over predicted by the BEM model by about 10% compared to the free wake code in all cases. The results of the coupled model are very close to the free wake code results. They slightly deviate towards higher work. This comparison indicates that the influence of the trailed vorticity behind the other two rotor blades, which is not included in the NWM, on the aerodynamic forces due to blade vibrations is small compared to the influence due to the wake of the blade itself in normal operation. The additional full rotor CFD results at 8 m/s in Figure 5.7 agree very well with the coupled model and GENUVP. Comparing the results from BEM without shed vorticity, BEM and the coupled model shows that both shed and trailed vorticity modeling decrease the aerodynamic work. The shed vorticity effects have a significant influence on the results along the whole blade radius. The trailed vorticity, on the other hand, mainly affects the results close to the blade tip, where the aerodynamic work is reduced by a larger margin than due to the shed vorticity effects.

For the edgewise vibrations, the different models agree worse, as shown in Figure 5.8. In [III], a model comparison at 8 m/s excluding drag shows a good agreement, which suggests that the reason for the differences might be in the different unsteady drag modeling. However, the differences in the unsteady drag prediction between the codes, which are based on the inviscid part of the Beddoes-Leishman type dynamic stall model in case of BEM and coupled model computations and the ONERA model for the free wake model are not the focus of this work. Even though the agreement of the radial work distribution is not as good, the coupled model produces results much closer to the free wake code and the CFD computations close to the blade tip than the BEM model.

At 25 m/s, where the inflow angle is much larger and the work is predominantly due to the vibration component perpendicular to the inflow, the coupled near and far wake model is agreeing quite well with the free wake code as in the cases with out-of-plane vibrations discussed above.

The influence of the trailed vorticity is again found to be of the same order of magnitude as the influence of the shed vorticity, but more restricted to the blade tip.

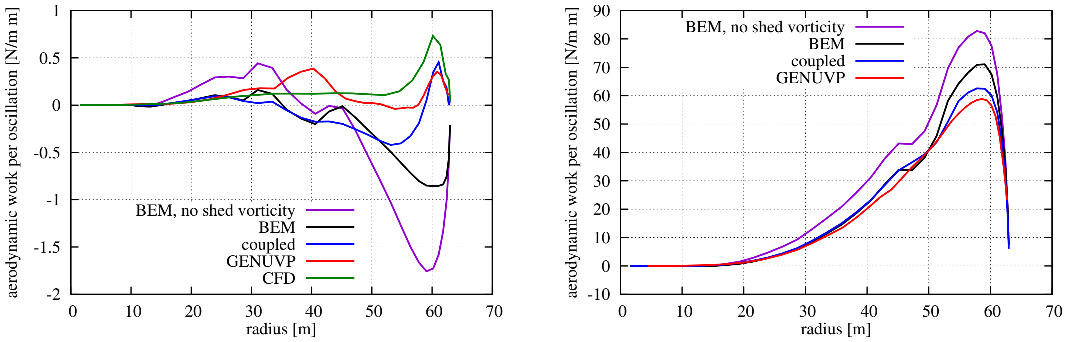

Figure 5.8: Comparison of aerodynamic work during one oscillation of first edge motion at 8 (left plot) and 25 m/s. (right plot)

The results from prescribed vibrations using the second mode shapes presented in Figure 5.6 are shown in [III] to follow the same trends as the results of the first mode shapes discussed above: In all cases, the coupled model results are closer to the free wake code results than the results from the unsteady BEM model. The agreement is best in the out-of-plane cases and worst for the in-plane vibrations at 8 m/s, where the direction of the vibration is close to parallel to the inflow.

To easier evaluate the impact of the differences observed in this section on load computations and stability analysis, the aerodynamic work can be expressed in terms of a damping ratio of a respective blade mode. It is important to note that, because the computations have been based on prescribed mode shapes that are purely in-plane and out-of-plane and based on structural, not aeroelastic, analysis of the turbine blades, these logarithmic decrements are not corresponding to any aeroelastic blade modes. Further, the energy exchange between different aeroelastic modes is neglected in this estimation. The estimated logarithmic decrements can, however, illustrate the order of magnitude of the effect of aerodynamic modeling on aerodynamic damping of flapwise and edgewise blade modes.

Assuming a single degree of freedom system with the modal mass m and frequency f, given in Table 5.1, the damping ratio ξ and logarithmic decrement δ can be expressed as:

$$\xi = \frac{W_{aero}}{8\pi^3 A^2 f^2 m} = \frac{1}{\sqrt{1 + \left(\frac{2\pi}{\delta}\right)^2}} \tag{5.1}$$

where A is the amplitude and W_{aero} the integral of the aerodynamic work over the whole blade in one period of oscillation. The estimated logarithmic decrements according to Equation (5.1) corresponding to the first flap motion at 8 m/s with an amplitude of 0.5 m are 334 % for the BEM results, 300 % for the coupled model and 292 % for the free wake code results. Generally, these deviations of the logarithmic decrement are not important for the computation of blade loads because flapwise modes are highly damped and will thus not contribute significantly to fatigue loads. On the other hand, the lower aerodynamic damping of flapwise blade motion will correspond to a lower aerodynamic damping of tower fore-aft motion and might thus lead to increased tower fatigue loads. However, the lower aerodynamic damping could be balanced by a decreased excitation of the tower fore-aft modes, because the near wake effects are likely to reduce the aerodynamic force variations due to atmospheric turbulence in the same way as they reduce the aerodynamic work due to blade motion.

Edgewise modes tend to have very low aeroelastic damping, which makes an accurate damping computation important. The aerodynamic damping estimations for the in-plane vibrations at 8 m/s are shown in Table 5.2. The damping has been estimated based on the computations with the first edgewise mode shape and an amplitude of 1 m in four different cases to separate the influence of the different parameters: Case (1) and (2) both use a lift gradient of 2π and zero drag. The difference between the first two cases is if the camber is included in the unsteady airfoil aerodynamics computations, cf. Equations (2.19-2.21) and (3.1). Case (3) uses the lift coefficient according the NREL 5 MW airfoil polars, but drag is ignored. Case (4) is based on both lift and drag coefficients of the NREL 5 MW reference turbine. Comparison of the first two cases of Table 5.2 shows that the induced drag caused by airfoil camber in the shed vorticity modeling is resulting in an aerodynamic damping of roughly 0.7 % logarithmic decrement. According to the BEM and coupled model results in case (3) and (4) the airfoil drag causes an estimated difference in logarithmic damping of about 0.3 % in this case with purely in-plane vibrations. The trailed vorticity consistently decreases the absolute value of the estimated logarithmic damping by roughly 0.14 %. Further, comparing columns (2) and (4), the combined influence of airfoil polars with lift coefficients other than 2π and drag is close to three times larger in the free wake code computations, which is likely to be caused by the different unsteady drag modeling. Although the differences in estimated logarithmic decrement are generally small, they might have an impact on loads computations for edgewise modes with an aeroelastic damping that is close to zero.

	Case 1 $C'_L = 2\pi$ $C_D = 0$ α_{QS}	Case 2 $C'_L = 2\pi$ $C_D = 0$ $\alpha_{QS} - \alpha_0$	Case 3 NREL C_L $C_D = 0$ $\alpha_{QS} - \alpha_0$	Case 4 NREL C_L NREL C_D $\alpha_{QS} - \alpha_0$
BEM	-1.13	-0.41	-0.52	-0.24
Coupled model	-1.00	-0.27	-0.37	-0.1
GENUVP	-	-0.25	-	0.22

Table 5.2: Estimated aerodynamic damping in logarithmic decrement [%] corresponding to the aerodynamic work of first in-plane vibrations at 8 m/s. The estimates are based on vibrations with an amplitude of 1 m. The values do not correspond to the damping of any aeroelastic mode, but are provided to evaluate the impact of the different aerodynamic models.

CHAPTER 6

Influence of trailed vorticity on flutter speed estimations, [IV]

The shed vorticity effects computed by 2D unsteady airfoil aerodynamics models have been found to be crucial for an accurate prediction of the critical flutter speed [6, 7]. The work presented in this chapter has been published in [IV] and is directed towards identifying the influence of trailed vorticity on the estimations of critical rotor speeds of modern wind turbines.

As opposed to the two previous chapters, which are showing results from purely aerodynamic computations, this chapter contains results from aeroelastic simulations. These simulations are run in HAWC2, either with the unsteady BEM model or the coupled near and far wake model, the latter version is denoted as HAWC2 NW in the following.

The next section is a short description of the runaway case that has been used to identify the critical rotor speeds, similar to the work in [9]. In Section 6.2, the main results from the stability investigations in [IV] are presented.

6.1 Runaway case

To find a critical speed at which an aeroelastic turbine mode becomes negatively damped, the turbine has been simulated in a runaway situation, where the generator torque and pitch angle are zero. The rotor will in this case approach a rotation speed where the aerodynamic torque is zero, due to negative torque from the outer part of the blade and positive torque from the in board sections. This terminal rotor speed depends only on the wind speed at the rotor. To approach the critical rotor speed where an instability occurs the wind speed can be slowly ramped up, thus continuously increasing the rotor speed until vibrations of the blades start to build up, cf. Figure 6.1. In general there is no disturbance other than numerical errors to start the vibration. In Section 6.2.1 the influence of turbulence as additional excitation on the flutter speed is evaluated.

Advantages of this approach compared to, for example, prescribing an increasing rotor speed through the generator torque at a fixed wind speed are:

- The runaway case is a better approximation of a real overspeed situation because no artificial forcing is necessary.
- The edgewise blade deflections are small because the rotor torque is close to zero. Edgewise deflection will change the coupling between flapwise, edgewise and torsional blade modes and change the flutter speed, in the same way as sweeping the blades would [9].
- The influence of the wind speed slope, which is the only relevant parameter for the simulation, is small, cf. Section 6.2.1.

In all observed cases, the instability will, since the rotor speed is free to change, first lead to small oscillations of the rotor speed and then to a significant decrease of the rotor speed, as energy from the rotation is transferred to vibrations of the blades. In the following flutter speed comparisons, the flutter speed has been determined at the time where the rotation speed in one time step is smaller than in the previous time step for the first time in the simulation except the transients at the start up, cf. Figure 6.2.

6.2 Stability investigations

6.2.1 Sensitivity to modifications of runaway case parameters

Figure 6.3 shows the sensitivity of the flutter speeds predicted using the HAWC2 and HAWC2 NW models to changes in ramping speed. It can be seen that over the range of ramping speeds the flutter speeds are changing only slightly, by about 3% if the near wake model is included and 5% if the traditional HAWC2 BEM model is used. Note that this small change in flutter speed is a consequence of changing the ramping speed by a factor of 16 from 0.00125 m/s^2 to 0.02 m/s^2. The predicted flutter speeds are higher for faster ramping speed, which might be partially because the instabilities need some time to build up. At faster ramping speeds the rotor accelerates faster, leading to a bigger increase in rotor speed between the first small blade oscillations and a decrease in rotor speed that is used here to mark the onset of the instability. Because the difference between HAWC2 and HAWC2 NW results is similar for different ramping speeds and slow ramps require long computations, all further computations

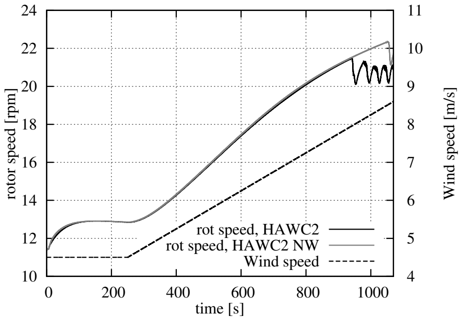

Figure 6.1: Principle of the runaway case: the wind speed is slowly ramped up and the rotor speed follows up to an instability. Comparison between HAWC2 with BEM and coupled near and far wake model.

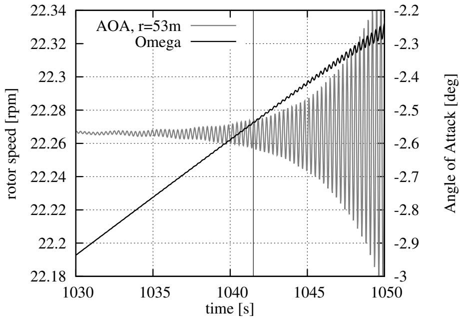

Figure 6.2: Zoom to the onset of vibrations. The black vertical line indicates the time interpreted here as the onset of flutter.

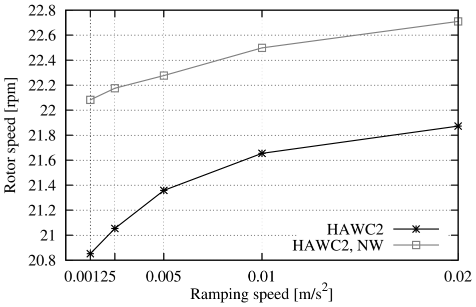

Figure 6.3: Sensitivity of flutter speed with respect to ramping speed.

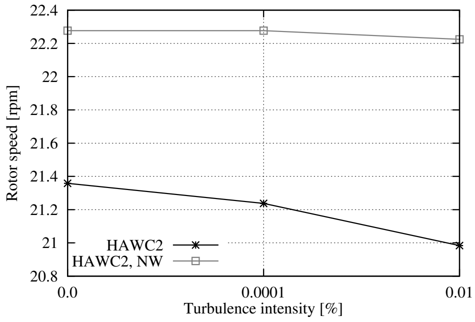

Figure 6.4: Sensitivity of flutter speed with respect to turbulence intensity.

have been performed using a wind ramp with a slope of 0.005 m/s^2.

In Figure 6.4 the influence of added turbulence is shown for low turbulence intensities. Turbulence decreases the flutter speed when the original HAWC2 model is used, but has almost no influence in case of the near wake model. In Section 6.2.2 it is shown that the reason for this difference is that two different modes can become unstable in HAWC2 at slightly different relative speeds if the standard blade is used. It seems that the mode that becomes unstable at lower wind speeds, which is different than the mode observed in HAWC2 NW, cf. Section 6.2.2, is more affected by turbulence than the other mode. Even though there is a clear influence of turbulence intensity on the offset between the flutter speeds predicted by the near wake model and the original HAWC2 model in this particular case, it has been decided to run all following computations without turbulence to avoid introducing an additional parameter.

6.2.2 Sensitivity to structural stiffness variations of the blade

Figure 6.5 shows the influence of the variation of both flapwise stiffness and torsional stiffness on the flutter speed. The cross section parameters Ix, the flapwise area moment of inertia, and Ip the torsional stiffness constant, have been varied from 70 to 130 % of the original values for the NREL 5 MW turbine, keeping all other parameters constant. Both models agree that an increase of torsional blade stiffness leads to an increased stability, as expected. The flutter speed increase due to increased torsional stiffness is comparable in both models.

The flapwise stiffness variation, however, leads to different results. In agreement with findings by Lobitz [8], the flapwise stiffness has a smaller influence on the flutter speed than the torsional stiffness. In the present work, the direction in which an increasing flapwise stiffness changes the flutter speed is found to depend on both the blade and the used aerodynamic model: For the blade with 130% torsional stiffness, both aerodynamics models agree on a reduced flutter speed for increasing the flapwise stiffness from 100% to 130%. The most interesting behavior can be seen when the flapwise stiffness is decreased from 100% to 70% for the otherwise unaltered blade. In this case the HAWC2 predicts a decrease in flutter speed, while HAWC2 NW shows an increased flutter speed. This case has been further investigated in [IV].

Analysis of the deflection shapes and frequencies showed different modes become unstable at the standard torsional stiffness and 70% flapwise stiffness. The computations

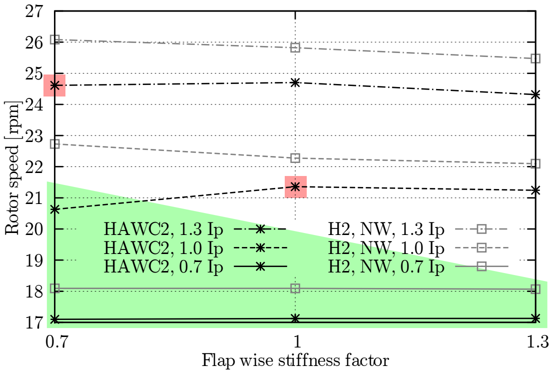

Figure 6.5: Sensitivity of flutter speed with respect to torsional and flapwise stiffness variations. The colors show the critical vibration modes: green indicates a backward whirling mode and white a symmetric flutter mode. Red indicates a whirling mode at small amplitudes, that quickly shifts to a symmetric mode.

with the unsteady BEM model predict a backward whirling flutter mode with a large edgewise content while the computations including trailed vorticity predict a symmetric flutter mode with negligible edgewise content. If the flapwise stiffness is increased to 130%, both models agree on the symmetric mode. This observation might explain the larger difference in critical rotor speeds at 70% flapwise stiffness, where different modes are predicted, and the smaller difference at 130%, where both models predict the same mode.

In the cases where both models predict self-induced vibrations in similar modes, the backward whirling mode at 70% torsional stiffness and the symmetric mode at 130% torsional stiffness, the influence of the increasing flapwise stiffness is quite different. The predicted critical rotor speeds are almost independent of the varying flapwise stiffness for the torsionally softer blade, while increasing flapwise stiffness leads to lower flutter speeds for the torsionally stiffer blade. An exception to this is the HAWC2 simulation at 130% torsional stiffness and 70% flapwise stiffness, where the vibration starts to build up in the whirling mode, shifting to the symmetric mode at higher amplitudes. Two opposing effects are expected if the flapwise stiffness is increased: The first effect is that the flapwise stiffness increases the flutter speed, which has been shown by Hansen for a 2D blade section [6]. This effect is negligible if the torsional stiffness is much larger than the flapwise stiffness but grows in importance at lower torsional stiffnesses. The second effect is that an increasing flapwise stiffness leads to a smaller ratio of torsional to flapwise eigenfrequencies, which is expected to reduce the critical flutter speed, [7]. A possible explanation for the different sensitivity to the varying flapwise stiffness is thus that both effects roughly cancel out for the torsionally softer blade. If the blade is stiffer in torsion, the first effect is weaker because the torsional stiffness dominates, but the torsional mode can easier couple with the flapwise mode at higher flapwise stiffness. Therefore the flutter speed decreases with increasing flapwise stiffness in the case of the blade with high torsional stiffness.

CHAPTER 7

Conclusions

7.1 Model

A coupled near and far wake model for wind turbine rotor aerodynamics has been presented and validated in this work. Several modifications compared to previous implementations have been shown to increase the accuracy and speed of the model. The near wake induction is iterated to convergence, using a dynamically computed relaxation factor. This iterative approach has removed the need for smaller time steps or aerodynamic sub time steps for stable computations. Due to these modifications, the model is now considered to be applicable in aeroelastic wind turbine simulations, without the need for user input that exceeds unsteady BEM computations. An exception to this are standstill cases, because the model has been developed for a rotating turbine. The model requires a higher computational effort than unsteady BEM modeling, but switching from an unsteady BEM model to the coupled model only slows down an aeroelastic wind turbine computation by few percent in the investigated cases.

7.2 Impact of trailed vorticity modeling

The aerodynamic force response to pitch steps and prescribed vibrations predicted by the coupled model have been shown to agree better with results from a more complex free wake panel code than results from an unsteady BEM model in all investigated cases. Selected vibration cases have also been computed using full rotor CFD. These computations confirmed the free wake results and showed a comparable improvement of the unsteady BEM modeling due to the added trailed vorticity effects. It has been found that changes of the dynamic angle of attack due to varying inflow velocity are important when computing the aerodynamic work response to vibrations nearly parallel to the inflow. Airfoil camber should be included in the unsteady airfoil aerodynamics modeling. The changes in the prediction of aerodynamic damping influence both load computations and stability analysis of wind turbines. A decreased excitation of the turbine vibrations due to atmospheric turbulence is expected if the trailed vorticity is modeled, which might balance the lower aerodynamic damping of the eigen modes in fatigue computations. For edgewise modes, however, which tend to have very low aeroelastic damping, the trailed vorticity modeling might change the sign of the aerodynamic damping, which will have a large impact on the load predictions.

The model has been applied to identify critical rotor speeds where aeroelastic instability occurs. These investigations have been based on runaway cases, where the generator torque is set to zero and the rotor is free to speed up. The free wind speed is low until a terminal rotor speed is reached. Then the wind speed is slowly increased, with the rotor speed following. It has been found that the slope of the wind speed ramp only has a small influence on the predicted flutter speeds, as well as additional excitation due to small turbulence intensity. The analysis has shown that the trailed vorticity modeling delays the onset of classical flutter towards four to ten percent higher rotor speeds for varying flapwise and torsional blade stiffness. Thus the trailed vorticity influences the blade dynamics in a similar way as the shed vorticity: Both decrease the aerodynamic damping of a flapwise mode and increase the flutter speeds.

7.3 Outlook

Future work on the coupled near and far wake model includes the implementation in the aeroelastic stability code HAWCStab2. This implementation requires a further simplification of the model to reduce the number of aerodynamic states necessary in a state space formulation. With the present implementation for time marching simulations, the effect of the trailed vorticity modeling on fatigue loads and extreme loads can be evaluated in a full load basis. In this context, the near wake model could be made more generally applicable for non-operation situations, such as standstill, where BEM modeling is usually disabled but the trailed vorticity modeling can be advantageous. Further validation of the model against high fidelity codes and measurements will increase the confidence in the model, also in cases of for example sheared and turbulent inflow and operation in yaw. However, the model already seems to produce superior results compared to unsteady BEM modeling, which justifies to use it more widely in aeroelastic wind turbine computations.

Bibliography

[1] Hansen MOL, Madsen HA. Review paper on wind turbine aerodynamics. *Journal of Fluids Engineering* 2011; **133**(11):114 001, doi:10.1115/1.4005031.

[2] Voutsinas SG. Vortex methods in aeronautics: How to make things work. *International Journal of Computational Fluid Dynamics* 2006; **20**:3–18.

[3] Sørensen N. General purpose flow solver applied to flow over hills. PhD Thesis 1995. Published 2003.

[4] Heinz J, Sørensen N, Zahle F. Partitioned fluid-structure interaction for full rotor computations using cfd. PhD Thesis 2013.

[5] *IEC 61400-1 Ed. 3, Wind Turbines. Part 1: Design Requirements*. 2005.

[6] Hansen MH. Aeroelastic instability problems for wind turbines. *Wind Energy* 2007; **10**:551–577.

[7] Lobitz DW. Aeroelastic stability predictions for a MW-sized blade. *Wind Energy* 2004; **7**:211–224.

[8] Lobitz DW. Parameter sensitivities affecting the flutter speed of a MW-sized blade. *Journal of Solar Energy Engineering, Transactions of the ASME* 2005; **127**(4):538–543.

[9] Hansen MH. *Aeroelastic properties of backward swept blades*, Proceedings of 49th AIAA Aerospace Sciences Meeting Including The New Horizons Forum and Aerospace Exposition, Orlando, 2011.

[10] Lindenburg C. Bladmode, program for rotor blade mode analysis. *ECN-C–02-050* 2003; .

[11] Riziotis VA, Voutsinas SG, Politis ES, Chaviaropoulos PK. Aeroelastic stability of wind turbines: the problem, the methods and the issues. *WIND ENERGY* 2004; **7**(4):373–392, doi:10.1002/we.133.

[12] Snel H, Schepers JG, Editors. Joint investigation of dynamic inflow effects and implementation of an engineering method. *ECN-C–94-107* 1995; .

[13] Theodorsen T. General theory of aerodynamic instability and mechanism of flutter. *National Advisory Committee for Aeronautics – Reports* 1935; .

[14] Wilson R, Lissaman P. *Applied aerodynamics of wind power machines*. Oregon State University, 1974.

[15] Leishman J. *Principles of Helicopter Aerodynamics*. Cambridge Aerospace Series, Cambridge University Press, 2002.

[16] Beddoes TS. A near wake dynamic model. *proc. of the AHS national specialist meeting on aerodynamics and aeroacoustics* 1987; .

[17] Madsen HA, Rasmussen F. A near wake model for trailing vorticity compared with the blade element momentum theory. *Wind Energy* 2004; **7**:325–341.

[18] Larsen TJ, Hansen AM. *How 2 HAWC2, the user's manual.* Denmark. Forskningscenter Risoe. Risoe-R-1597, 2007.

[19] Kim T, Hansen AM, Branner K. Development of an anisotropic beam finite element for composite wind turbine blades in multibody system. *Renewable Energy* 2013; **59**:172.

[20] Larsen TJ, Madsen HA, Larsen GC, Hansen KS. Validation of the dynamic wake meander model for loads and power production in the egmond aan zee wind farm. *Wind Energy* 2013; **16**(4):605–624, doi:10.1002/we.1563.

[21] Madsen Aagaard H, Mikkelsen R, Sørensen N, Hansen M, Øye S, Johansen J. *Influence of wind shear on rotor aerodynamics, power and loads.* Denmark. Forskningscenter Risoe. Risoe-R-1611, 2007; 101–116.

[22] Sørensen NN, Madsen HA. *Modelling of transient wind turbine loads during pitch motion (paper and poster).* European Wind Energy Association (EWEA), 2006.

[23] Madsen HA, Riziotis V, Zahle F, Hansen MOL, Snel H, Grasso F, Larsen TJ, Politis E, Rasmussen F. Blade element momentum modeling of inflow with shear in comparison with advanced model results. *Wind Energy* Jan 2012; **15**:63–81, doi:10.1002/we.493.

[24] Fung Y. *An Introduction to the Theory of Aeroelasticity.* Phoenix Edition Series, Dover Publications, 2002.

[25] Hansen MH, Gaunaa M, Madsen HA. *A Beddoes-Leishman type dynamic stall model in state-space and indicial formulations.* Risø-R-1354: Roskilde, Denmark, 2004.

[26] Jones RT. The unsteady lift of a wing of finite aspect ratio. *CASI* 1976; .

[27] Buhl T, Gaunaa M, Bak C. Potential load reduction using airfoils with variable trailing edge geometry. *Journal of Solar Energy Engineering* 2005; **127**(4):503–516, doi:10.1115/1.2037094.

[28] Andersen PB. PhD Thesis, Risø DTU 2010.

[29] Wang T, Coton FN. A high resolution tower shadow model for downwind wind turbines. *Journal of Wind Engineering and Industrial Aerodynamics* 2001; **89**:873–892.

[30] Madsen HA, Gaunaa M. *Udvikling af model for 3D induktions- og stallmodellering.* Risø-R-1509(DA): Roskilde, Denmark, 2004.

[31] van Garrel A. *Development of a wind turbine aerodynamics simulation module.* ECN report ECN-C–03-079, 2003.

[32] Jonkman J, Butterfield S, Musial W, Scott G. Definition of a 5-mw reference wind turbine for offshore system development. *Technical Report*, National Renewable Energy Laboratory 2009.

[33] Petot D. Differential equation modeling of dynamic stall. *La Recherche Aerospatiale(English Edition)* 1989; (5):59–72.

[34] Riziotis VA, Voutsinas SG. *Dynamic Stall on Wind Turbine Rotors: Comparative Evaluation Study of Different Models*, Proceedings of the 1997 European Wind Energy Conference and Exhibition, 1997.

[I]

Improvement of a near wake model for trailing vorticity

Improvement of a near wake model for trailing vorticity

GR Pirrung, MH Hansen, HA Madsen

Department of Wind Energy, Technical University of Denmark, Frederiksborgvej 399,
DK-4000, Roskilde

E-mail: `gepir@dtu.dk`

Abstract. A near wake model, originally proposed by Beddoes, is further developed. The purpose of the model is to account for the radially dependent time constants of the fast aerodynamic response and to provide a tip loss correction. It is based on lifting line theory and models the downwash due to roughly the first 90 degrees of rotation. This restriction of the model to the near wake allows for using a computationally efficient indicial function algorithm. The aim of this study is to improve the accuracy of the downwash close to the root and tip of the blade and to decrease the sensitivity of the model to temporal discretization, both regarding numerical stability and quality of the results. The modified near wake model is coupled to an aerodynamics model, which consists of a blade element momentum model with dynamic inflow for the far wake and a 2D shed vorticity model that simulates the unsteady buildup of both lift and circulation in the attached flow region. The near wake model is validated against the test case of a finite wing with constant elliptical bound circulation. An unsteady simulation of the NREL 5 MW rotor shows the functionality of the coupled model.

1. Introduction

The dynamic effects of trailed vorticity behind a wind turbine blade on the induced velocities at the blade are considered with a focus on the influence on the aeroelastic behavior. In many state of the art codes for wind turbine aeroelasticity, the unsteady aerodynamics are computed using a blade element momentum (BEM) model with several additions, such as tip loss correction and dynamic stall model, cf. Madsen et al. [1]. In a BEM model, the momentum equation is solved at different radial sections of the rotor independently, ensuring that the induced velocities are in balance with the forces at the blades. Unsteady effects are usually also modeled for each section independently, such as dynamic inflow, which takes into account that the turbine wake development delays the response to changes in wind speed or pitch, or unsteady airfoil aerodynamics, which model the faster time lags in the change of lift due to airfoil motion, turbulence and flow separation.

In reality, the flow at different radial sections is coupled through the wake, which can be modeled as trailed and shed vorticity. According to Leishman [2], the effects of the shed wake are mostly local and the overall aerodynamics along the blade are mainly depending on the trailed wake, where the most important contribution comes from the tip vortex. The influence of the trailed vortices is often computed with a BEM model combined with a tip loss model to account for the increased induction at the tip due to the finite number of blades. Due to the assumption of radial independence in the BEM formulation and because the dynamic inflow time constants are a function only of radius, the present modeling does not predict accurately the time varying trailed vorticity along the blade due to turbulence or blade vibrations.

Beddoes [3] has developed a near wake model that accounts for the unsteady trailed vorticity. It is based on a lifting line model, which is restricted to the first quarter revolution behind a single blade. This restriction makes it possible to use exponential functions to model the decreasing induction from trailed vortex filaments as the blade moves away from them. Madsen and Rasmussen [6] implemented the model for use on wind turbine aeroelasticity. and demonstrated the models basic capability to compute the aerodynamic damping as function of mode shape and not only as function of radius. The original model did not include downwind convection of the vortex filaments away from the rotor plane, but Wang and Coton [4] included the influence tilt angle of the trailed vortices in the axial induction. Andersen [5] added an optimization method for the exponential functions to reduce errors due to the approximation of the induction, compared to the exact evaluation of the Biot-Savart law.

Madsen and Rasmussen [6] suggested to couple the near wake model with a BEM model for the far wake. This BEM model would not include a tip loss correction, because that is implicitly included in the near wake model. The thrust coefficient, on which the computation of the induction using a BEM model is based on, is reduced by a coupling factor. In their work, the bound vorticity for the near wake model has been determined using Joukowski's law, which states that the steady circulation is proportional to the steady lift.

In this work, the core algorithm of the near wake model has been altered to ensure that the downwash due to trailed vortex elements is calculated with the same precision independent of their size and distance from the blade section. Also the influence of the spatial discretization of the blade on the results is investigated, using three different point distributions. An iterative solution scheme with a relaxation factor is introduced to ensure the stable behavior of the near wake model, especially as part of a coupled aerodynamics model. Joukowski's law, the proportionality of lift and circulation, does not hold for unsteady calculations. Therefore the unsteady circulation is determined separately in the attached flow region, analogue to the unsteady lift in the dynamic stall model by Hansen et al. [7].

With these additions, the modeling of the development of the downwash on a wing with a constant elliptical circulation becomes independent of the time step and converges consistently to the analytical steady state solution. It is shown that the altered trailing algorithm is also faster than the original version. To show the capabilities of the coupled model to handle the unsteady case, it has been used to simulate the aerodynamics of the NREL 5 MW reference turbine. The steady induction agrees well with results from a code comparison [1].

This paper is structured as follows: First, the near wake model and its modifications are described. Then the coupled model is introduced. Finally, results from both near wake model and coupled model are presented.

2. Description of the near wake model

In this section the near wake model is introduced, starting with the original model by Beddoes and followed by a modified version of the vortex trailing algorithm, which is less time step dependent. Furthermore, different point distribution methods and a stabilization of the model through an iterative computation of the downwash are presented. In the last part of the section, a brief outline of the coupling to a far wake model is given.

2.1. Original model by Beddoes, modified by Madsen and Rasmussen

Based on the Biot-Savart law, the induced downwash of a vortex filament with length $\mathrm{d}s$ and vortex strength $\Delta\Gamma$, which is trailed from radius r at a point on the blade and stays in the rotor blade, cf. Figure 1, can be evaluated as

$$\mathrm{d}w = \frac{\Delta\Gamma\,\mathrm{d}s}{4\pi r^2}\,\frac{1-\left(1-\frac{h}{r}\right)\cos(\beta)}{\left[1+\left(1-\frac{h}{r}\right)^2-2\left(1-\frac{h}{r}\right)\cos(\beta)\right]^{3/2}}, \tag{1}$$

where h is the distance between the vortex trailing point and the calculation point where the downwash is evaluated. The value of h is negative when the vortex is closer to the blade root than the section. The angle $\beta = \Omega t$ determines the position of the infinitesimal vortex element on the circular arc, the angle the rotor has rotated with the constant angular velocity Ω since the vortex filament has been trailed from the blade. The downwash from the circular arc could be evaluated by numerically integrating Equation (1) from 0 to 90 degrees.

To avoid these time consuming integrals, Beddoes derived an equation that gives the decrease of the induction by a vortex filament $\mathrm{d}w$ compared to its original induction $\mathrm{d}w_0$, when it has just left the lifting line. This equation is then approximated using two exponential functions:

$$\frac{\mathrm{d}w}{\mathrm{d}w_0} = \frac{\left(\frac{h}{r}\right)^2\left[1-\left(1-\frac{h}{r}\right)\cos(\beta)\right]}{\left[1+\left(1-\frac{h}{r}\right)^2-2\left(1-\frac{h}{r}\right)\cos(\beta)\right]^{3/2}} \approx 1.359e^{-\beta/\Phi}-0.359e^{-4\beta/\Phi}, \tag{2}$$

where Φ is a geometric factor depending on the positions of vortex trailing point and calculation point:

$$\Phi = \frac{\pi}{4}\left|\left(1+\frac{h}{2r}\right)\ln\left(1-\frac{h}{r}\right)\right|. \tag{3}$$

Madsen and Rasmussen [6] replaced the term 1 + h/(2r) by 0.75 for cases where h/(2r) is smaller than -0.25, which increases the accuracy of the exponential approximation when the vortex trailing point lies further inboard than the calculation point for the induced downwash. This modification is used in the calculations presented here.

The computational effort can be dramatically reduced by using the exponential functions. The downwash W can then be split into two contributions [3]:

$$W^i = X_w^i + Y_w^i, \tag{4}$$

where the index i denotes the time step and X_w and Y_w are state variables that represent the slowly and quickly decreasing components of the induction from the near wake according to Equation (2):

$$X_w^i = X_w^{i-1}e^{-\Delta\beta/\Phi} + 1.359D_w e^{-\Delta\beta/2\Phi} \tag{5a}$$

$$Y_w^i = Y_w^{i-1}e^{-4\Delta\beta/\Phi} - 0.359D_w e^{-2\Delta\beta/\Phi}, \tag{5b}$$

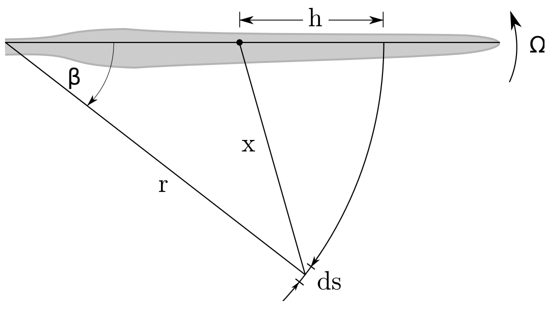

Figure 1. Geometry at a blade rotating with the constant angular velocity Ω. The downwash at a distance h from the vortex trailing point shall be computed. Since the infinitesimal vortex element with length ds has left the lifting line, the blade has been rotated by the angle β.

where $\Delta\beta = \Omega\Delta t$ is the azimuthal angle traveled in one time step Δt. The components X_w^{i-1} and Y_w^{i-1} from the last time step contain the complete induction from the old circular arc. These values are then multiplied by exponential factors, which depend on $\Delta\beta$, and the positions of vortex trailing point and calculation point, through their influence on the geometric factor Φ. The second terms on the right hand side of Equation (5) contain the induction due to the new finite length vortex filament D_w, which has been trailed during the time step. This induction D_w is computed using the Biot-Savart-law, assuming the newest element is a straight vortex with length Δs and perpendicular to the lifting line [3]:

$$D_w = \frac{\Delta\Gamma\left(\frac{\Delta s}{h}\right)}{4\pi r\frac{h}{r}\left[1+\left(\frac{\Delta s}{h}\right)^2\right]^{1/2}}, \tag{6}$$

where $\Delta\Gamma$ is the strength of the vortex. The contributions from X_w and Y_w to the induction D_w from the newest element are depending on its length, because Y_w decreases four times faster with increasing angle β than X_w, cf. Figure 2. In Equation (5), D_w is multiplied not only by 1.359 and -0.359, but also by the respective exponential factors corresponding to the middle of the element to take this length dependence into account. As shown in Figure 2, this gives not only the desired approximation of the contributions from X_w and Y_w, but also leads to an underestimation of the induction due to the newest element, because the exponential factors do not add up to 1 for a finite element length. The error due to this underestimation is growing with increasing time step and decreasing distance between calculation point and vortex trailing point.

2.2. New formulation of the trailing algorithm

The purpose of the modification explained in the following is to ensure a time step independent behavior of the trailing algorithm in case of a prescribed, constant circulation. Because the circulation is constant, this time step independence means that trailed vortex elements are evaluated correctly independent of their size, which varies with the time step. The decrease of induction from the old part of the wake, the first terms on the right hand side of Equation (5), is already time step independent, because $e^x e^x = e^{2x}$. Therefore, to make the whole algorithm time step independent, both the value of the initial downwash D_w and the way it is split into X_w and Y_w have to be corrected.

Instead of calculating a D_w for the whole first time step, the $\Delta s = \Delta\beta r$ in equation (6) is replaced by $\tilde{\beta} r$:

$$\tilde{D}_w = \frac{\Delta\Gamma\left(\frac{\tilde{\beta} r}{h}\right)}{4\pi r\frac{h}{r}\left[1+\left(\frac{\tilde{\beta} r}{h}\right)^2\right]^{1/2}}, \tag{7}$$

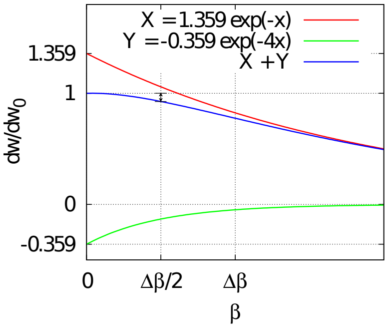

Figure 2. Illustration of the exponential trailing functions. The black mark indicates the underestimation of the induction due to the multiplication of D_w by the exponential factors in Equation (5) for an element with length $\Delta\beta$.

where $\tilde{\beta}$ is a constant, very small angle, for which the induction is approximately constant along the vortex filament: $\mathrm{d}w/\mathrm{d}w_0 \approx 1$ for $\beta \in [0;\tilde{\beta}]$. In the simulations presented here $\tilde{\beta} = 10^{-10}$ rad has been used.
The induction D_w for the first time step Δt can then be approximated as:

$$D_w = \tilde{D}_w \frac{\Delta\beta}{\tilde{\beta}} \left\langle \frac{\mathrm{d}w}{\mathrm{d}w_0} \right\rangle, \tag{8}$$

where $< \mathrm{d}w/\mathrm{d}w_0 >$ denotes the average value of $\mathrm{d}w/\mathrm{d}w_0$ given in Equation (2) over the whole length of the newest element. This average can be obtained by integrating:

$$\begin{aligned} D_w &= \tilde{D}_w \frac{\Delta\beta}{\tilde{\beta}} \frac{1}{\Delta\beta} \int_0^{\Delta\beta} \frac{\mathrm{d}w}{\mathrm{d}w_0}\, d\beta \\ &= \frac{\tilde{D}_w}{\tilde{\beta}} \int_0^{\Delta\beta} (1.359 e^{-\beta/\Phi} - 0.359 e^{-4\beta/\Phi})\, d\beta \\ &= \frac{\tilde{D}_w \Phi}{\tilde{\beta}} [1.359(1 - e^{-\beta/\Phi}) - \frac{0.359}{4}(1 - e^{-4\beta/\Phi})] \end{aligned} \tag{9}$$

For small values of $\tilde{\beta}$, which can be chosen independent of the time step, this is a good approximation of the downwash induced by the first vortex filament. The error due to calculating D_w based on a straight vortex filament is replaced by the error caused by using Beddoes' functions. As opposed to the way D_w is obtained before, it can be consistently split in X_w and Y_w, which leads to a modified version of Equation (5):

$$X_w^i = X_w^{i-1} e^{-\Delta\beta/\Phi} + 1.359 \frac{\tilde{D}_w \Phi}{\tilde{\beta}} (1 - e^{-\Delta\beta/\Phi}) = X_w^{i-1} e^{-\Delta\beta/\Phi} + D_X \Delta\Gamma (1 - e^{-\Delta\beta/\Phi}) \tag{10a}$$

$$Y_w^i = Y_w^{i-1} e^{-4\Delta\beta/\Phi} - 0.359 \frac{\tilde{D}_w \Phi}{4\tilde{\beta}} (1 - e^{-4\Delta\beta/\Phi}) = Y_w^{i-1} e^{-4\Delta\beta/\Phi} + D_Y \Delta\Gamma (1 - e^{-4\Delta\beta/\Phi}). \tag{10b}$$

The implementation of the new algorithm shows another advantage: In addition to ϕ and h also the factors D_X and D_Y for the induction from the new vortex elements are constant for each combination of calculation point and vortex trailing point. Therefore they can be computed once, at the initialization of the model,

$$D_X = 1.359 \frac{\tilde{D}_w \Phi}{\tilde{\beta} \Delta\Gamma} = 1.359 \left(\frac{\Phi r}{4\pi h^2} \right) \left[1 + \left(\frac{\tilde{\beta} r}{h} \right)^2 \right]^{-1/2} \tag{11a}$$

$$D_Y = -0.359 \frac{\tilde{D}_w \Phi}{4\tilde{\beta} \Delta\Gamma} = -0.359 \left(\frac{\Phi r}{16\pi h^2} \right) \left[1 + \left(\frac{\tilde{\beta} r}{h} \right)^2 \right]^{-1/2}, \tag{11b}$$

which was not possible in the original algorithm, as Δs in Equation (6) for D_w is not a constant. Furthermore, only two instead of four evaluations of exponential functions are necessary.

2.3. Influence of helical pitch angle, Wang and Coton

So far it has been assumed by Beddoes that the vortices are trailed in the rotor plane. In reality the vortices move in the helical wake. Wang and Coton [2] took this into account by including the pitch angle φ of the vortex path in the calculation of the axial induction. For an inflow perpendicular to the rotor plane and assuming a constant helical pitch, that angle can be defined as

$$\tan(\varphi) = \frac{V_\infty - w_a}{\Omega r + w_t}, \tag{12}$$

where V_∞ is the free stream velocity, w_a and w_t the axial and tangential induction, assumed to be constant in the annular tube, and Ω the rotational speed. The axial part of D_w is:

$$D_{w,a} = D_w \cos(\varphi). \tag{13}$$

This calculation of $D_{w,a}$ does not contain the increasing distance of the vortex filaments from the blade sections as they move downwind. The error due to neglecting the downwind convection is further investigated by Pirrung et al. [8].

2.4. Discretization of the blade

The algorithm used in this paper distinguishes between two kinds of points: vortex trailing points and calculation points. At the calculation points, the downwash, lift and circulation are determined. The circulation difference of two neighboring calculation points is then trailed at the vortex trailing point between them. At root and tip of the blade the vortex strength is the complete circulation of the nearest calculation point. Three different ways of distributing the points along the blade have been investigated:

- The **equidistant** distribution gives a constant resolution along the blades. The vortices are trailed from the root and tip of the blade, which is discretized in n sections, each with a vortex trailing point at both ends and a calculation point in the middle.
- The **cosine** distribution places the vortex trailing points at equal angle of a half circle over the blade, cf. Figure 3. The calculation points of the sections are placed in the middle of two trailed vortices.
- The **full cosine** distribution, which is used in the AWSM code [9] places the calculation points and vortex positions at equi-angle increments, also shown in Figure 3.

Figure 4 shows an example of how a continuous elliptical circulation is represented by constant values at the calculation points for the different point distributions.

2.5. Numerical stability

The near wake model can become numerically unstable if the downwash induced by the vortex filaments that have been trailed in one time step is so big that the predicted induction starts to diverge. The downwash will then lead to a negative lift of a bigger absolute value than the positive lift in the previous time step. The resulting trailed filaments with a vortex strength of the opposite sign will induce an even bigger negative downwash. If this is the case, the circulation and downwash can reach unphysical values in a few time steps.

The instability occurs especially for bigger time steps and close positions of calculation point and vortex trailing point, for example close to the tip when a cosine or full cosine distribution is used. Then the influence of the wake of the previous time step, that would stabilize the algorithm, decays quickly. The 2D shed vorticity effects on lift and circulation also stabilize the model. The problem of instability can be solved by running an iterative version of the NWM with the relaxation factor r:

$$W_r^j = W^{j-1} r + W^j (1 - r), \tag{14}$$

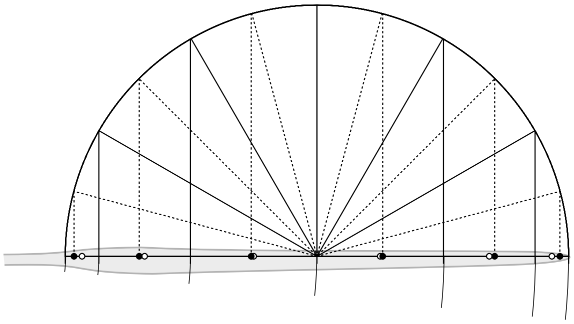

Figure 3. Sketch of the cosine and full cosine point distribution. The calculation points are placed at the positions marked by white (cosine) or black (full cosine) dots.

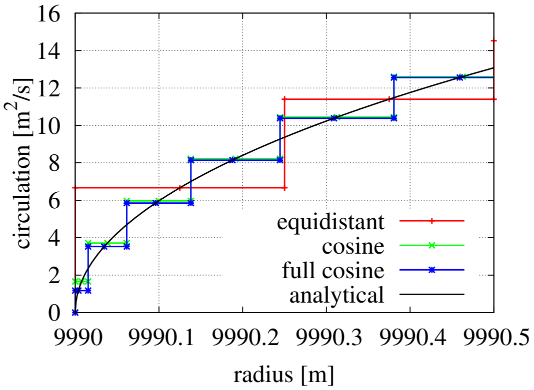

Figure 4. Resolution of an elliptical circulation close to the edge of the wing investigated in section 3 for the different point distributions.

where j denotes the iteration. This iterative process is used in the following coupled model. A more detailed explanation of the mechanism of instability and an estimation of the necessary relaxation factor depending on point distribution, time step and the shed vorticity model are given by Pirrung et al. [8].

2.6. Coupling to a far wake model

Because the near wake model only takes a fraction of one rotor revolution into account, it has to be coupled with a far wake model that calculates the induction from the missing part of the wake. A BEM model is used for this purpose. To consider the fraction of the induction that is computed by the near wake model, the thrust coefficient from the BEM model is multiplied by the coupling factor k_{FW} [5, 6], which depends on the operating conditions of the turbine. It is defined as:

$$C_{T,FW} = C_{T,BEM} k_{FW}, \qquad k_{FW} < 1 \tag{15}$$

where $C_{T,BEM}$ denotes the thrust coefficient obtained from the momentum balance of induced velocities without the near wake model and $C_{T,FW}$ is the reduced thrust coefficient used when the far wake BEM is coupled to the near wake model. The coupling factors used in this work are the result of simulations where the integral thrust coefficient from a coupled model has been matched with a BEM model with tip loss correction for the investigated operating conditions, as suggested by Andersen [5]. This matching ensures that steady state results from the coupled model agree with the classical BEM model for different combinations of wind speed, rotational speed and pitch angle. The structure of the coupled model is shown in algorithm 1. It includes the unsteady effects on circulation (cf. Pirrung et al. [8]) and on lift, the NWM and the BEM model with reduced thrust coefficient for the far wake.

3. Results

The modifications of the NWM are investigated for a wing with elliptical circulation. Simulations of the NREL 5 MW reference turbine [10] show the capabilities of the coupled model.

3.1. Near wake model: elliptical wing with prescribed circulation

A wing with a prescribed elliptical circulation has been used to investigate the influence of the spatial and temporal discretization. It is modeled as a 10 m long section at the end of a 10 km

Algorithm 1 One time step of the coupled model with near wake and far wake induction

```
while NOT convergence do
    AOA=AOA(W_iter), vrel=vrel(W_iter)
    calculate quasisteady lift and circulation
    apply unsteady airfoil aerodynamics model to lift and circulation
    call BEM(CT*$k_{FW}$)
    call NWM(unsteady circulation)
    W_iter=W_lastiter_NW*r+W_iter_NW*(1-r)+W_iter_FW
    if abs(W_iter-W_lastiter)< $\varepsilon$ then convergence = true
end while
```

long blade to approximate a parallel free stream, similar to the case presented by Madsen and Rasmussen, [6]. The circulation at radius r is given as

$$\Gamma = 30\,\frac{\mathrm{m}^2}{\mathrm{s}}\sqrt{(1-((r-9995\,\mathrm{m})/5\,\mathrm{m})^2)}, \tag{16}$$

which results in a constant downwash of 1.5 m/s along the wing according to lifting line theory. The blade rotates with 0.03359 rpm, which is equivalent to a free stream velocity at the wing of about 35 m/s.

To investigate the effect of the different spatial discretizations introduced in Section 2.4, Figure 5 shows the downwash of the near wake model in steady state for a 175 m long wake. The blade is discretized with 40 (left plot) or 80 (right plot) calculation points, corresponding to 41 and 81 vortex trailing points. While all spatial distributions perform well in the middle sections, the equidistant and cosine distribution lack accuracy close to the edges of the wing. They even lead to negative downwash in the outer sections of the blade.

To show the time step independence of the proposed method to obtain the downwash of the newest trailed filament described in Section 2.2, Figure 6 shows plots of the buildup of the downwash induced by the wake trailed from the wing with prescribed elliptical circulation. At the beginning of the simulation, $t = 0$, there is no trailed wake and therefore no downwash. The

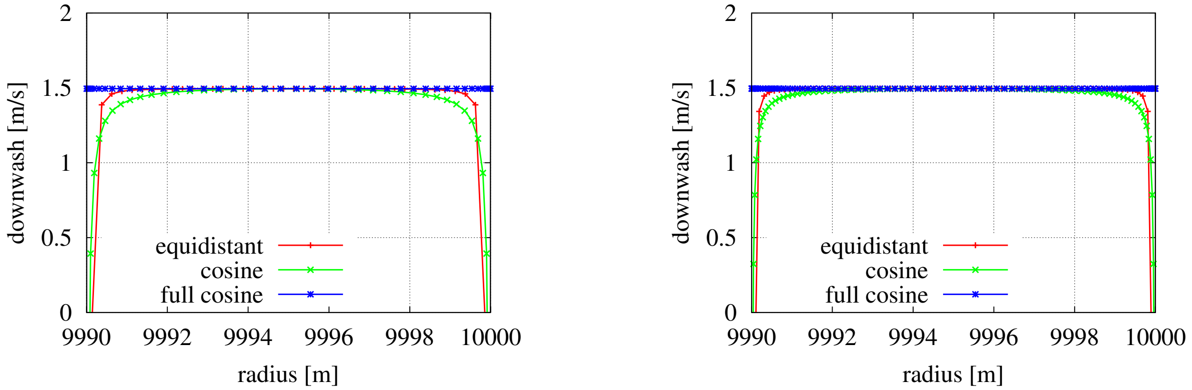

Figure 5. Comparison of the steady downwash at an elliptical wing with a wake of 175 m length. The calculation points and vortex trailing points have been distributed using the distribution methods described in Section 2.4. The blade has been discretized using 40 (left plots) or 80 (right plots) calculation points.

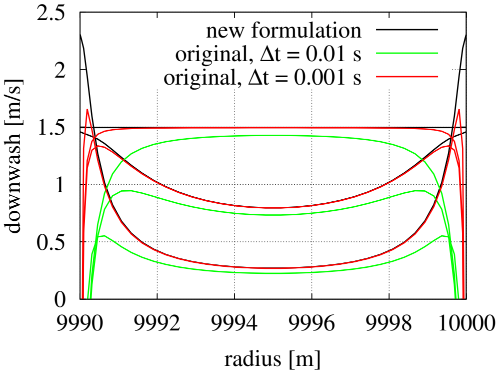

Figure 6. Buildup of induced velocities at the elliptical wing with a prescribed circulation at t=0.01 s, t=0.05 s and t=5.0 s, corresponding to 35 cm, 1.75 m and 175 m long trailed wakes. The new formulation, Equation (10), leads to the same results, independent of the time step.

plots of each color represent the distribution of the downwash after $t = 0.01$ s, $t = 0.05$ s and $t = 5$ s. A full cosine distribution with 40 sections has been used to discretize the wing. The new formulation proposed in Section 2.2 is compared to the original algorithm, Equation (5), for time steps of 0.01 s and 0.001 s. For all computations the downwash in the middle of the wing is increasing over time. The model based on the new formulation reaches a constant downwash of 1.4949 m/s along the wing after 5 s simulated time, which is close to the analytical steady solution of 1.5 m/s. Close to the middle of the wing Beddoes' algorithm agrees well with the new formulation for a time step of 0.001 s, but the accuracy gets worse towards both ends of the wing. If the original algorithm is used with a time step of 0.01 s, the downwash is significantly underestimated on the whole wing, again with the biggest errors at the ends.

3.2. Coupled model: NREL 5 MW reference turbine blade

Steady results of the coupled model for the NREL 5 MW reference turbine [10] are shown in Figure 7. The wind speed in the computation is 8 m/s, perpendicular to the rotor plane, and the rotational speed 9.21 rpm. The blade pitch angle is 0°. At the first 10 meters of radius, where there are no aerodynamic profiles, all the induction due to the root vortex is accounted for by the near wake model. Along large parts of the blade, the relatively constant induction due to the BEM model dominates, but closer to the tip the ability of the near wake model to capture the tip vortex becomes apparent. The combined axial induction from near and far wake agrees well with the code comparison results by Madsen et al. [1].

The thrust coefficients due to near wake, far wake and complete wake for an unsteady simulation are shown in Figure 8. The wind speed and rotational speed are identical as in the steady simulation. For simplicity, the dynamic inflow model used for the far wake had a dimensionless time constant of 1, independent of the radial position. After 100 seconds, the blades start to perform synchronous prescribed vibrations with an amplitude of 0.25 m and a frequency of 1 Hz perpendicular to the rotor plane. The shape of these vibrations is assumed to be the mode shape of a clamped-free prismatic beam. It can be seen that the unsteady aerodynamic effects due to these vibrations are mostly modeled by the near wake model. At 110 s, a pitch step of 4° within 0.5 seconds is performed, where the coupled model captures both fast and slow parts of the response.

4. Conclusions

The sensitivity to the spatial discretization of a near wake model, originally proposed by Beddoes, has been investigated. It was found that the case of a prescribed elliptic circulation could be modeled with better accuracy using a distribution based on equi-angle increments between calculation points and vortex trailing points as opposed to an equidistant distribution.

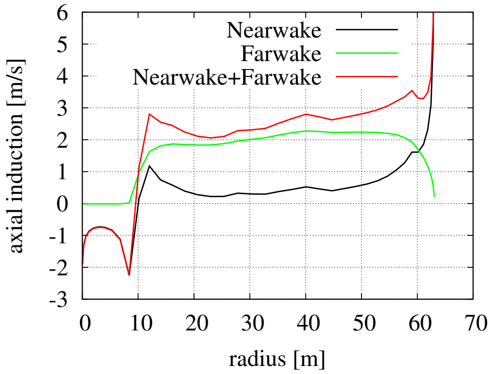

Figure 7. Induction due to near and far wake for the NREL 5MW rotor.

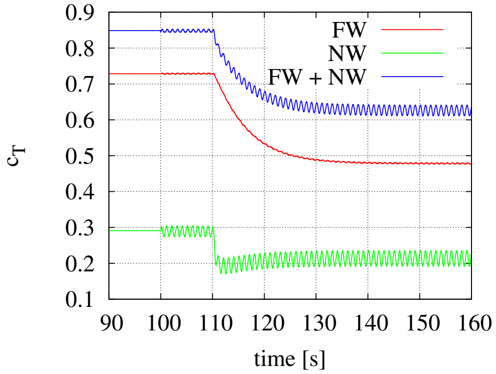

Figure 8. Integral C_T of the NREL rotor with a pitch step and blade vibrations.

To overcome the high sensitivity of the model on the time step a new formulation of the trailing wake algorithm based on integration of the trailing functions has been developed. This formulation makes the calculation of the downwash time step independent for a constant trailed vorticity, which means that trailed vortex elements are evaluated with the same accuracy, independent of their size. Therefore the modified algorithm can be used with bigger time steps. In addition to that, each time step is computed faster because larger parts of the algorithm can be computed once in the initialization of the program.

The model has been stabilized by introducing an iterative solution of the downwash from the near wake at each time step. The near wake model is coupled to the traditional BEM model of the far wake induction by sharing of the total induction through a coupling factor. The coupled model includes unsteady shed vorticity effects for both lift and circulation in the region of attached flow and a blade element momentum model for the far wake. The steady and unsteady behavior of the model has been illustrated based on the NREL 5 MW reference turbine. The coupled model agrees well with established models with regard to the distribution of axial induction and is capable of modeling the unsteady aerodynamic effects at different time scales.

References

[1] Madsen H A, Riziotis V, Zahle F, Hansen M O L, Snel H, Grasso F, Larsen T J, Politis E and Rasmussen F 2012 Blade element momentum modeling of inflow with shear in comparison with advanced model results *Wind Energy* **15** 63–81

[2] Leishman J 2002 *Principles of Helicopter Aerodynamics* Cambridge Aerospace Series (Cambridge University Press) ISBN 9780521523967

[3] Beddoes T S 1987 A near wake dynamic model *proc. of the AHS national specialist meeting on aerodynamics and aeroacoustics*

[4] Wang T and Coton F N 2001 A high resolution tower shadow model for downwind wind turbines *Journal of Wind Engineering and Industrial Aerodynamics* **89** 873–892

[5] Andersen P B 2010 Ph.D. thesis Risø DTU

[6] Madsen H A and Rasmussen F 2004 A near wake model for trailing vorticity compared with the blade element momentum theory *Wind Energy* **7** 325–341

[7] Hansen M H, Gaunaa M and Madsen H A 2004 *A Beddoes-Leishman type dynamic stall model in state-space and indicial formulations* (Roskilde, Denmark: Risø-R-1354)

[8] Pirrung G R, Hansen M H and Madsen H A 2012 *A stable near wake model for unsteady aeroelastic rotor simulations* (To be submitted)

[9] van Garrel A 2003 *Development of a wind turbine aerodynamics simulation module* (ECN report ECN-C–03-079)

[10] Jonkman J, Butterfield S, Musial W and Scott G 2009 Definition of a 5-mw reference wind turbine for offshore system development Tech. rep. National Renewable Energy Laboratory

[I]

Improvement of a near wake model for trailing vorticity

WIND ENERGY
Wind Energ. 0000; **00**:1–15
DOI: 10.1002/we

RESEARCH ARTICLE

A Coupled Near and Far Wake Model for Wind Turbine Aerodynamics

G. R. Pirrung, H. A. Madsen, T. Kim and J. Heinz

Wind Energy Department, Technical University of Denmark, Frederiksborgvej 399, Building 118, DK-4000 Roskilde, Denmark

ABSTRACT

In this paper an aerodynamic model consisting of a lifting line based trailed vorticity model and a blade element momentum (BEM) model is described. The focus is on the trailed vorticity model, which is based on the near wake model by Beddoes and has been extended to include the effects of downwind convection and to enable a faster and more accurate computation of the induction, especially close to the blade root and tip. The near wake model is used to add a radial coupling between the blade sections and provide a modelling for tip loss effects that is depending on the actual blade geometry and the respective operating point.

Moreover, the coupling of the near wake model with a BEM theory based far wake model is presented. To avoid accounting for the near wake induction twice, the induction from the BEM model is reduced by a coupling factor, which is continuously updated during the computation to ensure a good behavior of the model in varying operating conditions.

The coupled near and far wake model is compared to a simple prescribed wake lifting line model, a BEM model and full rotor CFD to evaluate the steady state results in different cases. The model is shown to deliver good results across the whole operation range of the NREL 5 MW reference wind turbine.

KEYWORDS

blade element momentum, lifting line, near wake model, rotor aerodynamics

Correspondence

Wind Energy Department, Technical University of Denmark, Frederiksborgvej 399, Building 118, DK-4000 Roskilde, Denmark E-mail: gepir@dtu.dk

Received . . .

1. INTRODUCTION

The aerodynamic computations in most aeroelastic wind turbine codes are based on blade element momentum (BEM) theory, where the blade is divided into radial sections and the blade forces are equated with the force applied on the wind. This approach leads to good results if the BEM model is extended by a tip loss correction factor to take into account the finite number of blades [1], a dynamic inflow model to include the inertia of the wake [2] and further extensions to cover for example sheared inflow and yaw error. The main advantage of a BEM model compared to other, more advanced, aerodynamic models, such as vortex codes and CFD [3] is the very fast computation time while obtaining good results in normal operation cases.

This paper further develops a coupled aerodynamics model consisting of a BEM model for the far wake computation and a lifting line based trailed vorticity model, the so-called near wake model developed by Beddoes [4]. This coupled aerodynamics model has been proposed by Madsen and Rasmussen for application on wind turbines [5] and promising results have been obtained by Andersen [6]. The purpose of the near wake model part is to account for both the root and tip vortices, to add an aerodynamic coupling between the radial sections along the blade span and to provide a more accurate modeling of the induction dynamics. The BEM model is necessary to compute the induction from the far wake and the slower dynamic inflow effects.

The near wake model originally assumes the trailed vorticity to stay in the rotor plane, which is a good approximation for operation at high tip speed ratio. Above rated wind speed, the down wind convection speeds of the trailed vorticity are higher, and accordingly the vorticity path is better approximated by helices. Wang and Coton, [7], proposed to include the helix angle in the near wake model, but did not account for the decreasing induction due to the larger distance between trailed vorticity and the blade when the vorticity has convected down wind. This increased distance is mainly important close to the blade root, where the root vortex is trailed at a large helix angle, and is accounted for by the model presented in this paper.

Moreover, a basic assumption of the near wake model, that the induction due to the trailed vorticity approaches zero within a quarter revolution, is not valid for the induction at the blade root due to the tip vortex. A correction is presented that limits the induction in this case to the induction from a quarter revolution to avoid an overestimation of induced velocities.

A disadvantage of previous implementations of the coupled aerodynamics model has been that the coupling factor, which is used to reduce the full BEM induction to account for the part of the induction that is included in the near wake model, had to be calculated before the simulations, [6]. In the present implementation, the coupling factor is adjusted during the computation to match the steady state thrust of a BEM model. This approach ensures that the mean induction results are similar to the well-validated BEM method, while different radial induction distributions due to, for example, trailed vorticity at trailing edge flaps or a partial pitch blade can be modeled. Also the dynamic behavior of the induction due to trailed vorticity is retained in the model.

To evaluate the coupled aerodynamic model, the results are compared with the BEM model implemented in HAWC2 and full rotor CFD results from EllipSys3D [3]. The focus in this paper is on the steady state results, i.e. on the handling of near and far wake by different models, the coupling factor computation and the effectiveness of the root and convection corrections.

The following section will present the near wake model as described by Beddoes [4], improved by Wang and Coton [7], and implemented in a coupled near and far wake model for rotor aerodynamics by Madsen and Rasmussen [5] and Andersen [6]. Section 3 is a brief analytical derivation of the induction from helical vortex arcs, which will be used to correct for the error due to neglecting the downwind convection, to analyze the axial and tangential induction from the near wake of one blade and the induction due to the remaining trailed wake of a three bladed rotor. In Section 4 modifications of the near wake model to improve accuracy and computation speed are presented. Section 5 discusses the implementation in a coupled near and far wake model, where the coupling factor is computed and modified during the simulation. Results are shown in section 6, where the coupled model is compared against numerical integration of the Biot-Savart law, a BEM model and full rotor CFD.

2. ORIGINAL MODEL DESCRIPTION

2.1. Near wake model

The purpose of the near wake model (NWM) is to approximate the induction at a blade due to the vorticity trailed from that blade in a quarter of a rotor revolution. To make an efficient computation possible, Beddoes [4], assumes that the trailed vorticity follows prescribed circular arcs in the rotor plane. Using the Biot-Savart-Law, the induction dw from a vortex element with the length ds on a circular arc trailed at radius r at a point on the blade at a distance h from the vortex trailing point, cf. Figure 1 can be found as:

$$\mathrm{d}w = \frac{\Delta\Gamma\,\mathrm{d}s}{4\pi r^2}\frac{1-\left(1-\frac{h}{r}\right)\cos(\beta)}{\left[1+\left(1-\frac{h}{r}\right)^2-2\left(1-\frac{h}{r}\right)\cos(\beta)\right]^{3/2}}, \tag{1}$$

where $\beta = \Omega t$ is the angle the blade has moved since the element has been trailed. Equation (1) is derived in Section 3 for the more general case including downwind convection. To obtain the induction from a vortex arc, Equation (1) could be

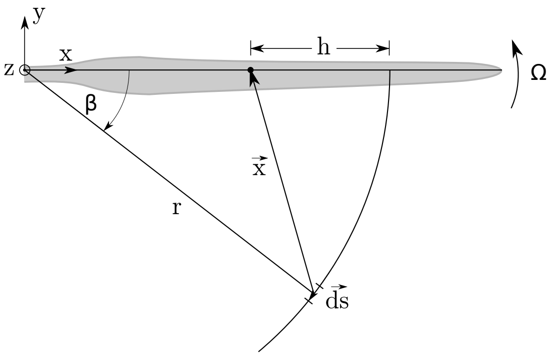

Figure 1. Sketch of the blade geometry with vorticity trailed at radius r. Since the vortex element $\vec{ds}$ has been trailed the blade has moved by an angle β at the angular velocity Ω. The induction is to be computed at a blade section the distance h inboard from the vortex trailing point.

integrated numerically. But it is very expensive to obtain the induction from the trailed wake along the blade in this way: If the blade is discretized into n sections, and $n+1$ vortices are trailed at the root and tip of the blade and in between the sections, $n(n+1)$ integrations of Equation (1) are necessary to obtain the induction due to every trailed vortex arc at every blade section.

A fast trailing wake algorithm has been developed by Beddoes to speed up these integrations. The basic idea is to compute the induction from a vortex element at the lifting line and let that value decrease as the blade rotates away from that element. This decay of the induction can then be efficiently computed using exponential functions. The induction from an element at the lifting line follows directly from Equation (1):

$$\mathrm{d}w_0 = \mathrm{d}w(\beta = 0) = \frac{\Delta\Gamma\,\mathrm{d}s}{4\pi r^2}\frac{1-\left(1-\frac{h}{r}\right)}{\left[1+\left(1-\frac{h}{r}\right)^2-2\left(1-\frac{h}{r}\right)\right]^{3/2}} = \frac{\Delta\Gamma r\,\mathrm{d}\beta}{4\pi h|h|}. \tag{2}$$

The spatial decay function that gives the fraction of the induction from an element of its value at the lifting line is obtained through division of Equation (1) by (2). Beddoes proposed to approximate it using exponential functions:

$$\frac{\mathrm{d}w}{\mathrm{d}w_0} = \frac{\left(\frac{h}{r}\right)^2\left[1-\left(1-\frac{h}{r}\right)\cos(\beta)\right]}{\left[1+\left(1-\frac{h}{r}\right)^2-2\left(1-\frac{h}{r}\right)\cos(\beta)\right]^{3/2}} \approx 1.359e^{-\beta/\Phi} - 0.359e^{-4\beta/\Phi}, \tag{3}$$

where Φ is a geometrical factor depending on r and h. In this paper, an improved definition of Φ by Wang and Coton [7] is used. This definition leads to a reduced error if the vortices are trailed further inboard than the blade section where the induction shall be computed, which is defined as $h/r < 0$.

$$\Phi = \frac{\pi}{4}\left|\left(1+\frac{h}{2r}\right)\ln\left(1-\frac{h}{r}\right)\right| \qquad \text{for } 0 < h/r < 1 \tag{4a}$$

$$\Phi = \frac{1-\frac{h}{r}}{1.5+\ln(1-\frac{h}{2r})} \qquad \text{for } h/r < 0. \tag{4b}$$

In Sections 4.2 and 4.3 Φ is further modified to improve the accuracy of the induction at the inboard part of the blade due to vortices close to the tip, i.e. $h/r \to 1$, and to model the downwind convection of the trailed vorticity.

The trailing wake algorithm proposed by Beddoes determines the near wake induction W at a point on the blade at a given time step i as:

$$W^i = X_w^i + Y_w^i, \tag{5}$$

with the slowly decaying component X_w and the faster decaying component Y_w. The value of these components depends both on their values at the previous time steps, which are decreasing during a time step according to the exponential functions, and the new contributions D_w from the vortex element trailed in the time step:

$$X_w^i = X_w^{i-1}e^{-\Delta\beta/\Phi} + 1.359D_w e^{-\Delta\beta/2\Phi} \tag{6a}$$

$$Y_w^i = Y_w^{i-1}e^{-4\Delta\beta/\Phi} - 0.359D_w e^{-2\Delta\beta/\Phi}. \tag{6b}$$

Assuming a straight element perpendicular to the lifting line and applying the Biot-Savart law, the induction due to the new element trailed during the time step is found as:

$$D_w = \frac{\Delta\Gamma\left(\frac{\Delta s}{|h|}\right)}{4\pi h\left[1+\left(\frac{\Delta s}{h}\right)^2\right]^{1/2}}. \tag{7}$$

Exponential functions evaluated at half a time step are used to determine the fractions of D_w driving the faster and slower decaying parts of the induction in Equations (6). The resulting fractions of D_w are added to the decreased contributions from all previous components included in X_w^{i-1} and Y_w^{i-1}.

To account for the movement of the vortices out of the rotor plane in the presence of downwind convection, Wang and Coton [7] introduced the angle φ of the helix formed by the trailed vortex filaments in the calculation of D_w. Andersen [6] proposed to model the tangential induction in a corresponding way as the axial induction:

$$D_{w,a} = D_w\cos(\varphi), \quad \text{and} \tag{8}$$

$$D_{w,t} = D_w\sin(\varphi). \tag{9}$$

The subscripts a and t denote the axial and tangential induction. The values for the induction from the first element are then inserted in Equations (6) replacing D_w.

2.2. Coupling to far wake model

The near wake model is only accounting for the induction due to the trailed vorticity in the first quarter of a rotation. A model for rotor aerodynamics must therefore include a far wake model and a shed vorticity model to cover the complete induction from the rotor. As in previous implementations [5, 6], a BEM model with reduced thrust is used to model the far wake. The shed vorticity model used in this paper is based on the inviscid part of the Beddoes-Leishman-type model by Hansen et al. [8].

The BEM model used for the far wake includes a dynamic inflow model with two different time constants, as in the aeroelastic code HAWC2 [9, 10, 11]. No tip loss effects are included in the far wake model, because they are taken care of by the near wake model, cf. Section 6.1.3. In this paper only uniform inflow without turbulence is considered, therefore it is unnecessary to compute the induction on a grid to account for e.g. wind shear and independent motion of individual blades, as in HAWC2. Instead the far wake induction is assumed to be constant on each annular element of the rotor.

In the BEM model, first the aerodynamic forces are computed. To account for the part of the thrust included in the near wake model, the thrust coefficient is then reduced by multiplying with a coupling factor k_{FW}:

$$C_{T,FW} = C_T k_{FW}. \tag{10}$$

The induction follows from the thrust coefficient based on the following polynomial function [2], which is used in the HAWC2 BEM model:

$$a(C_{T,FW}) = k_3 C_{T,FW}^3 + k_2 C_{T,FW}^2 + k_1 C_{T,FW} + k_0 \tag{11}$$

In the previous implementations, the coupling factor was provided as an input by the user and had to be calculated in preceding simulations, with a goal to achieve the same mean induction as in a BEM model [6]. A method to determine the coupling factor during the computation is described in Section 5, so that no additional input for the near wake model is needed and the rotor thrust matches the one obtained from a BEM model in steady computations.

3. INDUCTION FROM HELICAL VORTEX ARCS

In this section, the basic NWM equations are derived for axial and tangential induction including out of plane movement of the vortex filaments with a constant downwind convection velocity. The goal is to obtain a basis for evaluating the induction computed by the near wake model and for developing a convection correction in Section 4.3. A constant downwind convection velocity v_h results in helical instead of circular vortex arcs. The helix angle φ, with $\tan\varphi = v_h/(\Omega r)$ depends on the radial position of the vortex trailing point. The following derivations are based on the geometry sketched in Figure 1. The vortex is trailed at a blade radius r, the induction is to be calculated at a blade section at the distance h from the origin of the vortex. The vector $\vec{x}$ points from the location of the trailed vortex filament to the blade section, and the filament $\vec{ds}$ is pointing away from the blade. The x-axis points from blade root to blade tip, the y-axis in front of the blade, away from the trailed vorticity and the z-axis is positive upwind.

The vector $\vec{x}$ from the vortex filament at the angle β to the blade section and the vortex filament with the length ds are found as:

$$\vec{x} = \begin{pmatrix} -r\cos\beta + r - h \\ r\sin\beta \\ v_h\beta/\Omega \end{pmatrix}, \quad \vec{ds} = \frac{ds}{\sqrt{1 + \left(\frac{v_h}{\Omega r}\right)^2}} \begin{pmatrix} -\sin\beta \\ -\cos\beta \\ -v_h/(\Omega r) \end{pmatrix} \tag{12}$$

The Biot-Savart-law gives for the induction due to this filament at the blade section:

$$dw = \frac{\Gamma}{4\pi} \frac{\vec{x} \times \vec{ds}}{|\vec{x}|^3}. \tag{13}$$

The z-component, the axial induction, is evaluated as:

$$\begin{aligned} dw_z &= \frac{\Gamma}{4\pi} \frac{x_x ds_y - x_y ds_x}{|\vec{x}|^3} \\ &= \frac{\Gamma ds\cos\varphi}{4\pi r^2} \frac{1 - \left(1 - \frac{h}{r}\right)\cos\beta}{\left(1 + \left(1 - \frac{h}{r}\right)^2 - 2\left(1 - \frac{h}{r}\right)\cos\beta + \left(\frac{v_h\beta}{\Omega r}\right)^2\right)^{3/2}} \end{aligned} \tag{14}$$

where φ is the helix angle:

$$\cos\varphi = \frac{\Omega r}{\sqrt{(\Omega r)^2 + v_h^2}} = \frac{1}{\sqrt{1 + \left(\frac{v_h}{\Omega r}\right)^2}} \tag{15}$$

The axial induction from a filament with a finite length at the blade, i.e. $\beta = 0$, can be found as:

$$\mathrm{d}w_{0,z} = \frac{\Delta\Gamma\,\mathrm{d}s\cos\varphi}{4\pi h|h|}. \tag{16}$$

This leads to the following equation for axial induction, which includes downwind convection:

$$\frac{dw_z}{dw_{0,z}} = \frac{\left(\frac{h}{r}\right)^2\left[1 - \left(1 - \frac{h}{r}\right)\cos\beta\right]}{\left(1 + \left(1 - \frac{h}{r}\right)^2 - 2\left(1 - \frac{h}{r}\right)\cos\beta + \left(\frac{v_h\beta}{\Omega r}\right)^2\right)^{3/2}}, \tag{17}$$

Equations (14) and (16) are obtained for vortices that convect downwind with a constant speed depending on the wind speed at the rotor plane. These equations contain two terms that are additions to the equations without convection, $\cos\varphi$ and $((v_h\beta)/(\Omega r))^2$. The only difference between Equation (17) and Equation (3) is the term $((v_h\beta)/(\Omega r))^2$, which describes the increasing distance from vortex trailing point to calculation point because of the downwind convection.

The equation for the induced velocity in the rotor plane perpendicular to the blade can be derived analogue to the axial velocity. It is the y-component of Equation (13). The induction from the first element is the $\sin\varphi$ counterpart of Equation (16). That leads to the spatial decay function for tangential induction:

$$\frac{dw_y}{dw_{0,y}} = \frac{\left(\frac{h}{r}\right)^2\left(1 - \frac{h}{r} - \cos\beta - \beta\sin\beta\right)}{\left(1 + \left(1 - \frac{h}{r}\right)^2 - 2\left(1 - \frac{h}{r}\right)\cos\beta + \left(\frac{v_h\beta}{\Omega r}\right)^2\right)^{3/2}}. \tag{18}$$

The inductions computed using Equations (17) and (18) differ for not small β and h/r. This is because the angle of the in-plane induction, and therefore the fraction of the induction that is perpendicular to the blade and contributes to the velocity triangle, changes as β increases. There is also an in-plane component of the induction due to the vorticity parallel to the rotor plane that increases as the vorticity convects downstream. Thus using the same approximation, Equation (3) for tangential induction as for axial induction, as proposed by Andersen, [6] , introduces an error. This error is quantified in Section 4.3.

What becomes obvious is that the helix angle is only introduced through the normalizing of $\vec{ds}$ in Equation (12). This means that if the projection of the filament in the rotor plane is used for the computation of $\Delta\beta = \Omega\Delta t$, as proposed by Beddoes, the helix angle is not necessary for the computation of the axial induction. The wake rotation, represented by tangential induction, can be included, defining $\Delta\beta = (v_y/r)\Delta t$, where v_y denotes the in-plane component of the relative velocity.

Assuming a constant downwind convection velocity and no wake expansion, Equations (16) to (18) can be used as a basis for computation of the induction due to the trailed wake of a three bladed rotor. To model blades at different positions, an angle β_{start} is added, which is 0 for the blade where the induction shall be calculated, 120° for the blade behind in the direction of rotation and -120° for the blade in front. The axial induction from a quarter rotation at the blade is then given as:

$$W = \sum_{i=1}^{3} W_i, \quad \text{where} \tag{19}$$

$$W_i = \frac{\mathrm{d}w_0}{\mathrm{d}\beta}\int_{\beta_{start,i}}^{\pi/2+\beta_{start,i}} \frac{dw}{dw_0}\,d\beta. \tag{20}$$

To obtain the induction due to the wake trailed from the other blades, the z-component of $\vec{x}$, Equation (12), has to be modified so that the trailed vorticity starts in the rotor plane for $\beta = \beta_{start}$, resulting in $x_z = v_h(\beta - \beta_{start})/\Omega$. Thus follows for the axial and tangential induction

$$\frac{dw_z}{dw_{0,z}} = \frac{\left(\frac{h}{r}\right)^2 \left[1 - \left(1 - \frac{h}{r}\right)\cos\beta\right]}{\left(1 + \left(1 - \frac{h}{r}\right)^2 - 2\left(1 - \frac{h}{r}\right)\cos\beta + \left(\frac{v_h(\beta - \beta_{start})}{\Omega r}\right)^2\right)^{3/2}}, \tag{21}$$

$$\frac{dw_y}{dw_{0,y}} = \frac{\left(\frac{h}{r}\right)^2 \left(1 - \frac{h}{r} - \cos\beta - (\beta - \beta_{start})\sin\beta\right)}{\left(1 + \left(1 - \frac{h}{r}\right)^2 - 2\left(1 - \frac{h}{r}\right)\cos\beta + \left(\frac{v_h(\beta - \beta_{start})}{\Omega r}\right)^2\right)^{3/2}}. \tag{22}$$

This formulation can be used to compute the far wake as well, by integrating Equation (20) from $\pi/2 + \beta_{start,i}$ to infinity or, in practise, a sufficiently high number of rotations, for example 32π.
Further, the Equations above can be used to calculate the induction from a steady trailed wake without wake expansion and a constant convection speed for a blade discretized in calculation points and vortex trailing points. It can serve as a reference to compare the NWM to and to evaluate the division of the wake into a near wake and a far wake based on BEM computations. The input, namely axial and tangential induction and vortex strength, can be obtained by using the coupled near and far wake model. In order to get a reasonable result from the helical vortex model for the far wake, the downstream convection velocity is limited to a minimum of $2/3v_\infty$. This limit on the convection can be justified because especially close to the tip of the blade the induction is a function of the azimuth angle, with a much higher induction at a blade than in between blades. Thus having the tip vortex convect with $v_h = v_\infty - v_{ax,tip}$ would lead to an overestimated far wake induction, because the tip vortex stays close to the rotor plane for many revolutions. The minimum convection speed is relevant at wind speeds below rated.

4. NEAR WAKE MODEL MODIFICATIONS

4.1. Modified trailing functions

The original approach of first calculating the induction D_w from a finite length element and a subsequent splitting in two components, Equation (6), has a major disadvantage. For time steps of 0.01 or $0.02s$ and cosine based spatial discretization of 30 to 60 points, which are widely used in aeroelastic wind turbine codes, cf [12], the induction from the newest element can be drastically underestimated close to the root and the tip of the blade. The reason for this is in the splitting of D_w into X_w and Y_w using exponential functions evaluated at half a time step, cf. Equation (6). Starting point for the development of an improved approach is Equation (2). Division by $\mathrm{d}\beta$ leads to:

$$\frac{\mathrm{d}w_0}{\mathrm{d}\beta} = \Delta\Gamma \frac{r}{4\pi h|h|}. \tag{23}$$

The induction from the newest element, which in the original model is assumed to be a straight element, cf. Equation 7, can instead be computed as:

$$\begin{aligned} D_w &= \frac{\mathrm{d}w_0}{\mathrm{d}\beta}\Delta\beta \left\langle \frac{\mathrm{d}w}{\mathrm{d}w_0} \right\rangle \\ &= \Delta\Gamma \frac{r}{4\pi h|h|} \int_0^{\Delta\beta} \frac{\mathrm{d}w}{\mathrm{d}w_0}\, d\beta. \end{aligned} \tag{24}$$

Here a constant induction along the element $(\mathrm{d}w_0/\,\mathrm{d}\beta)\Delta\beta$ is corrected by multiplying with the decay function $\mathrm{d}w/\,\mathrm{d}w_0$ averaged over the length of the element. Inserting Equation (3) yields:

$$\begin{aligned} D_w &= \Delta\Gamma \frac{r}{4\pi h|h|} \int_0^{\Delta\beta} (1.359 e^{-\beta/\Phi} - 0.359 e^{-4\beta/\Phi})\, d\beta \\ &= \Delta\Gamma \frac{r}{4\pi h|h|} \Phi[1.359(1 - e^{-\Delta\beta/\Phi}) - \frac{0.359}{4}(1 - e^{-4\Delta\beta/\Phi})] \\ &\equiv \Delta\Gamma \left[D_X (1 - e^{-\Delta\beta/\Phi}) + D_Y (1 - e^{-4\Delta\beta/\Phi}) \right]. \end{aligned} \tag{25}$$

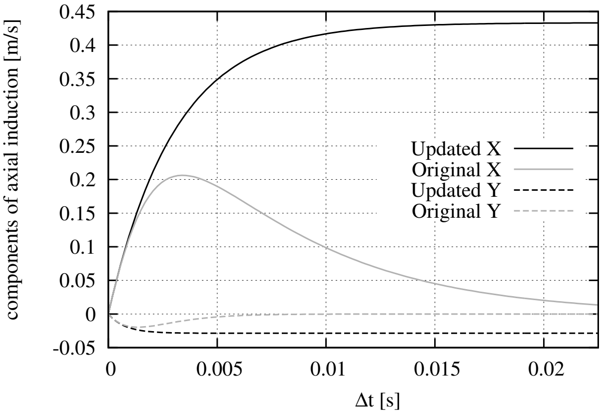

Figure 2. Comparison of the induction from the newest element, divided in the X and Y components depending on the chosen time step. The vortex with $\Delta\Gamma = 1$ is trailed from r=60 m, the blade rotates with 12.1 rpm and the calculation point is placed at r=59.4 m, so $h/r = 0.01$.

Now the induction of the first element is divided into slow and fast decaying components, which can be directly inserted into Equation (6):

$$W_i = X_w^i + Y_w^i \tag{26a}$$

$$X_w^i = X_w^{i-1} e^{-\Delta\beta/\Phi} + D_X \Delta\Gamma (1 - e^{-\Delta\beta/\Phi}) \tag{26b}$$

$$Y_w^i = Y_w^{i-1} e^{-4\Delta\beta/\Phi} + D_Y \Delta\Gamma (1 - e^{-4\Delta\beta/\Phi}). \tag{26c}$$

In this formulation, the error in evaluating the trailing functions does not depend on the time step and the spatial point density, since D_w is split into an X_w and Y_w component according to Beddoes' exponential approximation, Equation (3), and the assumption of a straight element is not necessary.

A comparison of the original way to calculate the induction from the newest element and the proposed modification is shown in Figure 2. The X and Y components associated with D_w from Equations (6) and (26) are plotted depending on the time step for an example case with $h/r = 0.01$. The plot shows that the original evaluation is deviating from the new formulation already at small time steps. This error would have to be reduced by using smaller time steps or sub time steps for the near wake model, both options slowing down the computations.

Another advantage is that D_X and D_Y only depend on the point distribution, which is constant during a simulation, and not on Δs, like the original D_w, cf. Equation (7). Therefore D_X and D_Y can be computed in the initialization of the program, which, in combination with the halved number of evaluations of exponential functions in Equation (26) compared to Equation (6), greatly improves the computational speed.

4.2. Root correction

For small, positive values of h/r, which means the vortex trailing point and the calculation point are close with the trailing point further outboard, both the analytical spatial decay function and Beddoes' approximation, Equation (3), reach small values within the first 90 degrees, cf. Figure 3. If the calculation point moves further inboard, that means h/r gets closer to one, the function values decrease slower, as seen in the right plot. They do not approach zero within 90 degrees, even for higher convection speeds. Thus the near wake model, integrating Beddoes' functions to infinity, gives a higher induction than the value of a quarter circle.

The goal of the correction here is to limit the steady state induction the NWM gives to that of a quarter circle and to reduce the dynamic effects afterwards.

Inserting $\Delta\beta = \pi/2$ in Equation (25) leads to the induction from a quarter circle of trailed vorticity with constant circulation according to Beddoes' functions:

$$D_{w,\pi/2} = \Delta\Gamma \left[D_X (1 - e^{-\pi/(2\Phi)}) + D_Y (1 - e^{-2\pi/\Phi}) \right]. \tag{27}$$

If the near wake model is applied, the following induction is reached because of the integration to infinity:

$$D_{w,\infty} = \Delta\Gamma (D_X + D_Y) \tag{28}$$

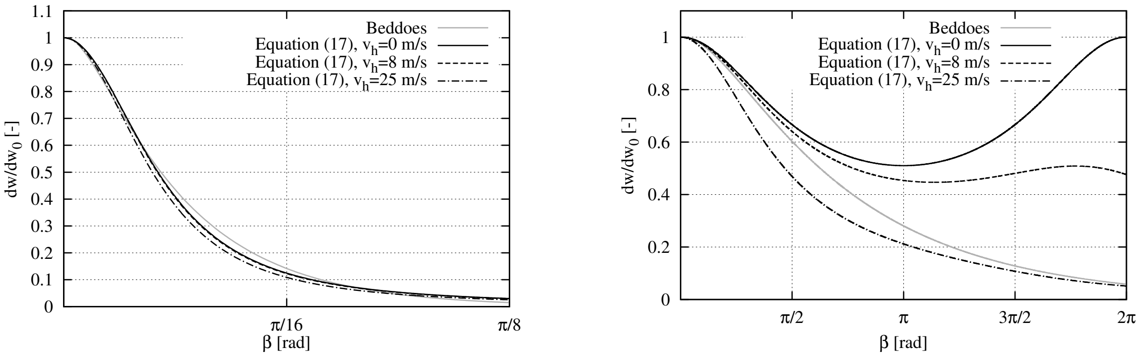

Figure 3. Comparison of the analytical trailing function, Equation (17), and Beddoes' approximation, Equation (3) for $h/r = 0.1$ (left) and $h/r = 0.8$ (right). Zero is clearly not reached within a quarter rotation at large h/r, even at high hub wind speeds.

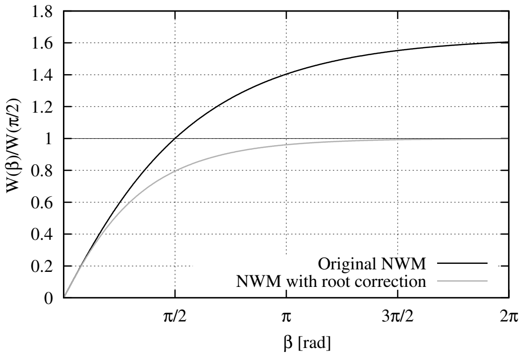

Figure 4. Induction due to constant trailed vorticity of length β as fraction of the induction due to a quarter circle at $h/r = 0.8$. The black curve shows the behavior of the original near wake model. Applying the correction factor on the value leads to the response shown in the gray curve.

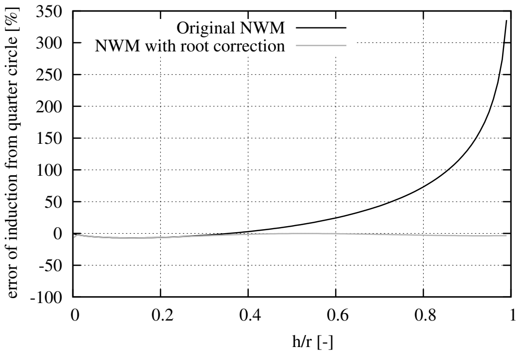

Figure 5. Integral error of original and corrected NWM trailing functions compared to analytical solution. The error for negative h/r has been reduced by using the Φ according to Wang and Coton, the error for positive h/r is reduced due to the new root correction.

The correction factor is then found as:

$$C = \frac{D_{w,\pi/2}}{D_{w,\infty}} = \frac{D_X(1 - e^{-\pi/(2\Phi)}) + D_Y(1 - e^{-2\pi/\Phi})}{D_X + D_Y}. \tag{29}$$

(30)

The root correction factor is applied in the near wake model by correcting Φ, which leads to corrected D_X and D_Y in the initialization of the program:

$$\Phi_C = \Phi C, \quad D_{X,C} = 1.359 \frac{r}{4\pi h|h|} \Phi_C, \quad D_{Y,C} = -\frac{0.359}{4} \frac{r}{4\pi h|h|} \Phi_C, \tag{31}$$

It is shown in Figure 4 how this approach limits the induction to the value reached after a quarter rotation.

The steady induction given by the integral of the exponential functions to infinity is compared with the integral of the analytical solution over a quarter circle in Figure 5. The root correction roughly reduces the error of the blade root induction due to the tip vortex, ($h/r \to 1$) from over 300% to 5%.

4.3. Correction for downwind convection

The influence of the downwind convection of the vortices can be included in the near wake model with the helix angle as additional parameter. This additional parameter is here included in the decay rate Φ, which is then not only a function of h/r, cf. Equation (4), but also a function of the tangent of the helix angle φ.

Wang and Coton, [7], proposed to obtain an optimal value for Φ by integration of both sides of equation (3) and numerically determining the value of Φ for which the integral of the approximation equals the integral of the Biot-Savart law. The same approach is used in this work to determine optimal values of Φ in the presence of downwind convection, where the exact solution of the induction decay is given by Equation (17). The optimal Φ for computing the axial induction solves the following Equation:

$$\int_0^{pi/2} \left(\frac{\left(\frac{h}{r}\right)^2 \left[1 - \left(1 - \frac{h}{r}\right)\cos\beta\right]}{\left(1 + \left(1 - \frac{h}{r}\right)^2 - 2\left(1 - \frac{h}{r}\right)\cos\beta + \left(\frac{v_h \beta}{\Omega r}\right)^2\right)^{3/2}} \right) \mathrm{d}\beta = \int_0^{pi/2} \left(1.359 e^{-\beta/\Phi_{opt,z}} - 0.359 e^{-4\beta/\Phi_{opt,z}}\right) \mathrm{d}\beta. \tag{32}$$

For the tangential induction computation, the optimal Φ follows accordingly from Equation (18).

The correction for downwind convection is developed as an additional factor that the Φ according to Wang and Coton, Equation (4), is multiplied with:

$$\Phi^* = \Phi \frac{\Phi_{opt,z}(\tan\varphi \neq 0)}{\Phi_{opt,z}(\tan\varphi = 0)} \approx \Phi f(h/r, \tan\varphi). \tag{33}$$

The correction function f is an exponential function approximation that has been obtained through curve fitting:

$$f = (1.1 e^{-b_1(h/r)\tan\varphi} + a_2(h/r) e^{-b_2(h/r)\tan\varphi} - 0.1 - a_2(h/r)). \tag{34}$$

The dependency of the parameters b_1, a_2, b_2 on h/r has been as well approximated by exponential functions:

$$b_1 = a_{1,1} + a_{1,2} e^{a_{1,3} h/r} + a_{1,4} e^{a_{1,5} h/r}, \tag{35a}$$

$$b_2 = a_{2,1} + a_{2,2} e^{a_{2,3} h/r} + a_{2,4} e^{a_{2,5} h/r}, \tag{35b}$$

$$a_2 = a_{3,1} + a_{3,2} e^{a_{3,3} h/r} + a_{3,4} e^{a_{3,5} h/r}. \tag{35c}$$

The parameters $a_{i,j}$ are collected in a matrix $\mathbf{A}$:

$$\mathbf{A} = \begin{pmatrix} 1.9223 & -1.2524 & -0.8313 & 0.0055 & 6.1569 \\ 14.0826 & -11.0331 & -0.3656 & 0.0034 & 8.8199 \\ -0.2441 & -0.0639 & 2.8980 & 0.0441 & 3.3352 \end{pmatrix} \quad \text{for } 0 < h/r < 1 \tag{36a}$$

$$\mathbf{A} = \begin{pmatrix} 0.0748 & 0.3217 & 0.2720 & 0.2596 & 2.5328 \\ 0.2464 & 1.3197 & 2.5445 & 1.2137 & 0.3018 \\ 1.1736 & 0.0529 & 1.4179 & -1.5000 & -0.0018 \end{pmatrix} \quad \text{for } h/r < 0. \tag{36b}$$

The approximation function f is compared against the numerically obtained values of $\Phi_{opt}(\tan\varphi \neq 0)/\Phi_{opt}(\tan\varphi = 0)$ in Figure 6. The purpose of f is to improve the accuracy of the axial induction computation when downwind convection is present, and this is clearly achieved. Also the optimal Φ for tangential induction is matched well for $|h/r| << 1$. For $h/r \to 1$ and low downwind convection speeds, the analytical expression for $dw_y/dw_{0,y} \geq 1$ for angles $\beta < \pi/2$, so an approximation using Beddoes' approach is not possible.

In principle, an optimal Φ for the tangential induction would be necessary for accurate results. This would, however, increase the computation time in a way that is not reflected by the benefits of the increased accuracy considering the small importance of a precise tangential induction computation. Therefore it is recommended to use the same approximation for Φ as for the axial induction.

5. DETERMINING OF THE COUPLING FACTOR

Because different operating conditions change the ratio of induction from the near and far wake, the coupling factor is not constant. An example for this is the operation of a turbine above rated wind speed. If the wind speed increases, the helical pitch angle increases. This has a bigger influence on the induction from the far wake than from the near wake, therefore the coupling factor decreases.

Andersen [6] has proposed to compute the coupling factor beforehand for a turbine, depending on tip speed ratio and thrust coefficient, but in paper work a different approach is suggested to avoid these preliminary computations:
In each time step, in addition to compute the axial far wake induction with reduced thrust coefficient, a second reference BEM induction with complete thrust coefficient and tip loss correction are computed. This reference BEM induction a_{ref}

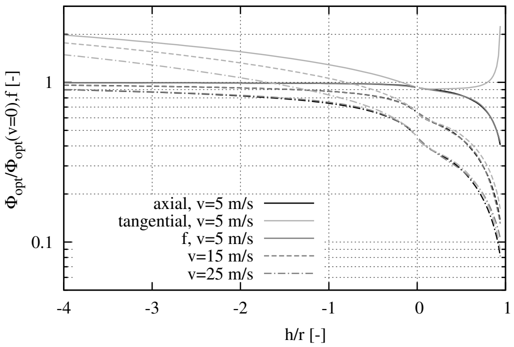

Figure 6. Comparison of the exact axial and tangential $\Phi/\Phi(v=0)$ with the approximation function f to the axial induction, cf. Equation (33). Results are shown for different convection speeds. Vortices are trailed at $r = 10m$, the rotation speed is $\Omega = 12.1rpm$. The functions are not evaluated at h/r=0 and h/r=1, where the optimal Φ without convection tends to zero and infinity, respectively.

is the induction following from Equation (11) without application of a coupling factor but using the Wilson and Lissaman tip loss correction [1]. The objective is to chose a coupling factor so that

$$a_{ref,QS} = a_{FW,QS} + a_{NW}, \tag{37}$$

where quasi steady values of the far wake and reference induction are used to reduce slow changes of the coupling factor due to the different dynamic behavior of the BEM model and the coupled model. The near wake induction reacts faster than the far wake induction and thus the dynamic near wake induction is used for the computation of the coupling factor.

A new value for the coupling factor k_{FW} can be determined every time step for each blade section with the goal of fulfilling Equation (37) as:

$$k^{i+1}_{FW,j} = k^{i}_{FW,j} + \frac{a_{ref,QS,j} - (a_{FW,QS,j} + a_{NW,j})}{\partial a/\partial k_{FW}}, \quad \text{with} \tag{38}$$

$$\partial a/\partial k_{FW} = 3k_3 C_T^3 k_{FW}^2 + 2k_2 C_T^2 k_{FW} + k_1 C_T, \tag{39}$$

where the subscript j indicates the blade section. A time lag with the same time constant as the near wake part of the dynamic inflow model used in HAWC2 is applied on the coupling factors to avoid introducing numerical instabilities. If these sectional coupling factors were used in the coupled model, the induction along the blade would reach the same distribution as with the BEM model with tip loss correction. Since one purpose of using the coupled model is to achieve an induction distribution due to the whole trailed vortex system including the tip vortex, an average coupling factor is used for the entire blade. In order to closely match the complete thrust of a BEM computation, the coupling factors are averaged weighted by the sectional thrust forces:

$$k_{FW} = \frac{\sum_{j=1}^{n}(k_{FW,j} T_j)}{\sum_{j=1}^{n} T_j} \tag{40}$$

Further before averaging a maximum for the sectional coupling factor of 1.0 and a minimum of 0.5 has been implemented, to limit the influence of sections close to strong trailed vorticity on the whole blade.

With the approach presented here preliminary runs to determine the coupling factor can be avoided. The necessary additional computation time is very small, since the reference induction value is not subject to dynamic inflow or shed vorticity effects and is not used to calculate any aerodynamic forces or the velocity triangle.

6. RESULTS

In the following Section 6.1, the NWM is first compared with the induction following directly from the Biot-Savart law for the NREL 5 MW reference turbine, [13] to evaluate the improvement due to the modifications of the NWM. Cases with wind speeds above and below rated are investigated.

In Section 6.2 the effect of the modification of the trailing functions to remove the time step dependency of the steady induction is illustrated for an exemplary normal production case.

Finally in Section 6.3 the coupled model is validated against a BEM model and full rotor CFD results from EllipSys3D [3] in steady cases.

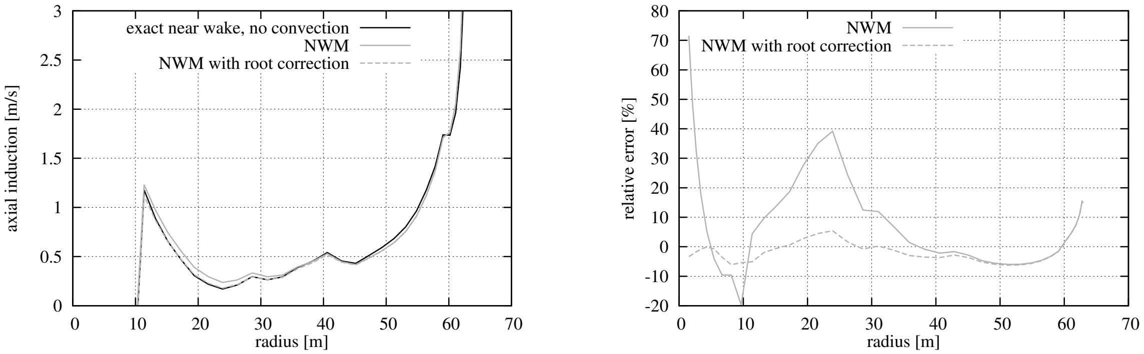

Figure 7. Effect of the root correction on the Induction from the near wake for normal operation at 8 m/s Near wake induction (left) and relative error (right).

6.1. Comparison of near wake model with induction from Biot-Savart law

The accuracy of the approximation of the induction from the near wake, Equation (17), by the modified NWM is investigated in steady cases in this section. Moreover, the induction according to helical vortices trailed from a three bladed turbine, Equations (20) to (21), is compared with results from the coupled model to evaluate the separation of the wake into a lifting line type near wake and a BEM based far wake.

6.1.1. Root correction

The root correction is demonstrated for the NREL turbine in a normal operation case with $\Omega = 9.2$ rpm, uniform inflow with $v_\infty = 8$ m/s and unpitched blades in Figure 7. The results have been obtained in the following way: the axial and tangential induction, as well as the vortex strengths, at sections distributed over the blade from a run of the coupled model with all modifications presented in this paper has been used as input for a numerical integration of Equation (17) over a quarter rotation. The result from this integration is then compared to the near wake induction using either the integral of Beddoes functions from zero to infinity, which is equivalent to $D_X + D_Y$ or the corresponding integral of the functions corrected for the root error, $D_{X,C} + D_{Y,C}$, cf. Section 4.2.

The improvement clearly appears in Figure 7, where the results according due to the Biot Savart law are closer to the results from the NWM with root correction up to a blade radius of 35 meters.

6.1.2. Convection correction

The effect of the convection correction is investigated for two cases above rated wind speed, again based on the NREL 5 MW turbine. In these cases, the uniform wind speeds are $v_\infty = 15$ m/s and $v_\infty = 25$ m/s, the turbine is rotating with its rated speed of $\Omega = 12.1$ rpm and the blade pitch is $10.54°$ and $23.195°$, respectively. The induction and vortex strength from the coupled model is this time used as input for the numerical integration of the induction from circular arcs and helical arcs, Equations (3) and (17). The inductions from these integrations are then compared with the near wake induction from the NWM, without and with the correction for downwind convection of the vortices.

As shown in Figure 8, the convection correction can account for the helix angle, which is most dominant close to the root of the blade.

6.1.3. Separation in near wake and far wake model

The purpose of this section is to evaluate how well the induction from near and far wake can be divided into a near wake model and a BEM based far wake model. To investigate this issue, results from the coupled model are compared with the numerical integration of the induction from prescribed helical vortices trailed from a three bladed rotor, based on Equations (20) to (22).

The induction from these helical vortices can be divided into near wake induction of the blade concerned, where the vorticity is trailed from the rotor plane for $\beta = \beta_{start} = 0$, and the far wake, which includes the complete induction from the wakes of the other two blades and the far wake induction due to the wake of the blade concerned.

Even though the prescribed wake model with helical vortex paths is limited by the assumption of a constant convection speed and the neglection of wake expansion, the qualitative differences between the near and far wake can be investigated in the results.

In Figure 9 the axial and tangential induction from integration of Equation (21) is compared with results from the coupled model for wind speeds of 8 and 25 m/s and the corresponding rotational speeds and pitch angles as used in

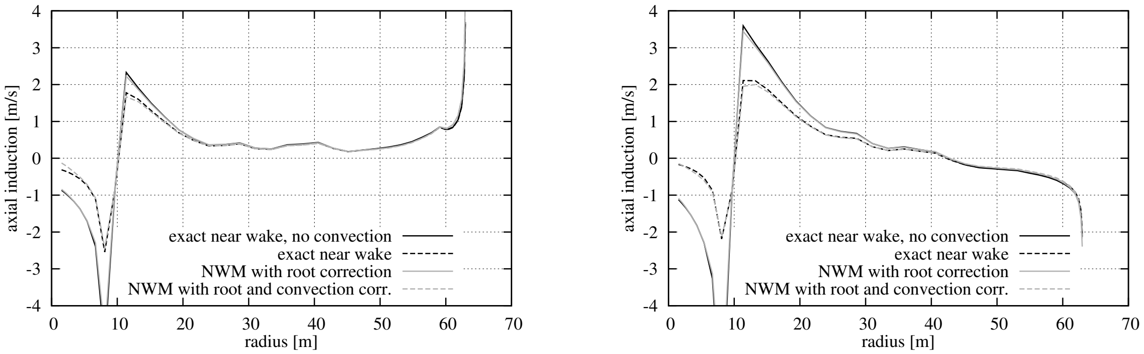

Figure 8. Steady near wake induction at 15 m/s (left) and 25m/s (right), NREL 5 MW reference turbine. The correction of the downwind convection improves the result significantly.

previous sections. Overall the agreement of the near wake induction is better for the axial induction and lower wind speeds. The discrepancy in the tangential near wake induction at 8 m/s close to the tip is partly due to the minimum downwind convection in the helical vortex model that is not present in the coupled model.

The far wake induction is the result of two completely different models: a BEM model with reduced thrust coefficient and the prescribed wake vortex model with constant helical pitch and no wake expansion presented in Section 3. Even though the mean value of the far wake induction in the 8 m/s case is strongly depending on the limit of the downwind convection to a minimum of $2/3v_\infty$, the shape of the far wake induction can be used for qualitative comparison.
Since the NWM can not model the influence of the near wake from the two other blades, the far wake part of the coupled model has to account for both the far wake from all blades and the near wake from the other blades. The tangential induction predicted by the far wake part of the coupled model agrees remarkably well with the far wake and near wake of the other blades from the integration of the helical vortices, except an over prediction of induction close to the root. This over prediction is visible in all cases, except the axial induction in the 8 m/s case. But also in that case a comparison of the shape of the far wake induction shows too much induction at root and tip of the blade compared to the mid blade sections.

6.2. Modified trailing functions

The modified trailing functions proposed in Section 4.1 make the steady induction from the NWM time step independent. This is illustrated in Figure 10, where the steady axial induction of the NREL 5 MW turbine at 8 m/s is shown for different time steps computed with the original trailing functions aside the induction predicted by the modified trailing functions. The result of the original model clearly converges to the result of the modified model if the time step is reduced. For commonly used time steps mainly the induction at the outer part of the blade deviates from the time step independent result, but through the coupling factor, cf. Section 5 the whole blade is affected by a change in induction close to the tip. Note that the modification of the functions not only removes the need for a fine time step to achieve a good steady induction, but also reduces the computation time per time step compared to the original model, as shown in Section 4.1.

6.3. Comparison of the coupled model with a BEM model and CFD

6.3.1. Steady power and thrust

The thrust and power in steady operation of the NREL 5 MW reference turbine of the coupled model and a BEM model are compared for different wind speeds of 4 to 25 m/s in Figure 11, along with the coupling factor computed for the different cases. The power and thrust agree with deviations smaller than 1.5 % and 2.5 %, respectively. The coupling factor stays almost constant where the tip speed ratio and the helical pitch angle are fixed, and then gets reduced at higher wind speeds. This can be explained by the faster convection of the wake away from the turbine at higher speeds and the corresponding bigger fraction of the induction due to the near wake.

6.3.2. Radial load distribution

The radial in-plane and out-of-plane load distributions along the NREL 5 MW blade are shown in Figure 12 for normal operation at wind speeds of 8 and 25 m/s. The HAWC2 BEM model is compared with the coupled near and far wake model and full rotor CFD. The CFD results have been computed with the incompressible RANS solver EllipSys3D [3] assuming fully turbulent flow and using the K-omega SST turbulence model by Menter to close the RANS equations. The

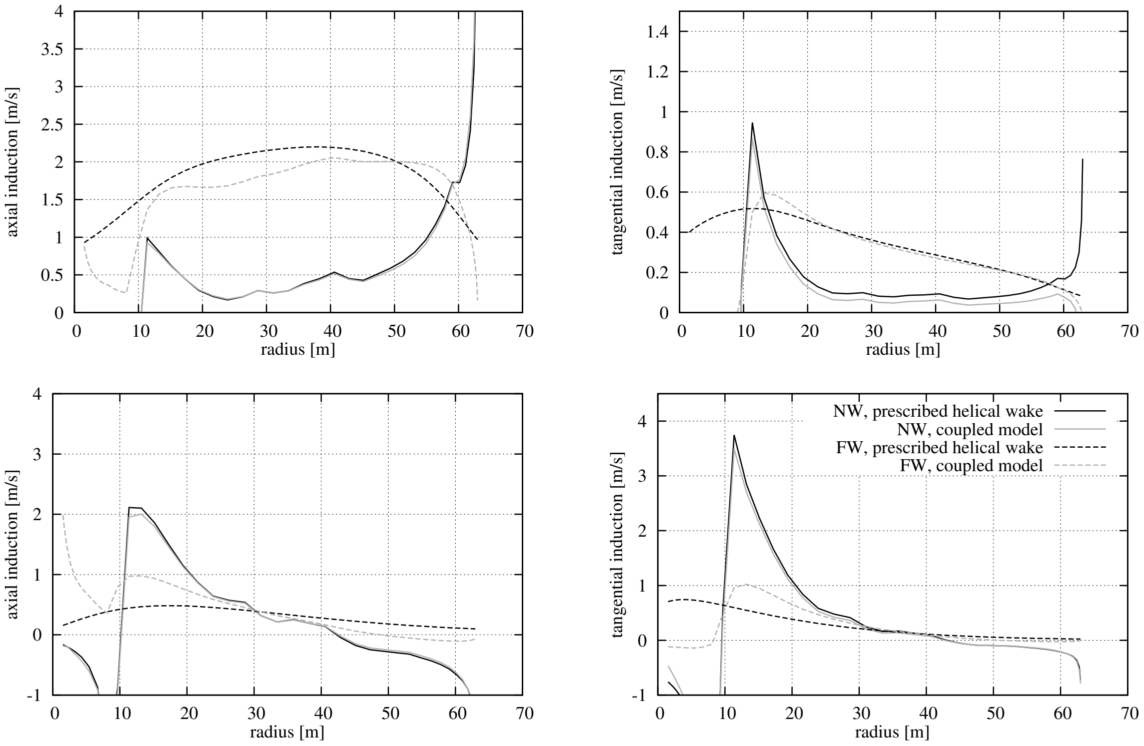

Figure 9. Near wake and far wake from three blades compared to Beddoes' NWM with root and convection correction. Axial induction is shown on the left, tangential induction on the right side. The turbine operates at 8 m/s (top) and 25 m/s (bottom).

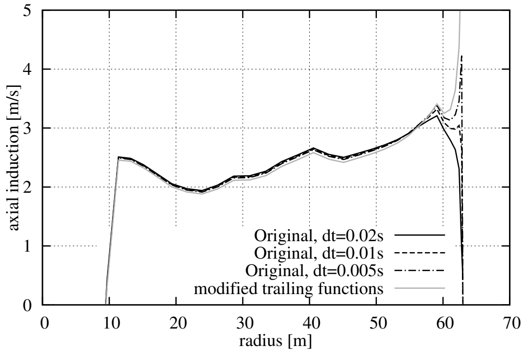

Figure 10. Results from the coupled model at 8 m/s. The effect of the tip vortex varies with time step in the original model and converges to the time step independent results of the modified model presented in Section 4.1.

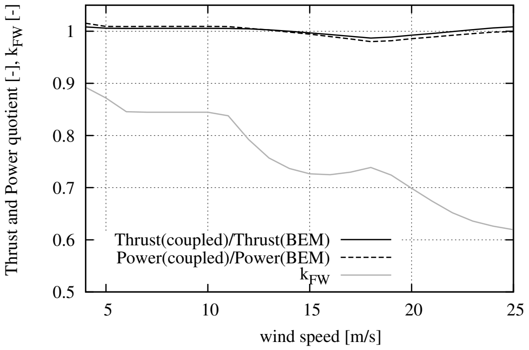

Figure 11. Agreement of power and thrust of coupled model with BEM model and the coupling factors automatically chosen for different wind speeds. The aerodynamic power of the NREL 5 MW rotor agrees within 2.5%, the thrust within 1.5%.

computations are done on a structured grid in which each blade exhibits 256 cells in the chord wise, 128 cells in the span wise and 128 cells in the normal direction. This results in approximately 14 million mesh cells for the entire rotor mesh.

At 8 m/s, the thrust force agrees very well between all the aerodynamic models. There are some differences between the faster models and CFD close to the root and tip of the blade, which can be explained by differences between the lift coefficients from the airfoil polars and the corresponding forces obtained in the 3D CFD computation. The differences seem to be largest for the thick DU airfoils used up to 19.95 m blade radius and the NACA64 airfoil with 17 % thickness used on the outboard part of the blade.

The tangential forces are in close agreement between the models, with the coupled model over predicting the tangential forces on mid blade. Close to the root and tip of the blade, the coupled models results are closer to CFD than the BEM results.

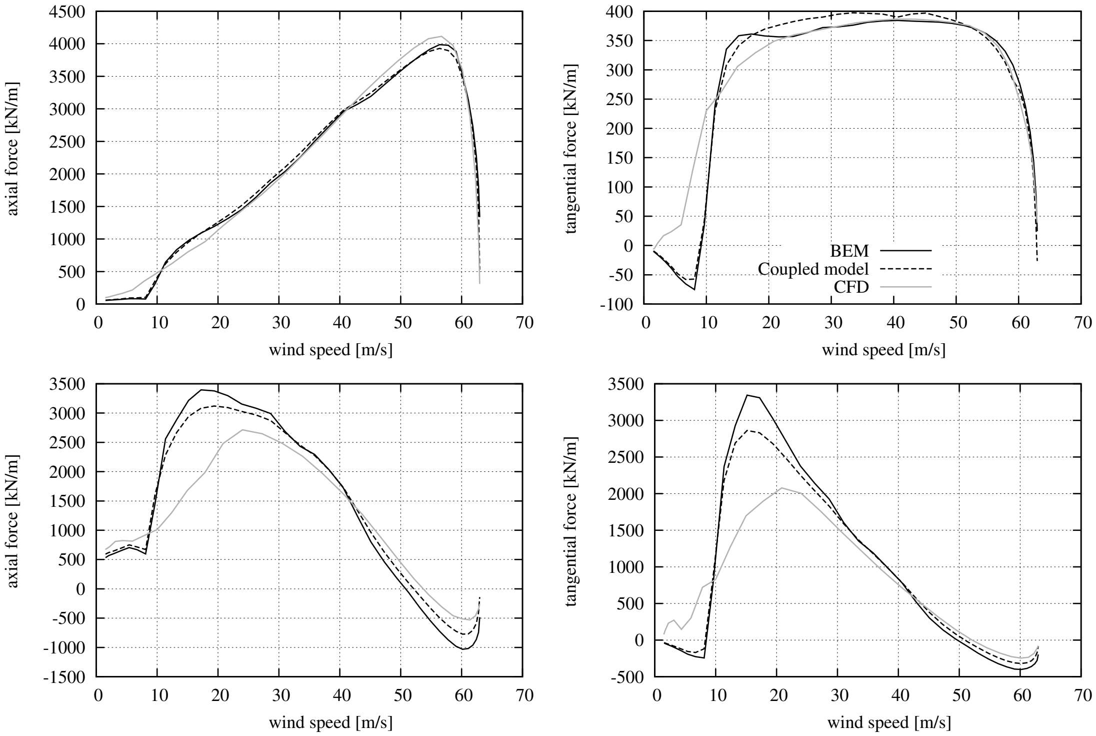

Figure 12. Comparison of axial and tangential forces in normal operation at 8 m/s (top) and 25 m/s (bottom) of a BEM model, the coupled near and far wake model and full rotor CFD.

The forces from the CFD computations deviate strongly at 25 m/ wind speed for airfoils with more than 30 % thickness up to a blade radius of 25 m, which is in agreement with the steady state results at high wind speeds for flexible blades presented by Heinz [14]. The results from the coupled model clearly show the effect of the strong root vortex that is present in this case, and the loads are in between the BEM and CFD results.

7. CONCLUSIONS

A coupled near and far wake model for wind turbine aerodynamics has been presented.

The near wake model, based on a fast prescribed wake lifting line model by Beddoes, has been improved to be more efficient and to compute time step independent steady results. The model has been modified in order to limit the wake length used in the induction computation to a quarter revolution, independent on the radial position where the vortices are trailed. Furthermore, the model has been extended to include the effects of downwind convection in the wake modeling, replacing the prescribed circular arcs used originally by helical arcs.

The thrust that the far wake induction computation is based on has to be reduced by a coupling factor to account for the near wake induction. This coupling factor, which has been a user input in previous implementations of the model, is now computed during the simulation.

It has been shown that the corrections presented in this paper improve the near wake induction computation and make it possible to achieve a good resolution of the tip induction without the need for lower time steps than what is commonly used in aeroelastic wind turbine codes. The results have been compared against numerical integration of the induction due to trailed vorticity behind a three bladed rotor with good agreement. The correction for downwind convection has been found to be a necessary extension of the model to enable computations at high wind speeds.

The automated coupling factor computation has been shown to produce power and thrust levels close to the widely used BEM models. A comparison with full rotor CFD showed an improved agreement of the radial load distribution due to the added near wake model at high wind speed.

The work presented here enables using a more accurate and faster trailed vorticity computation for dynamic wind turbine simulations while retaining similar steady power and thrust results to well known BEM models in the full wind speed range. The dynamics of the model are expected to be an improvement compared to a standard BEM model. An ongoing validation of the dynamic behavior against a free wake vortex code will be published in the near future.

REFERENCES

1. Wilson R, Lissaman P. *Applied aerodynamics of wind power machines*. Oregon State University, 1974.
2. Madsen Aagaard H, Mikkelsen R, Sørensen N, Hansen M, Øye S, Johansen J. *Influence of wind shear on rotor aerodynamics, power and loads*. Denmark. Forskningscenter Risoe. Risoe-R-1611, 2007; 101–116.
3. Sørensen N. General purpose flow solver applied to flow over hills. PhD Thesis 1995. Published 2003.
4. Beddoes TS. A near wake dynamic model. *proc. of the AHS national specialist meeting on aerodynamics and aeroacoustics* 1987; .
5. Madsen HA, Rasmussen F. A near wake model for trailing vorticity compared with the blade element momentum theory. *Wind Energy* 2004; **7**:325–341.
6. Andersen P. Advanced load alleviation for wind turbines using adaptive trailing edge flaps: Sensoring and control. PhD Thesis 2010.
7. Wang T, Coton FN. A high resolution tower shadow model for downwind wind turbines. *Journal of Wind Engineering and Industrial Aerodynamics* 2001; **89**:873–892.
8. Hansen MH, Gaunaa M, Madsen HA. *A Beddoes-Leishman type dynamic stall model in state-space and indicial formulations*. Risø-R-1354: Roskilde, Denmark, 2004.
9. Larsen T, Hansen A. *How 2 HAWC2, the user's manual*. Denmark. Forskningscenter Risoe. Risoe-R-1597, 2007.
10. Kim T, Hansen AM, Branner K. Development of an anisotropic beam finite element for composite wind turbine blades in multibody system. *Renewable Energy* 2013; **59**:172.
11. Larsen TJ, Madsen HA, Larsen GC, Hansen KS. Validation of the dynamic wake meander model for loads and power production in the egmond aan zee wind farm. *Wind Energy* 2013; **16**(4):605–624, doi:10.1002/we.1563.
12. Yde A. Hawc2 wind turbine models 2014. Http://www.hawc2.dk/HAWC2%20Download/HAWC2%20model.aspx.
13. Jonkman J, Butterfield S, Musial W, Scott G. Definition of a 5-mw reference wind turbine for offshore system development. *Technical Report*, National Renewable Energy Laboratory 2009.
14. Heinz J. Partitioned fluid-structure interaction for full rotor computations using cfd. PhD Thesis 2013.

[III]

Comparison of a Coupled Near and Far Wake Model With a Free Wake Vortex Code

WIND ENERGY
Wind Energ. 0000; **00**:1–20
DOI: 10.1002/we

RESEARCH ARTICLE

Comparison of a Coupled Near and Far Wake Model With a Free Wake Vortex Code

G. R. Pirrung[1], V. A. Riziotis[2], H. A. Madsen[1], M. H. Hansen[1] and T. Kim[1]

[1] Wind Energy Department, Technical University of Denmark, Frederiksborgvej 399, Building 118, DK-4000 Roskilde, Denmark
[2] School of Mechanical Engineering, National Technical University of Athens, 9 Heroon Polytechneiou Str., GR15780, Athens, Greece

ABSTRACT

This paper presents the integration of a near wake model for trailing vorticity, proposed by Beddoes, with a BEM-based far wake model and a 2D shed vorticity model. The resulting coupled aerodynamics model is validated against lifting surface computations performed using a free wake panel code. The focus of the description of the aerodynamics model is on the numerical stability, the computation speed and the accuracy of unsteady simulations. To stabilize the near wake model, it has to be iterated to convergence, using a relaxation factor that has to be updated during the computation. Further, the effect of simplifying the exponential function approximation of the near wake model to increase the computation speed is investigated in this work. A modification of the dynamic inflow weighting factors of the far wake model is presented that ensures good induction modeling at slow time scales. Finally, the unsteady airfoil aerodynamics model is extended to provide the unsteady bound circulation for the near wake model and to improve the modeling of the unsteady behavior of cambered airfoils. The model comparison with results from a free wake panel code and a BEM model is centered around the NREL 5 MW reference turbine. The response to pitch steps at different pitching speeds is compared. By means of prescribed vibration cases, the effect of the aerodynamic model on the predictions of the aerodynamic work is investigated. The validation shows that a BEM model can be improved by adding near wake trailed vorticity computation. For a range of cases, results similar to those obtained by the free wake model can be achieved in a small fraction of computation time with the proposed model.

KEYWORDS
rotor aerodynamics, blade vibrations, vortex models

Correspondence
G. R. Pirrung, Wind Energy Department, Technical University of Denmark, Frederiksborgvej 399, Building 118, DK-4000 Roskilde, Denmark, E-mail: gepir@dtu.dk

Received . . .

1. INTRODUCTION

This work is based on a coupled aerodynamics model, where the trailed vorticity effects in the near wake are computed based on a model proposed by Beddoes [1], and the far wake computation is using the well-known blade element momentum (BEM) theory. The near wake model (NWM) is a simplified prescribed wake lifting line model, which efficiently computes the induction due to the vorticity trailed during a quarter of a rotor revolution. The coupled model can be seen as a hybrid code between a traditional BEM model and the more complex vortex codes: The computation time is in the order of magnitude of a BEM model, thus the addition of the near wake model in an aeroservoelastic code has only a small effect on the total computation speed. However, the accuracy of the computations is improved due to the added aerodynamic coupling between airfoil sections through the trailed vorticity. Thus the limitations of the BEM strip theory are alleviated. Especially in cases with large radial load gradients, for example close to trailing edge flaps or other aerodynamic devices or the blade root and tip, the cross sectional coupling will lead to an improved prediction of the steady and dynamic induction.

The coupled model using the modified BEM approach for the far wake has been proposed by Madsen and Rasmussen [2] and extended by Andersen [3]. Further improvement has been presented by Pirrung et al. [4], where an iterative procedure was used to ensure convergence and avoid numerical instabilities of the NWM. An application of the coupled model to estimate the critical flutter speeds of the NREL 5MW turbine [5], also including blades with modified stiffness, has been described by Pirrung et al. [6], where the coupled aerodynamics model has predicted 4-10 % higher critical flutter speeds than the unsteady BEM model in the aeroservoelastic wind turbine code HAWC2 [7, 8, 9].

In this paper, the iteration procedure of the NWM used in [4] is presented in more detail, as well as a method to compute the necessary relaxation factor during a simulation, removing the need for additional input or very conservative relaxation factors that are independent of spatial and temporal discretization and increase the computation time. Further, the NWM is simplified to accelerate the computations with small loss of accuracy of the unsteady results.

The dynamic responses to pitch steps and prescribed blade vibrations are validated by comparing them to results from the more complex free wake code GENUVP [10]. The focus in the pitch step cases is the dynamic induction response, while the prescribed vibration cases are evaluated based on aerodynamic work during a period of oscillation. It is found that the coupled aerodynamic model is capable of producing results that agree much better with results obtained from the free wake code than the unsteady BEM model in most cases, without a dramatic increase in computation time. The more accurate computation of aerodynamic work can have a considerable impact on the aeroelastic response in the case where the total damping is close to zero, such as for edgewise vibrations.

This paper is structured as follows: In the next section a short description of the NWM and a previous implementation of the coupling to a far wake model and shed vorticity model are presented. In Section 4, modifications to far wake and shed vorticity model are proposed to improve the interaction of these models with the near wake model and to increase the accuracy of the dynamic lift computation for cambered airfoils. This is followed by a description of the iterative procedure to stabilize the near wake model in Section 5. A way of simplifying the NWM to accelerate the computation is presented in Section 6. In Section 7 the free wake panel code used for validation of the coupled near and far wake model is briefly described. The effects of the model modifications and results from the code comparison are shown and discussed in Section 8.

2. ORIGINAL MODEL DESCRIPTION

The structure of the previous implementation, [2, 3], of the model is shown in Figure 1. From the velocity triangle, denoted as VT, follows a geometric angle of attack (AOA) α_{QS} and a relative velocity v_r. An effective AOA α_{eff} is obtained through a 2D modeling of the shed vorticity effects, which is briefly described in Section 2.3. This effective AOA is used to determine the aerodynamic forces and the thrust coefficient CT. In Section 2.2 will be shown how the thrust coefficient leads to a far wake induction factor a_{FW}, requiring a coupling factor k_{FW} as input. This section also contains the dynamic inflow model, using the weighting factors A_1 and A_2, which is used to determine the unsteady far wake induction $u_{FW,dyn}$.

Using this far wake induction, and the near wake induction from the previous time step, a new quasi steady AOA and relative velocity are determined. These lead to the bound circulation Γ_{QS}. The difference in Γ_{QS} between adjacent blade sections, denoted as $\Delta\Gamma$ in the following, determines the trailed vorticity. In the next section is shown how the induced velocity W due to the near wake, which is added to u_{FW} to obtain the total induced velocity at each blade section, follows from the trailed vortices.

2.1. Near wake model

The NWM enables a fast computation of the induction due to the trailed vorticity behind a rotor blade. The induction at a blade section at a distance x from a vortex element ds, cf. Figure 2 can be computed using the Biot-Savart law, but this computation is numerically expensive as the influence of each vortex element on the induction at each blade section has to be determined individually. Beddoes [1] proposed to avoid these expensive computations by assuming that the trailed

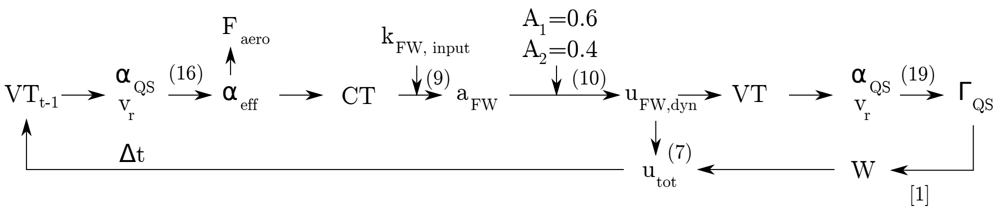

Figure 1. The previous implementation of the coupled near and far wake model, as described by Madsen and Rasmussen [2] and Andersen [3]. The numbers in parenthesis refer to the equations in the following sections.

vorticity follows circular vortex arcs in the rotor plane and limiting the computation to a quarter rotation. In this quarter rotation, the axial induction dw from a vortex element is decreasing as the vortex element moves away from the blade, starting with a value dw_0. This decreasing induction, following from the Biot-Savart law, is approximated by exponential functions:

$$\frac{\mathrm{d}w}{\mathrm{d}w_0} = \frac{\left(\frac{h}{r}\right)^2 \left[1 - \left(1 - \frac{h}{r}\right)\cos(\beta)\right]}{\left[1 + \left(1 - \frac{h}{r}\right)^2 - 2\left(1 - \frac{h}{r}\right)\cos(\beta)\right]^{3/2}} \approx 1.359 e^{-\beta/\Phi} - 0.359 e^{-4\beta/\Phi}, \tag{1}$$

where Φ is a geometrical factor depending on r, the radius from which the vortex is trailed and the distance h to the blade section where the induction is computed. The angle β determines how far behind the blade the vortex element is, cf. Figure 1. In this paper, an improved definition of Φ by Wang and Coton [11] is used:

$$\Phi = \begin{cases} \frac{\pi}{4}\left|\left(1 + \frac{h}{2r}\right)\ln\left(1 - \frac{h}{r}\right)\right| & \text{for } 0 < h/r < 1 \\ \frac{1 - \frac{h}{r}}{1.5 + \ln\left(1 - \frac{h}{2r}\right)} & \text{for } h/r < 0. \end{cases} \tag{2}$$

The numerically efficient trailing wake algorithm gives the induction W due to the trailed vorticity at time step i at a blade section s as:

$$W_s^i = \sum_{v=1}^{N_v} W_{s,v}^i, \tag{3}$$

where $W_{s,v}$ is the induction due to a single vortex arc v at the blade section. It is computed as

$$W_{s,v}^i = X_{s,v}^i + Y_{s,v}^i, \tag{4}$$

where $X_{s,v}^i$ and $Y_{s,v}^i$ are the components corresponding to both of the exponential functions in Equation (1):

$$X_{s,v}^i = X_{s,v}^{i-1} e^{-\Delta\beta_v/\Phi_{s,v}} + D_{X,s,v}\Delta\Gamma_v(1 - e^{-\Delta\beta_v/\Phi_{s,v}}), \tag{5a}$$

$$Y_{s,v}^i = Y_{s,v}^{i-1} e^{-4\Delta\beta_v/\Phi_{s,v}} + D_{Y,s,v}\Delta\Gamma_v(1 - e^{-4\Delta\beta_v/\Phi_{s,v}}), \tag{5b}$$

where $\Delta\Gamma_v$ is the trailed vortex strength, which depends on the radial difference in bound circulation between the blade sections adjacent to the vortex trailing point. The relative movement of the blade in the rotor plane during the time step at the vortex trailing point is denoted as $\Delta\beta_v = (v_{in-plane}/r)\Delta t$. The in-plane velocity component perpendicular to the lifting line is denoted as $v_{in-plane}$. It depends on blade section velocity due to rotor rotation and blade vibration as well as air speed, for example due to tangential induction or turbulence. Equations (5) show that the induction consists of a decreasing part of the induction at the previous time step, due to the previously trailed wake moving away from the blade, and the contributions from the newest element:

$$D_{X,s,v} = 1.359 \frac{r}{4\pi h|h|}\Phi_{s,v}, \quad D_{Y,s,v} = -\frac{0.359}{4}\frac{r}{4\pi h|h|}\Phi_{s,v}. \tag{6}$$

The trailing wake Equations (5) and (6) have been described by Pirrung et al. [12] and are less time step sensitive and computationally faster than the original equations by Beddoes.

The tangential induction is in this work modeled using the same algorithm as for the axial induction, but multiplying the contributions from the newest element, Equation (6), by the tangent of the helix pitch angle. Because the derivation of the tangential induction according to the Biot-Savart law leads to a different expression than Equation (1), an error is introduced when applying the same algorithm as for the axial induction. This error is discussed and quantified by Pirrung et al [12], with the conclusion that using a different expression for dw/dw_0 in case of tangential induction is not worth the increased computational effort.

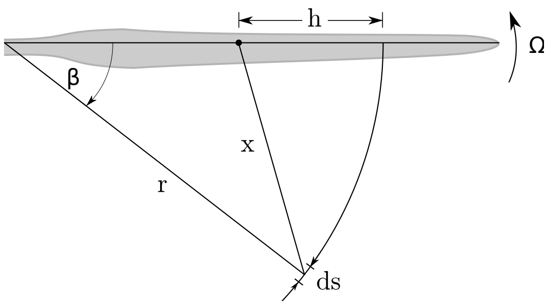

Figure 2. Geometry at a blade rotating with the constant angular velocity Ω. The downwash at a distance h from the vortex trailing point shall be computed. Since the infinitesimal vortex element with length ds has left the lifting line, the blade has been rotated by the angle β, resulting in the distance x between vortex element and the point of evaluation.

2.2. Coupling to far wake model

The NWM, which only computes a fraction of the total rotor induction, is complemented by a modified BEM model for the far wake. The total induced velocity at a blade section is computed as

$$u_{tot} = u_{FW} + W, \tag{7}$$

where u_{FW} is the far wake component of the induced velocity and W is the near wake component, cf. Equation (3).

The far wake component u_{FW} is computed based on the BEM model implementation in HAWC2 that uses a polynomial to relate the thrust coefficient with the axial induction factor:

$$a_{ref}(C_T) = k_3(C_T/F)^3 + k_2(C_T/F)^2 + k_1(C_T/F), \tag{8}$$

where F is the tip loss factor. The coefficients k_i have been determined to provide an approximation for the induction at low thrust according to BEM theory and the Glauert correction at high thrust. They are $k_3 = 0.08921$, $k_2 = 0.05450$ and $k_1 = 0.25116$.

To avoid to account multiple times for the near wake induction, the far wake model is not using a tip loss correction and it is based on a thrust coefficient C_T that is reduced by the coupling factor k_{FW} [2]. The quasi steady far wake induction factor is thus found as:

$$a_{FW}(C_T) = k_3(k_{FW}C_T)^3 + k_2(k_{FW}C_T)^2 + k_1(k_{FW}C_T) \tag{9}$$

Where k_{FW} is determined during the computation with the goal to closely match the thrust of a pure BEM computation as described in [12].

A dynamic inflow model has to be applied to the induction resulting from Equation (9). This work uses the dynamic inflow model implemented in HAWC2, where two parallel first order low pass filters are applied on the quasi steady induced velocities $u_{FW,QS} = a_{FW}u_\infty$ from the BEM model:

$$u^i_{FW,dyn} = A_1 u^i_1 + A_2 u^i_2 \tag{10}$$

$$u^i_1 = u^{i-1}_1 e^{-\Delta t/\tau_1} + u^i_{FW,QS}(1 - e^{-\Delta t/\tau_1}) \tag{11}$$

$$u^i_2 = u^{i-1}_2 e^{-\Delta t/\tau_2} + u^i_{FW,QS}(1 - e^{-\Delta t/\tau_2}). \tag{12}$$

In a pure BEM computation and the previous far wake model implementation, the factors A_i are $A_1 = 0.6$ and $A_2 = 0.4$. They are used to divide the induction into a faster and slower reacting part, corresponding to a faster time constant τ_1 and the slower time constant τ_2. Both time constants are a function of radius and mean loading. The constants A_i and τ_i have been tuned to the actuator disc simulations of step changes in uniform loading [13].

2.3. Unsteady airfoil aerodynamics model

The sketch in Figure 3 illustrates how the shed vorticity due to the time variation of the bound circulation induces a downwash $w_{3/4}$ at the three quarter chord of an airfoil. This downwash will change the angle of attack and thus the lift, drag and moment coefficients according to the airfoil polars, as well as the directions of the aerodynamic forces. The inviscid part of the unsteady airfoil aerodynamics model in Hansen et al. [14] treats the shed vorticity effects as a time lag on the angle of attack according to Jones' function for a flat plate. The effective angle of attack α_{eff}, which determines the magnitude and direction of the unsteady aerodynamic forces, is computed as:

$$T^i_0 = \frac{c}{2v^i_r} \tag{13}$$

$$x^i_1 = x^{i-1}_1 e^{-0.0455\frac{\Delta t}{T^i_0}} + \frac{1}{2}(\alpha^i_{QS} + \alpha^{i-1}_{QS})0.165 v^i_r (1 - e^{-0.0455\frac{\Delta t}{T^i_0}}) \tag{14}$$

$$x^i_2 = x^{i-1}_2 e^{-0.3\frac{\Delta t}{T^i_0}} + \frac{1}{2}(\alpha^i_{QS} + \alpha^{i-1}_{QS})0.335 v^i_r (1 - e^{-0.3\frac{\Delta t}{T^i_0}}) \tag{15}$$

$$\alpha^i_{eff} = \frac{1}{2}\alpha^i_{QS} + (x^i_1 + x^i_2)/v^i_r, \tag{16}$$

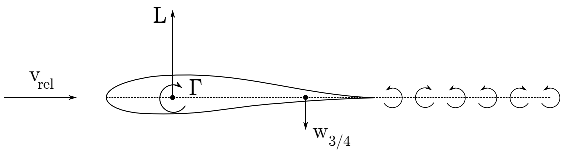

Figure 3. Cambered airfoil in parallel inflow to the chord line. The shed wake corresponds to the time history of the bound circulation.

where the superscript i denotes the time step and c the chord length. Further, α_{QS} is the quasi steady angle of attack resulting from the velocity triangle at the blade section and v_r denotes the corresponding relative velocity.

3. MODEL OVERVIEW

The structure of the current implementation of the coupled near and far wake model is shown in Figure 4. The changes to the previous implementation, cf. Figure 1 are:

- The weighting factors A_i of the far wake dynamic inflow are adjusted during the computation to account for the induction computed by the near wake model, which is explained in Section 4.1.
- The trailed vorticity is no longer based on the quasi steady bound circulation Γ_{QS}, but instead on a dynamic bound circulation Γ_{dyn}. The computation of the dynamic bound circulation is shown in Section 4.2.1.
- The near wake induction is computed in an iteration loop, which is detailed in Section 5.
- The coupling factor is no longer needed as input, but instead continually updated during the computation, as described in [12].
- The trailed vorticity is assumed to follow helix arcs to account for the downwind convection of the trailed vorticity. To achieve this, Φ, Equation (2), is multiplied with a correction function f, depending on the blade section and vortex trailing point, as well as the helix angle at which the vortex is trailed [12].
- The computation of α_{eff} according to shed vorticity effects is improved for cambered airfoils, which is explained in Section 4.2.2.

4. MODIFICATIONS TO FAR WAKE AND SHED VORTICITY MODEL

4.1. Adapting the weighting of the dynamic inflow time filters

The dynamic inflow model described in Section 2.2, which has been tuned for BEM computations, has to be modified if a part of the induction is covered by the NWM. The objective is to obtain a similar slow induction response with the coupled near and far wake model as with an unsteady BEM model.

This requires a modification of the constants A_1 and A_2 in Equation (10). The new constants A_i are computed based on the far wake induction factor a_{FW} from Equation (9) and a reference induction factor obtained from a BEM model with tip loss correction, Equation (8). The weighting constants for the far wake model are determined such that roughly 40 % of the total induction are considered to be reacting slowly, as in the original dynamic inflow model for BEM computation, Equation (10):

$$A_{1,FW} = \frac{0.4 a_{ref}}{a_{FW}} \tag{17}$$

$$A_{2,FW} = 1 - A_{1,FW}. \tag{18}$$

The factors are continuously updated during the computations. A first order low pass filter with the far wake time constant τ_2 of the dynamic inflow model is applied on $A_{1,FW}$ to make sure this model does not introduce unphysical rapid induction variations due to instantaneous changes of the weighting factors.

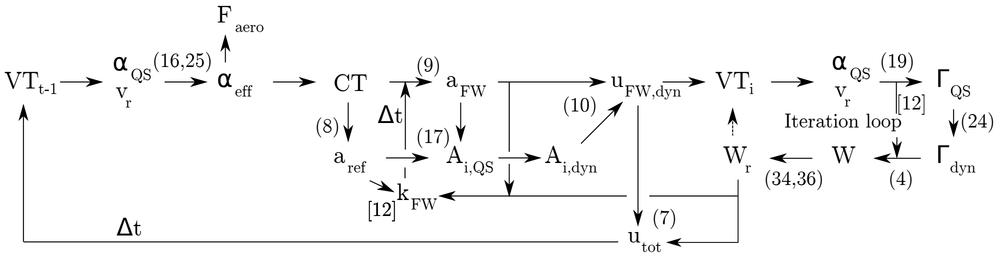

Figure 4. Overview of one time step in the coupled near and far wake model used in this work. Relevant equation numbers and references are included.

4.2. Extensions of the unsteady airfoil aerodynamics model

4.2.1. Unsteady circulation computation

The influence of shed vorticity on the bound circulation buildup has to be be considered when determining the strength of the trailed vortices of the NWM. Joukowski's relation between quasi steady lift L_{QS} and circulation Γ_{QS},

$$\Gamma_{QS} = \frac{L_{QS}}{\rho v_r} = \frac{1}{2} v_r c C_L, \tag{19}$$

which has been used by Madsen and Rasmussen [2] and Andersen [3] to determine the bound vorticity, is not valid for unsteady conditions. The error of calculating the circulation based on the unsteady lift at an airfoil section depends on the reduced frequency $k = \omega c/(2v_r)$, where ω is the angular velocity, c is the chord length, and v_r is the relative flow speed. For an airfoil pitching harmonically about the three-quarter chord point, the error has been estimated by Madsen and Gaunaa [15] to be 10% at $k = 0.1$ and 100 % at $k = 0.8$, which for the NREL 5 MW reference turbine at rated wind and rotor speed corresponds to frequencies of about 1.2 and 9.8 Hz at 60 m rotor radius with a chord of 2 m. Except for the first flapwise and edgewise bending frequencies, most relevant modal frequencies for modern blades are between these values, which shows that it is important to include a modeling of the unsteady circulation.

In this paper, the step response of the circulation is approximated by the three term indicial function used in Madsen and Gaunaa [15].

$$\Gamma_{dyn}/\Gamma_{QS} = 1 - A_{\Gamma,1}e^{-b_{\Gamma,1}\tau} - A_{\Gamma,2}e^{-b_{\Gamma,2}\tau} - A_{\Gamma,3}e^{-b_{\Gamma,3}\tau}, \quad \text{where} \tag{20}$$

$$\tau = \Delta t \frac{2v_r}{c}, \quad A_{\Gamma,1} = 0.5547, \quad A_{\Gamma,2} = 0.1828, \quad A_{\Gamma,3} = 0.2656, \tag{21}$$

$$b_{\Gamma,1} = 0.3064, \quad b_{\Gamma,2} = 0.0439, \quad b_{\Gamma,3} = 3.227 \tag{22}$$

The algorithm is implemented analogue to the computation for the effective angle of attack in Equations (13)-(16):

$$x^i_{\Gamma,j} = x^{i-1}_{\Gamma,j} e^{-b_{\Gamma,j}\frac{\Delta t}{T^i_0}} + \frac{A_{\Gamma,j}}{2}(\Gamma^i_{QS} + \Gamma^{i-1}_{QS})(1 - e^{-b_{\Gamma,j}\frac{\Delta t}{T^i_0}}) \tag{23}$$

$$\Gamma^i_{dyn} = x^i_{\Gamma,1} + x^i_{\Gamma,2} + x^i_{\Gamma,3}, \tag{24}$$

where the quasi steady circulation is computed from the quasi steady lift coefficient using Equation (19).

4.2.2. Unsteady aerodynamics of cambered airfoils

Any change in bound circulation Γ, which is a function of $v_r C_L$, cf. Equation (19) should lead to the corresponding shed vorticity. The implementation of the shed vorticity model according to Hansen et al. [14], cf. Equations (14-16) is based on the term $\alpha_{QS} v_r$. The camber of the airfoil is neglected in this computation of the shed vorticity effects. We propose in this work to replace α_{QS} in Equations (14 to 16) by $\alpha_{QS,camber}$, with

$$\alpha_{QS,camber} = \alpha_{QS} - \alpha_0, \tag{25}$$

where α_0 is the zero lift angle of the airfoil. The impact of this modification is shown for basic cases of relative velocity changes in Figures 5 and 6, where an airfoil with a 2π lift gradient, a 2 m chord length, a zero lift angle of -3° and a drag coefficient of $C_D = 0.005$ has been simulated. The airfoil characteristics and chord length have been chosen to be similar to the outboard region of the NREL 5MW reference turbine and the geometric angle of attack has been chosen as zero, to show the isolated effect of airfoil camber. In Figure 5, the variation of effective angle of attack due to a step change of relative speed from 70 m/s to 71 m/s within a time step of 0.01 s is shown. Without the effect of camber , the change in relative speed has no influence on the angle of attack, because α_{QS} is a constant zero. The effect of camber leads to a lower angle of attack due to the shed vorticity caused by the increase in bound circulation. The camber effect is small, and the angle of attack changes only by less than 0.02 degrees immediately after the relative speed step. In Figure 6 the induced drag due to angle of attack changes is compared to the viscous drag in case of a vibration of the airfoil section parallel to the inflow. There would be no induced drag in this example if camber was excluded from the effective angle of attack computation. The amplitude of the vibration is 1 m, the frequency 1 Hz. The effect of induced drag is of the same order of magnitude as the airfoil drag, which indicates the importance of including the airfoil camber in the unsteady airfoil aerodynamics model. The camber effect is included in all further computations presented in this paper except in the left plot of Figure 19, where it is excluded to investigate its importance on in-plane blade vibrations.

In the unsteady circulation computation described in the previous section, the camber is accounted for through the quasi steady circulation Γ_{QS}, which is based on the lift coefficient, cf. Equation (19).

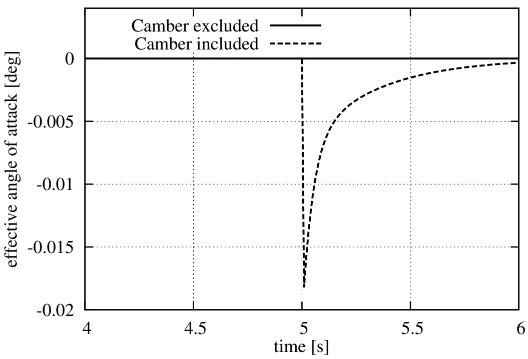

Figure 5. Effect of including camber in the unsteady aerodynamics model on effective angle of attack during a step in relative velocity.

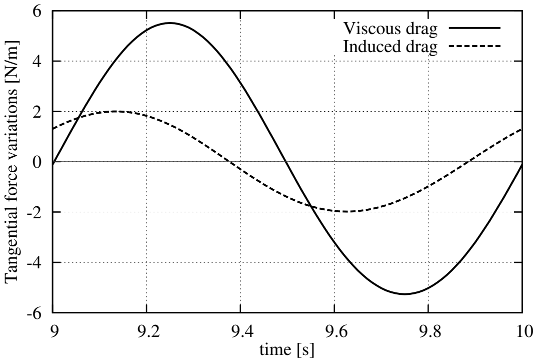

Figure 6. Comparison of viscous drag and induced drag during oscillations of a cambered airfoil parallel to the inflow at 1 Hz. The effect of camber is included as proposed in Equation (25). The mean drag has been subtracted.

5. ITERATIVE NEAR WAKE AND SHED VORTICITY MODEL

5.1. Iteration scheme

The NWM can become numerically unstable depending on the time step, operating point of the turbine, blade geometry and radial calculation point distribution, [4]. Figure 8 shows the maximum time step where a stable computation is possible for a fine and coarse geometry definition, shown in Figure 7, of the NREL 5 MW blade. The coarse geometry definition is a blade geometry typically distributed for BEM computations and the fine distribution is more suitable for computations with higher fidelity codes. The aerodynamic calculation points and vortex trailing points follow a cosine distribution, which means they are placed at equi-angle increments. The time steps have been determined in a numerical experiment, where the time step has been decreased until large oscillations of the induction disappear. The results are accurate to the first significant digit. It can be seen that the finer blade geometry leads to a more stable computation. This can be explained by the smoother blade tip, where the blade chord is approaching zero. Thus the radial circulation gradient at the very blade tip is smaller and the vortex strength of the tip vortex is distributed to several weaker trailed vortices in the tip region that are less likely to cause numerical instabilities. In a coupled aeroelastic simulation, the small stable time steps for resolutions of 30 to 60 points would lead to a very slow computation especially in case of the coarser blade geometry.

The numerical instability which occurs at larger time steps can be explained as follows: The axial induction due to trailed vortices typically reduces the angle of attack at a blade section, which in attached flow leads to a reduced lift. In the original implementation of the NWM the constant circulation trailed during a time step is only depending on the flow

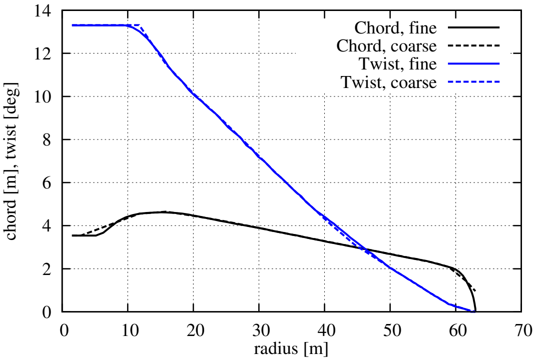

Figure 7. Coarse and fine blade geometry for the NREL 5MW reference turbine. The coarse definition is a typical geometry definition for BEM based computations. The finer geometry is smoothed for use in computational fluid dynamics and free wake codes.

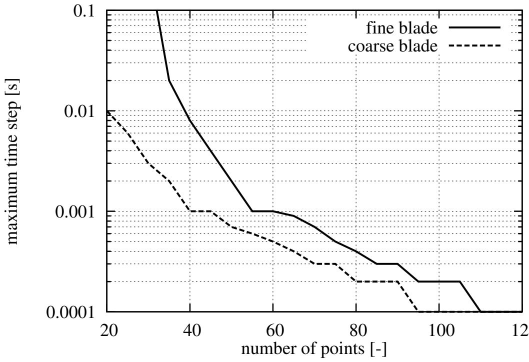

Figure 8. Maximum stable time step depending on number of points for the coarse and fine blade geometries of the NREL 5 MW reference turbine. The points are distributed using a full cosine distribution, [4]. The results are obtained through numerical experiment.

conditions at the blade at the beginning of a time step. Thus a longer time step will lead to a bigger induction and thus a further reduction in lift in the next time step. If the time step is too large, the induction can become big enough to create a negative lift in the next time step, that is bigger in absolute value than the previous positive lift. This in turn leads to stronger trailed vortices of opposite sign, which will cause even bigger induced velocities in the opposite direction, which again leads to stronger vortices.

To stabilize the NWM the balance between trailed vortex strength based on the sectional circulation and the induced velocities are iterated to equilibrium in each time step, which removes the need for small time steps to stabilize the aerodynamics model. The iteration is structured as follows:

1 The quasi-steady circulation is computed according to Joukowskis law using the velocity triangle at the airfoil section based on the induction from the last iteration.

2 The unsteady circulation after half a time step is computed including shed vorticity effects, cf. Section 4.2

3 This unsteady circulation defines the constant vortex strengths trailed during a time step

4 These constant vortex strengths lead to an induction at all airfoil sections.

5 The new induction is combined from the inductions from step 1 and 4 by applying a relaxation factor: $w_i = w_{i-1}r + w_i(1-r)$, where the subscript i indicates the iteration number. If w_i is sufficiently close to w_{i-1}, it is the desired converged induction.

The BEM model for the far wake is excluded from this iteration procedure. The AOA and relative velocity used to compute the far wake induction are the values from the converged iteration in the previous time step. This is accelerating the computation and is feasible because the near wake effects are on a much faster time scale than the dynamic inflow effects in the BEM model.

5.2. Estimation of the necessary relaxation factor

In the following, an estimation of the relaxation factor for a blade section is described. A conservative estimation is based on the least stable case which is characterized by the following properties:

- One single blade section with one vortex trailing from each side. Adjacent sections would tend to have similar circulations and therefore reduce the vortex strengths and the corresponding induction at the blade section. The trailed vortices on both sides of the section depend only on the bound circulation Γ of that section.
- The lift coefficient is linearly dependent on the angle of attack, $C_L = 2\pi\alpha$. A reduced but still positive gradient due to stall would stabilize the model.
- No prior trailed vorticity is present. It would stabilize the model, because the induction would not only be determined by the momentary circulation at the section, but also by the decaying influence of the wake trailed before. If the model converges in the very first time step, with a given induction at the section from the previous iteration then the iterations will also converge with prior trailed vorticity.
- The helix angle at which the vortices are trailed is assumed to be small. Thus all the induction due to trailed vorticity is assumed to be axial induction.

With these assumptions, the downwash after a time step Δt is:

$$w^i = \sum_{v=1}^{2}(-1)^v \Gamma(D_X^i(1-e^{-\Delta\beta/\Phi_v}) + D_Y^i(1-e^{-4\Delta\beta/\Phi_v})), \tag{26}$$

where the subscript v denotes the vortex further inboard ($v=1$) and outboard ($v=2$) of the section with the bound circulation Γ. The subscript i denotes the iteration. Because the tangential induction is neglected, $\Delta\beta$ is only a function of the rotation speed of the turbine and the time step. Thus Γ is the only variable in Equation (26) that depends on the induction at the section:

$$\Gamma = \frac{\Gamma_{dyn}}{\Gamma_{QS}}\frac{1}{2}cC_L v_r \tag{27}$$

$$= \frac{\Gamma_{dyn}}{\Gamma_{QS}}c\pi v_r \alpha \tag{28}$$

$$= \frac{\Gamma_{dyn}}{\Gamma_{QS}}c\pi\sqrt{(v_\infty - w_{i-1})^2 + (\Omega r)^2}\,\arctan\left(\frac{v_\infty - w_{i-1}}{\Omega r}\right), \tag{29}$$

where v_∞ is the free wind speed and the step response function from Equation (20) evaluated at half a time step gives Γ_{dyn}/Γ_{QS} because we consider the first time step, thus a buildup of the circulation from zero.

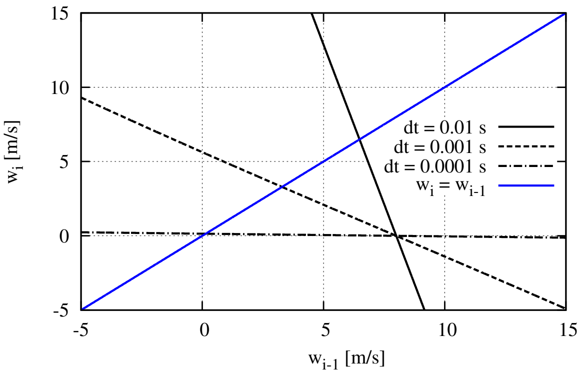

Figure 9. Downwash after an iteration as a function of the downwash from the preceding iteration in case of a single section with trailed vortices.

Equation (26) is plotted for different time steps as a function of w_{i-1}, the induction from the previous iteration, for the blade tip section of the NREL 5MW reference turbine at 8 m/s in Figure 9. The airfoil camber is neglected. The intersections of the curves with the blue curve ($w_i = w_{i-1}$) are the converged solutions, where a new iteration would lead to exactly the same induction as the previous one. The calculations for different time steps have different converged inductions, because the length of the trailed vortex filaments is proportional to the time step. But not only the converged solution changes, also the gradient of the curves, which leads to a condition for convergence: If the distance from the converged solution decreases during a time step,

$$|w_i - w_{conv}| < |w_{i-1} - w_{conv}|, \tag{30}$$

the iterative process converges. As seen in Figure 9, the gradient of the curves is almost independent of w_{i-1}. The gradients are negative because induction reduces the angle of attack. Therefore an approximation of condition (30) can be used:

$$\frac{\mathrm{d}w_i}{\mathrm{d}w_{i-1}} > -1. \tag{31}$$

This gradient can be derived from Equations (26) and (29) as:

$$\frac{\mathrm{d}w_i}{\mathrm{d}w_{i-1}} = \frac{\Gamma_{dyn}}{\Gamma_{QS}}\pi c(B_1 - B_2)\left(\frac{\alpha(v_\infty - w_{i-1})}{v_r} + \frac{v_r}{\Omega r\left(\left(\frac{v_\infty - w_{i-1}}{\Omega r}\right)^2 + 1\right)}\right), \quad \text{where} \tag{32}$$

$$B_v = (-1)^v\left(D_{X,v}\left(1 - e^{-\Delta\beta/\Phi_v}\right) + D_{Y,v}\left(1 - e^{-4\Delta\beta/\Phi_v}\right)\right) \tag{33}$$

The gradient is mainly depending on the time step and point density (through B_1 and B_2) and the rotational speed.

Instead of reducing time step and point density until a simulation is stable, which can lead to time steps orders of magnitude smaller than commonly used in aeroelastic codes and low spatial resolution, a relaxation factor r can be introduced, so that:

$$w_{i,r} = w_i(1 - r) + w_{i-1}r. \tag{34}$$

The derivative of this downwash with regard to the old downwash is:

$$\frac{\mathrm{d}w_{i,r}}{\mathrm{d}w_{i-1}} = \frac{\mathrm{d}w_i}{\mathrm{d}w_{i-1}}(1 - r) + r. \tag{35}$$

For the minimum relaxation factor r, that allows for a stable computation ($\mathrm{d}w_{i,r}/\,\mathrm{d}w_{i-1} = -1$), follows:

$$r = -\frac{1 + \frac{\mathrm{d}w_i}{\mathrm{d}w_{i-1}}}{1 - \frac{\mathrm{d}w_i}{\mathrm{d}w_{i-1}}}, \tag{36}$$

which can be determined depending on the time step Δt, the point distribution, and the number of points on the blade.

In the initial phase of the simulation, the maximum relaxation factor for all blade sections can be quickly determined by setting $w_{i-1} = 0$ in Equation (32) and looping through the sections. The highest necessary relaxation factor for one section that has been found is then used for the whole blade. As the simulation continues, the relaxation factor can be updated whenever there are big changes in rotational speed, induction, or blade pitch. If the relaxation factor is updated every several time steps, determining the relaxation factor takes negligible computation time. Choosing a slightly more conservative relaxation factor than what has been estimated will ensure stability also in different conditions than the ones the factor was based on.

6. ACCELERATING THE NWM

In this section, an approach to accelerate the model is presented. The number of exponential terms used to approximate the decreasing induction with increasing distance from the blade in Equation (1) is reduced to one. Using only one exponential term removes the Y_w component in the near wake algorithm, Equation (5b) and thus halves the computation time.

The reduced approximation function is defined as:

$$\frac{\mathrm{d}w}{\mathrm{d}w_0} \approx 1.359e^{-\beta/\Phi} - 0.359e^{-4\beta/\Phi} \approx A^* e^{-\beta/\Phi^*}. \tag{37}$$

The values of A^* and Φ^* are found by solving the following equations:

$$W(\beta = \infty) = \int_0^\infty 1.359e^{-\beta/\Phi} - 0.359e^{-4\beta/\Phi}\,\mathrm{d}\beta = \int_0^\infty A^* e^{-\beta/\Phi^*}\,\mathrm{d}\beta \tag{38}$$

$$\int_0^\infty W(\beta = \infty) - W(\beta)\,\mathrm{d}\beta = \int_0^\infty \Phi(1.359e^{-\beta/\Phi} - \frac{0.359}{4}e^{-4\beta/\Phi})\,\mathrm{d}\beta = \int_0^\infty \Phi^*(A^* e^{-\beta/\Phi^*})\,\mathrm{d}\beta. \tag{39}$$

Equation (38) ensures that the quasi steady induction $W(\beta = \infty)$ of the reduced model is equal to the one computed by the original model for a trailed vortex with constant strength. Equation (39) ensures a good dynamic behavior by requiring the time integral of the difference between dynamic and quasi steady induction to be identical to the original model. The solution to these equations is

$$A^* = \frac{(1.359 - 0.359/4)^2}{1.359 - 0.359/16}, \qquad \Phi^* = \Phi\frac{1.359 - 0.359/16}{1.359 - 0.359/4} \tag{40}$$

A comparison of the buildup of induction in time, corresponding to the integral of the exponential functions, is shown in Figure 10. The largest deviations of the reduced model from the original model are below 2.5 % of the quasi steady induction $W(\beta = \infty)$.

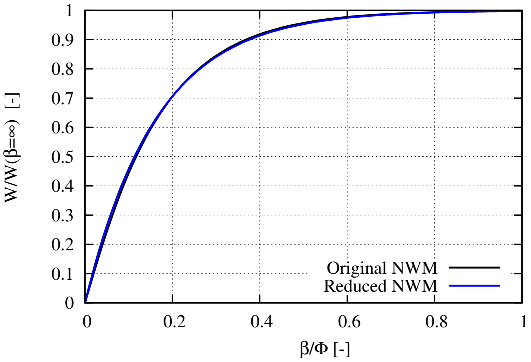

Figure 10. Comparison of induction buildup between full NWM and reduced NWM, depending on the length of a trailed vortex filament with constant circulation.

7. FREE WAKE CODE

GENUVP is a potential flow solver combining a panel representation of the solid boundaries (blades) with a vortex particle representation of the wake. In the present work, the blades are considered as thin-lifting surfaces carrying piecewise constant dipole distribution (equivalent to horseshoe type vortex filaments). Blades shed vorticity in the wake along their trailing edges and their tips (vorticity emission line). In the model a hybrid wake approach is followed. The near wake part, consisting of the newly shed vorticity trailed within the current time step, is modelled as a vortex sheet also carrying piecewise constant dipole distribution. Within every time step, a strip of wake panels is released that are in contact with the emission line. Applying the no-penetration boundary condition at the centre of each solid panel and the Kutta condition along the emission line the unknown dipole intensities are determined. Then at the end of each time step, the newly shed vorticity is transformed into vortex particles and then all vortex particles are convected downstream with the free flow velocity (free wake representation) into their new positions. The layout of the modelling is shown in Figure 11. Details of the model can be found in [10]. Since GENUVP is defined as a potential flow solver, the loads need correction in order to account for viscous effects. This is done by means of the generalized ONERA unsteady aerodynamics and dynamic stall model [16]. The potential load is calculated by integrating pressures (pressure differences between pressure and suction side) over the lifting surfaces. Then, through a consistent definition of the local flow angle of attack and relative flow velocity corrections are applied on the potential loads on the basis of the ONERA model. Thereby, the effects of viscous drag and flow separation are taken into account [17]. In the case of aeroelastic coupling, the aerodynamic part will receive the deformed geometry and the deformation velocity and feedback the loading. The deformed geometry as well as the deformation velocities are introduced into the boundary conditions and therefore the flow is accordingly adjusted.

8. RESULTS

In the following section, the effectiveness of the iteration procedure and the estimation of the relaxation factor are demonstrated for a horseshoe vortex. Then in Section 8.2 the unsteady induction predicted by the coupled near and far wake model is compared with results from an unsteady BEM model and the free wake code described in Section 7. Pitch steps and prescribed vibrations of the blades of the NREL 5 MW reference turbine are investigated.

8.1. Iteration procedure

In this section the effectiveness of the iteration procedure is shown for a single horseshoe vortex and the estimated relaxation factor according to Section 5.2 is compared to minimum relaxation factors obtained by trial-and-error.

8.1.1. Effectiveness of iteration procedure

To illustrate the efficiency of the iterative implementation, induction buildups for a simplified case are shown in Figure 12. The simple test case is a wing with a span of 0.3 m and a constant bound circulation, so that only two vortices with opposite vortex strength are trailed at the edges. To use the NWM, the wing is modeled as the only aerodynamic section at the end of a 10 km long blade. Therefore the air is moving almost orthogonal to the wing in its proximity. The free stream velocity is 70 m/s. At t=1 s, the geometric AOA of the wing with a symmetrical profile is increased from 0 to 5 degrees within 0.02 s. The lift coefficient is that of a flat plate, $c_L = 2\pi\alpha$, the chord is 1 m. The buildup of the circulation is modeled as in the coupled model, cf. Equation (24). The left side of Figure 12 shows the induction buildup for different time steps without iterating, the right side shows the effect of the iteration procedure. Both the overshoot of the induction

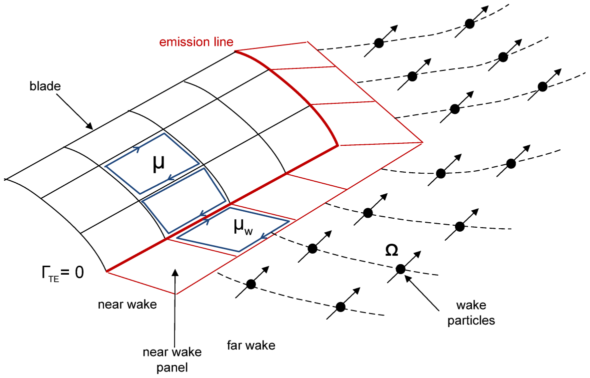

Figure 11. Layout of the free-wake modelling of a blade: black lines define the blade surface panels; red lines define the wake generated within a time step; symbols represent freely moving particles.

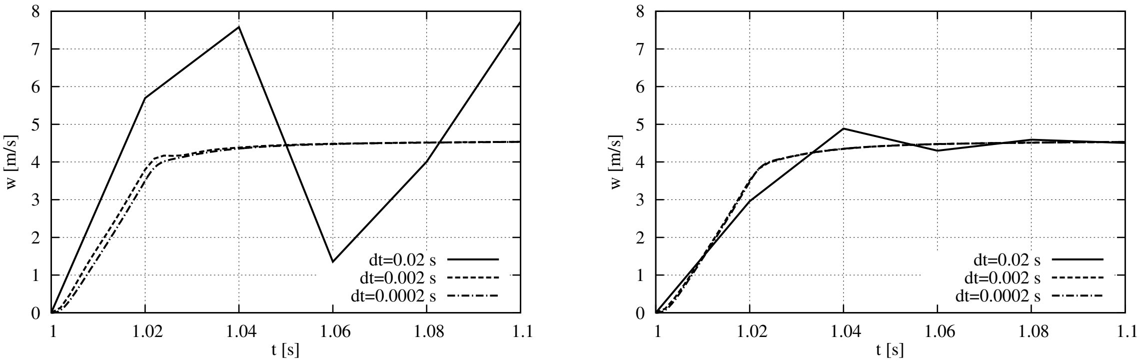

Figure 12. Buildup of the downwash for a horseshoe vortex depending on the time step. The NWM tends to be unstable (left) but can be stabilized by iterating to convergence of the downwash (right).

for a time step of 0.002 s and the oscillations for a time step of 0.02 s are reduced by the iteration procedure. The result with a time step of 0.02 s is not perfect, but the iterative model is clearly more stable and computes less time step dependent results in this demanding test case.

8.1.2. Validation of the estimated relaxation factor

The relaxation factors estimated as proposed in Section 5.2 are compared with relaxation factors obtained by trial-and-error in Figure 13. The factors from trial-and-error have been obtained by running simulations for the NREL 5 MW turbine in the 8 m/s and 25 m/s cases for different numbers of aerodynamic sections starting with a relaxation factor of either 0.0 or the relaxation factor that allowed a stable computation for lower spatial resolution. Whenever the computation gets unstable, the relaxation factor is increased by 0.001 and the simulation restarted until the minimum relaxation factor for stable computation is found. The comparison in Figure 13 shows that the estimated relaxation factor is conservative, but the safety margin towards unstable computation is smaller in the 25 m/s case.

8.2. Comparison of the coupled model with a BEM model and the free wake panel code

In this section the induction and loads predicted by the coupled model are compared with other codes in different cases, namely pitch steps in Section 8.2.1 and blade vibrations in Section 8.2.2. All following results are obtained for the refined blade model shown in Figure 7. The spatial distribution is identical in all computed cases: For the computations with the unsteady BEM model and the coupled model, the blade has been discretized using 40 radial aerodynamic stations. Because the vortices are trailed at the blade root and tip and in between the aerodynamic stations, there are a corresponding 41 vortex trailing points in the coupled model computations. For the computationally more expensive lifting surface free

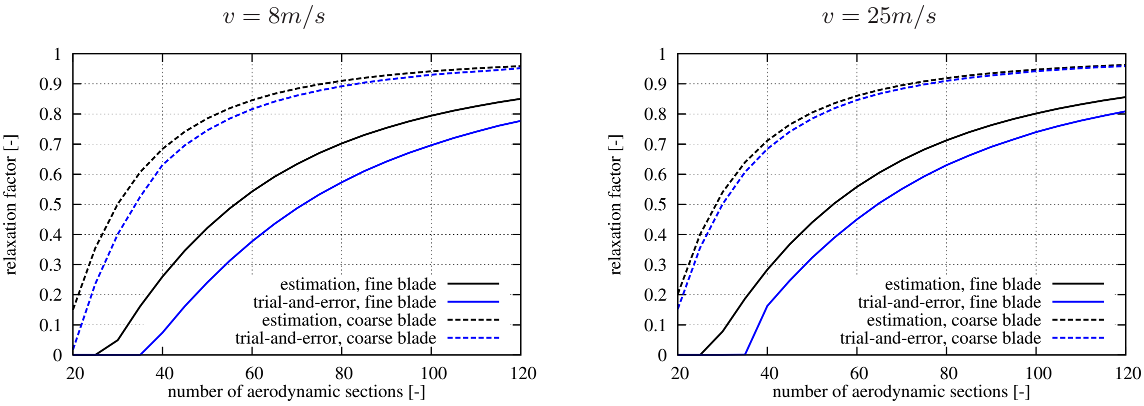

Figure 13. Estimated relaxation factor compared with the lowest stable relaxation factor from trial-and-error depending on the number of aerodynamic sections. The time step is 0.02 seconds. The estimated relaxation factors, Equation (36), are conservative and the influence of the refined blade geometry is captured.

wake simulations, the blade has been discretized using 35 grid lines in the span wise and 11 lines in the chord wise direction. Compared to the computations with the faster models, the resolution was mainly reduced close to the blade root.

8.2.1. Pitch steps

Pitch steps with a stiff blade have been performed to compare the performance of the coupled aerodynamic model to a less complex unsteady BEM model and the more complex free wake panel code. The NREL 5 MW reference turbine is operating at a wind speed of 8 m/s and a rotation speed of 9.2 rpm. The turbine starts with blades that are pitched by 5 degrees to feather. In the free wake simulations the pitch steps are resolved with a resolution of 120 steps per rotor revolution, which translates to a time step of 0.054 seconds. The BEM and coupled model simulations used a time step of 0.05 seconds. After 60 seconds simulation time, the blades are pitched to 0 degrees with a constant pitch rate in either 1 or 4 seconds. Because the radial force distributions before and after the pitching are not in exact agreement for the three models, the forces are normalized in the following comparisons. To normalize, the values of the axial force immediately before the pitch step have been subtracted from each respective time series, which is then divided by the corresponding axial force at 45 seconds after the beginning of the pitch step.

Figures 14 and 15 show the axial force response at a position at mid-blade and close to the blade tip. In case of the fast pitch step, the free wake code predicts a slower force response during the pitch step than the BEM model. The results of the coupled model during the pitch step lie in between the other codes. In the free wake code results, some oscillations due to the changing wake geometry are present after the pitch step that can not be seen in the results of the less complex codes, especially at the mid blade section. These oscillations make it difficult to judge if the BEM model or the coupled model are predicting the overshoot closer to the free wake code, the results of which are in between the two. However, at the tip section the oscillations are less pronounced and the agreement between the coupled model and the free wake model is better.

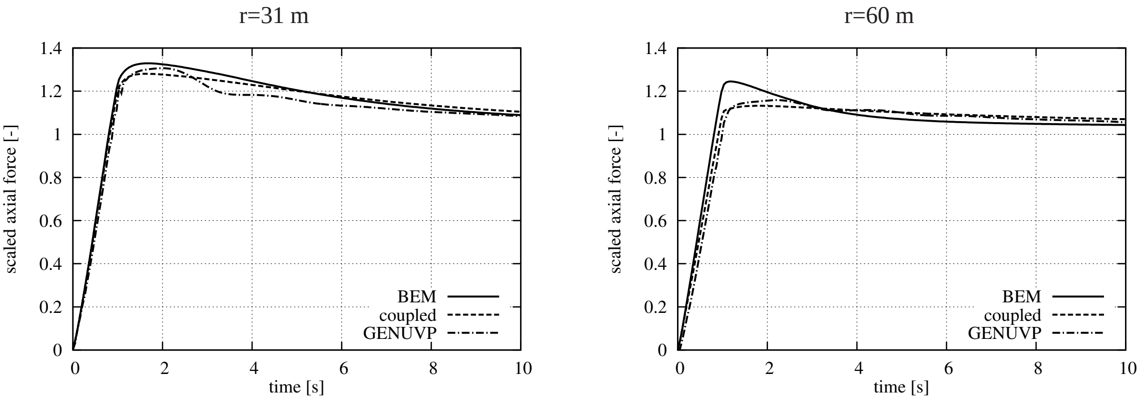

Figure 14. Scaled axial force at different radial positions during and after a pitch step by 5 degrees in 1 s.

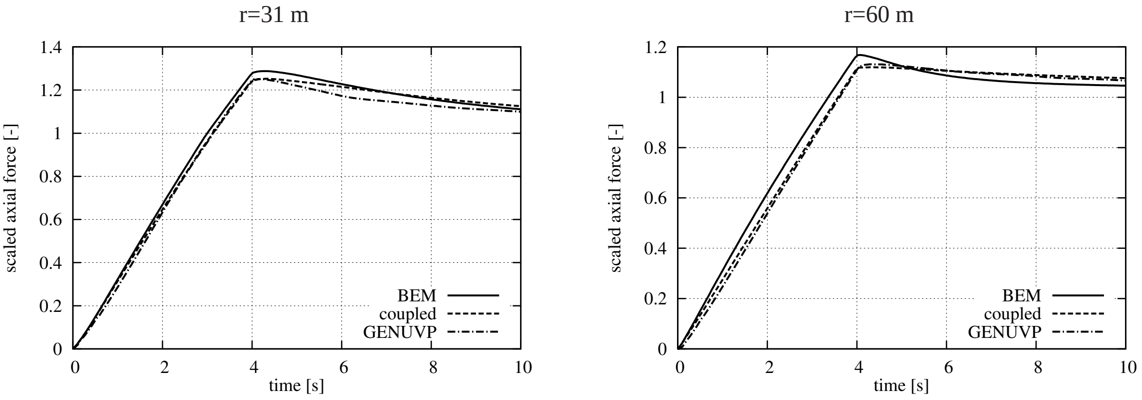

Figure 15. Scaled axial force at different radial positions during and after a pitch step by 5 degrees in 4 s.

The results of the slower pitch step in Figure 15 show less oscillations of the free wake code results, but they are still visible at the mid blade section. The coupled model and the free wake code agree well on the slope of the force increase during the pitching motion. The steeper slope predicted by the BEM model can be explained by a slower reaction of the induction than in the other codes. In this case, the results from the coupled model agree better with the free wake code than the BEM results, both during the pitching motion and on the predicted overshoot.

Axial force distributions for a partial pitch comparison are shown in Figure 16. This comparison used the same starting conditions as the comparisons above (8 m/s wind speed and the blade pitched by 5 degrees to feather), but only the outer half of the blade is pitched to zero degrees during 1 second. As shown in the left plot of Figure 16, the effect of the cross sectional coupling due to the trailed vorticity at the mid blade is predicted by both the coupled aerodynamics model and the free wake code at a similar degree. Compared to the BEM model, these codes predict a smoothing of the radial load distribution around the discontinuity of the blade pitch.

In the right plot of Figure 16, the time history of the axial force between the coupled model and the free wake code is compared at a radius of 21.6 meters. Because this part of the blade is not pitching, the force predicted by the BEM model is constant, therefore it is not included in this comparison. The behavior of the coupled model and GENUVP shows a similar time scale, but the overshoot is under predicted by the coupled model by around 40%.

8.2.2. Vibrations

In this section the aerodynamic response to blade vibrations is investigated for normal operation at 8 and 25 m/s. The corresponding rotor speeds are 9.2 rpm and 12.1 rpm and the pitch angles 0 degrees and 23.2 degrees, respectively. The load response to the prescribed vibration cases is compared in terms of radial distributions of aerodynamic work during one oscillation, where a positive aerodynamic work corresponds to a positive aerodynamic damping of the vibration. The mode shapes are chosen as the first and second structural mode shapes of the NREL 5 MW reference turbine blade at stand still, cf. Figure 17. To simplify the comparison, the vibrations have been prescribed either purely in-plane or out-of-plane for the edgewise and flapwise vibrations, respectively. The frequencies and amplitudes used for the computations are shown in Table I, as well as the modal masses that are used for damping estimations. The tip amplitudes used here have been limited to avoid stall.

The computationally expensive free wake model defines the time step of the prescribed motion simulations. A time resolution of 180 steps per rotor revolution (time step 0.036s for the 8m/s case and 0.028s for the 25m/s case) was used in the simulations of the first flap mode. This time step is affordable in terms of computational cost and provides a grid independent solution. The number of steps per period of the prescribed oscillation is 41-52 for the first flap mode which is sufficient to accurately integrate work over one cycle of oscillation. For the first edge mode the time step was decreased to 0.025s in order to ensure that the number of steps per period of oscillation will be equal to 40 (lower bound of the flapwise case). For the second flap and edge modes the time step was set to the lower limit of 0.01s, which corresponds to 55 steps per oscillation period for the second flap mode and to 31 steps per period for the second edge mode. Lower values of the time step would prohibitively increase computational time. Although the computational time of the coupled near and far wake model is not seriously affected by the time step the time step of the free wake simulations was employed in order to ensure uniformity in the work integration.

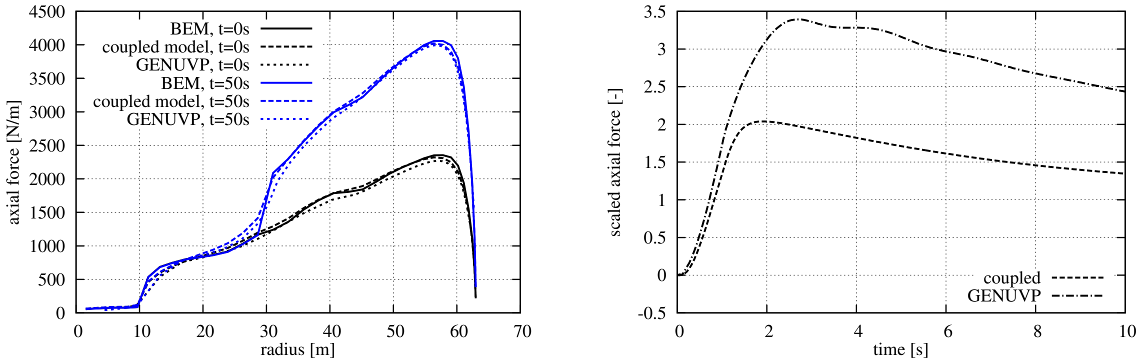

Figure 16. Left plot: Force distribution before the pitch step and 50 seconds after.
Right plot: Time history of the axial force comparing coupled model and GENUVP at 21.6 meter radius. The BEM gives a constant force.

Mode	freq. [Hz]	modal mass [kg]	amp. [m]	
first flap	0.66	905	0.25	0.5
first edge	1.0	1480	0.25	1.0
second flap	1.82	594	0.25	
second edge	3.2	793	0.25	

Table I. Modes, frequencies and amplitudes prescribed in the work comparison.

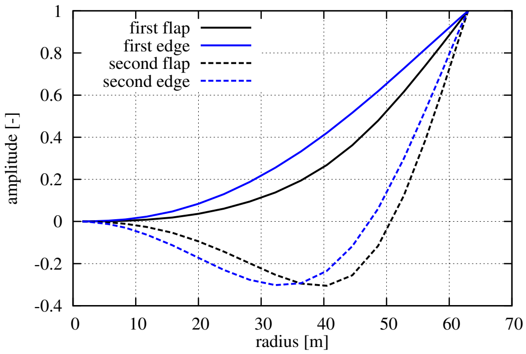

Figure 17. Mode shapes used in the work computations, which are simplified to be purely in-plane or out-of-plane deflections.

In the BEM and coupled model, the blade section velocities due to the vibrations are applied on the aerodynamic models as additions to the relative wind speed. The deflection of the blade and the resulting change of the section positions and the geometric parameter Φ of the NWM have been neglected because the amplitudes are small compared to the blade radius.

The aerodynamic work during out of plane motion according to the first flap mode shape is shown in Figure 18. The work integrated over the blade is over predicted by the BEM model by about 10% compared to the free wake code in all cases. The results of the coupled model are very close to the free wake code results. They slightly deviate towards higher work. This comparison indicates that the influence of the trailed vorticity behind the other two rotor blades, which is not included in the NWM, on the aerodynamic forces due to blade vibrations is small compared to the influence due to the wake of the blade itself in normal operation.

The comparison of the in-plane vibrations at 8 m/s is more challenging because the vibrations occur almost parallel to the inflow and the drag forces contribute much more to the work than in the other cases. To simplify the problem and to evaluate the modification of the unsteady aerodynamics model with regards to airfoil camber proposed in Section 4.2, drag has been excluded from the computations presented in the left plot of Figure 19. Further, the lift gradient has been assumed as 2π. If the airfoil camber is not considered in the computation of the effective angle of attack variation due to relative velocity variation, the agreement is poor, even in the simplified case. Adding the airfoil camber leads to a much improved result. In the right plot of Figure 19, the work computed using the coupled model shows a good agreement with the GENUVP results.

If drag is included and the airfoil polars of the NREL 5 MW reference turbine are used, the agreement between the codes is not as good in the 8 m/s case, as shown in the top plots of Figure 20. However, the differences in the unsteady drag prediction between the codes, which are based on the inviscid part of the Beddoes-Leishman type dynamic stall model in case of BEM and coupled model computations and the ONERA model for the free wake model are not the focus of this work. Even including the drag modeling the coupled model produces results much closer to the free wake code close to the blade tip than the BEM model. At 25 m/s, where the inflow angle is much larger and the work is predominantly due to the vibration component perpendicular to the inflow, the coupled near and far wake model is agreeing similarly well with the free wake code as in the cases with out-of-plane vibrations discussed above.

Figure 21 shows the comparison for the second in-plane and out-of-plane modes. The BEM model results compare similarly well with the GENUVP results as for the first modes. The coupled model results are closer to the free wake results than the BEM results in all cases, but as opposed to the comparisons above, the coupled model is underestimating the effects of the dynamics of the tip vortex. The addition of trailed vorticity reduces the aerodynamic work the BEM model predicts only very close to the tip in these cases, and in general the results of the coupled model are not as close to the free wake results as in the first mode comparisons. Further inboard the free wake code predicts slightly lower aerodynamic work in the 25 m/s case than the BEM model, which can't be seen in the coupled model results. Also the agreement of the coupled model and GENUVP is worse in the edgewise case than in the flapwise case at 25 m/s, which has not been seen to that extend for the first edgewise cases, cf. Figures 18 and 20. A reason for this might be that the second edgewise case is computed with fewer time steps per period of oscillation to limit the computational cost.

To easier evaluate the impact of the differences observed in this section on load computations and stability analysis, the aerodynamic work can be expressed in terms of a damping ratio of a respective blade mode. It is important to note that, because the computations have been based on prescribed mode shapes that were purely in-plane and out-of-plane and based on structural, not aeroelastic, analysis of the turbine blades, these logarithmic decrements are not corresponding to any aeroelastic blade modes. Further, the energy exchange between different aeroelastic modes is neglected in this estimation.

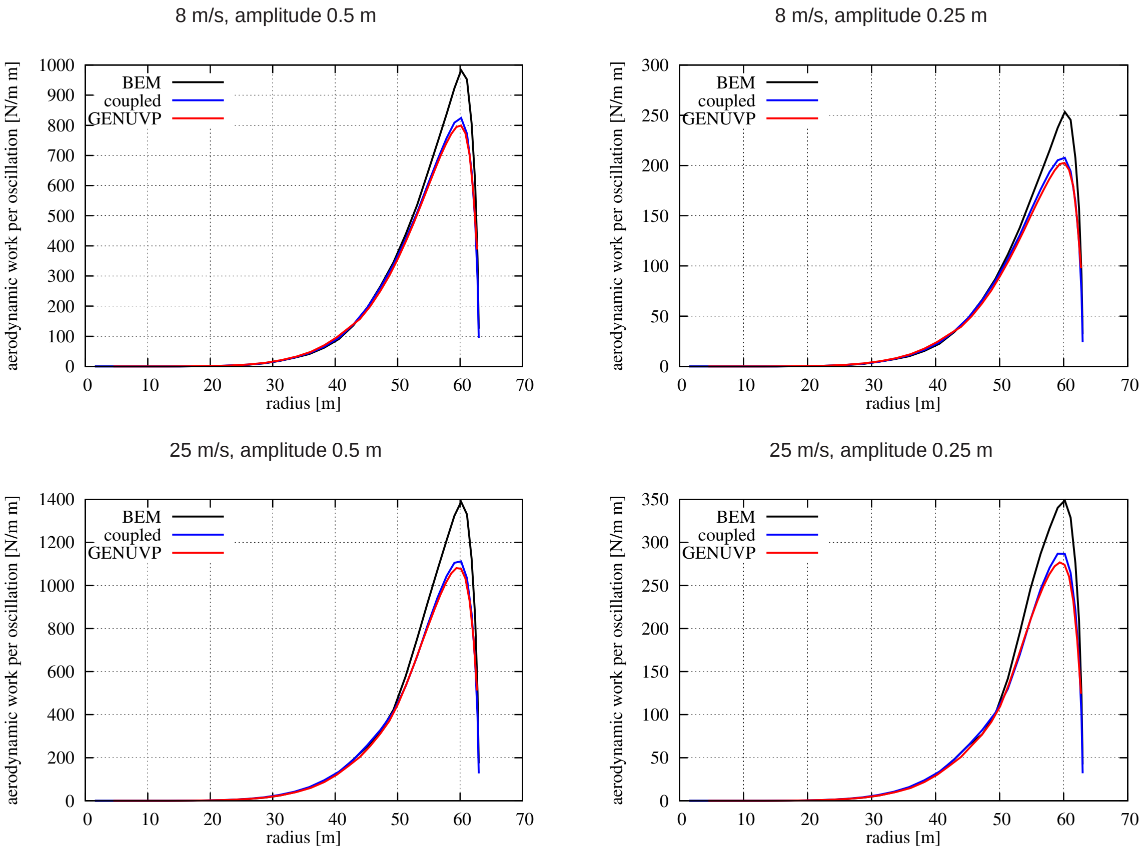

8 m/s, amplitude 0.5 m

8 m/s, amplitude 0.25 m

25 m/s, amplitude 0.5 m

25 m/s, amplitude 0.25 m

Figure 18. Comparison of aerodynamic work during one oscillation of first flap motion at 8 m/s and 25 m/s.

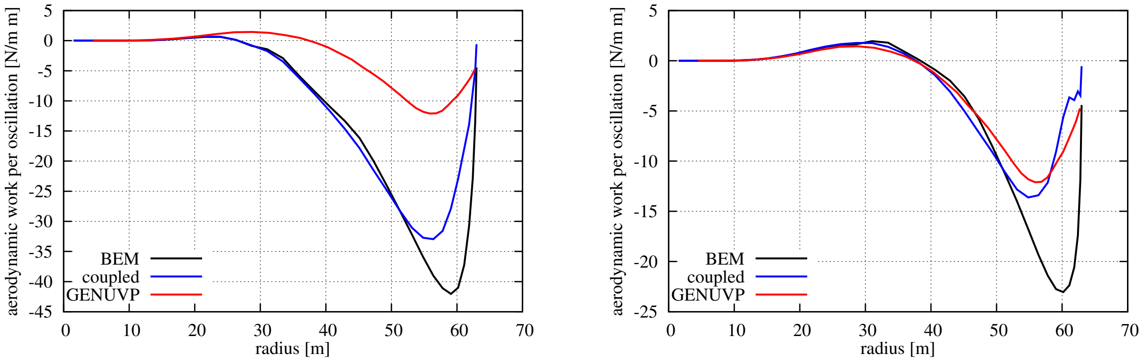

Figure 19. Comparison of aerodynamic work during one oscillation of first edge motion at 8 m/s at an amplitude of 1 m. Drag has been excluded, and the lift gradients of the airfoils are assumed to be 2 π. In the right plot, the camber of the airfoils has been treated as an increase of the mean angle of attack in the unsteady airfoil aerodynamics model used for coupled model and BEM, cf. Equation (25).

The estimated logarithmic decrements can, however, illustrate the order of magnitude of the effect of aerodynamic modeling on aerodynamic damping of flapwise and edgewise blade modes.

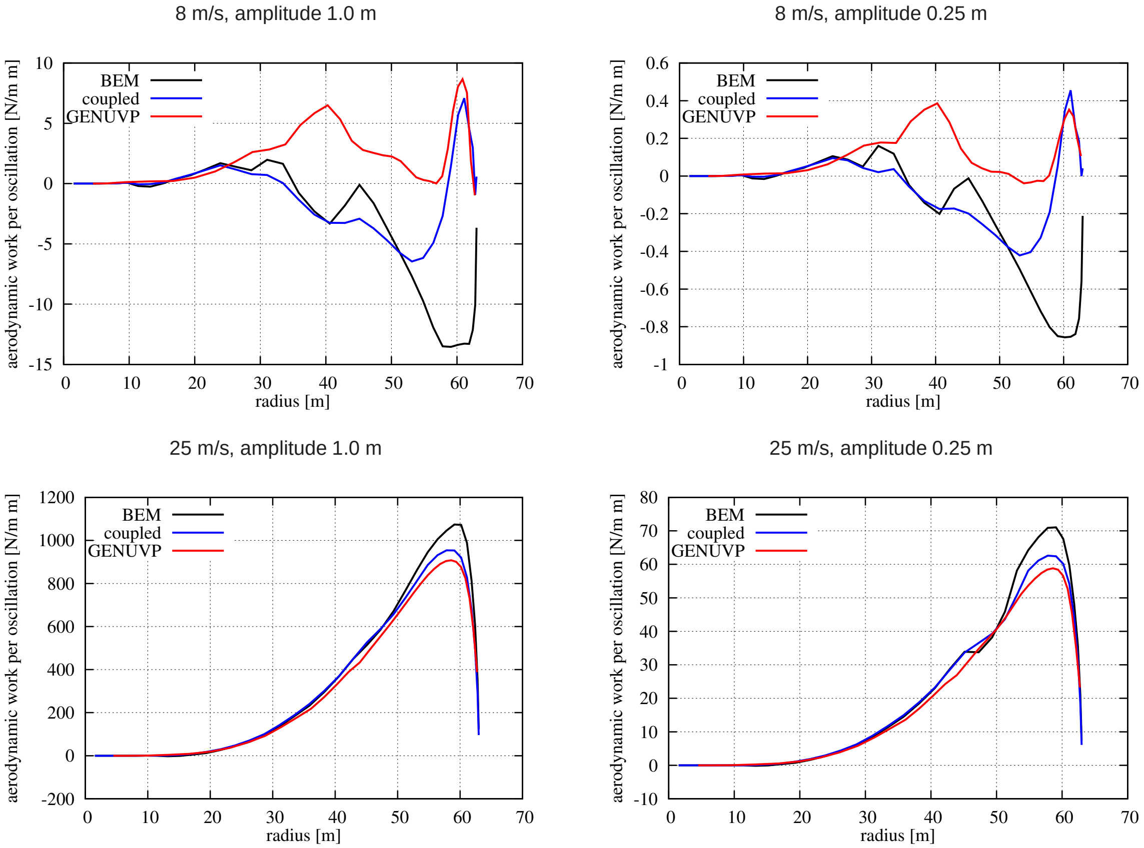
8 m/s, amplitude 1.0 m

8 m/s, amplitude 0.25 m

25 m/s, amplitude 1.0 m

25 m/s, amplitude 0.25 m

Figure 20. Comparison of aerodynamic work during one oscillation of first edge motion at 8 and 25 m/s.

Assuming a single degree of freedom system with the modal mass m and frequency f, given in Table I, the damping ratio ξ and logarithmic decrement δ can be expressed as:

$$\xi = \frac{W_{aero}}{8\pi^3 A^2 f^2 m} = \frac{1}{\sqrt{1+\left(\frac{2\pi}{\delta}\right)^2}} \qquad (41)$$

where A is the amplitude and W_{aero} the integral of the aerodynamic work over one oscillation period. The estimated logarithmic decrements according to Equation (41) corresponding to the first flap motion at 8 $\mathrm{m/s}$ with an amplitude of 0.5 m, cf. the top left plot of Figure 18, are 334 % for the BEM results, 300 % for the coupled model and 292 % for the free wake code results. The right plot of Figure 18 shows that all codes predict a reduction of the work by roughly a factor of 4 if the amplitude is halved, as expected according to Equation (41). Generally, these deviations of the logarithmic decrement are not important for the computation of blade loads because flapwise modes are highly damped and will thus not contribute significantly to fatigue loads. On the other hand, the lower aerodynamic damping of flapwise blade motion will correspond to a lower aerodynamic damping of tower fore-aft motion and might thus lead to increased tower fatigue loads. However, the lower aerodynamic damping could be balanced by a decreased excitation of the tower fore-aft modes, because the near wake effects are likely to reduce the aerodynamic force variations due to atmospheric turbulence in the same way as they reduce the aerodynamic work due to blade motion.

Edgewise modes tend to have very low aeroelastic damping, which makes an accurate damping computation important. The aerodynamic damping estimations for the in-plane vibrations at 8 $\mathrm{m/s}$ are shown in Table II. The damping has been estimated based on the computations with the first edgewise mode shape and an amplitude of 1 m in four different cases to separate the influence of the different parameters: Case (1) and (2) both use a lift gradient of 2π and zero drag. The difference between the first two cases is if the camber is included in the unsteady airfoil aerodynamics computations; they correspond to the left and right plot in Figure 19, respectively. Case (3) uses the lift coefficient according the NREL 5 MW airfoil polars, but drag is ignored. The corresponding radial aerodynamic work distribution plots are not included in the paper for brevity. Case (4) is based on both lift and drag coefficients of the NREL 5 MW reference turbine, where the

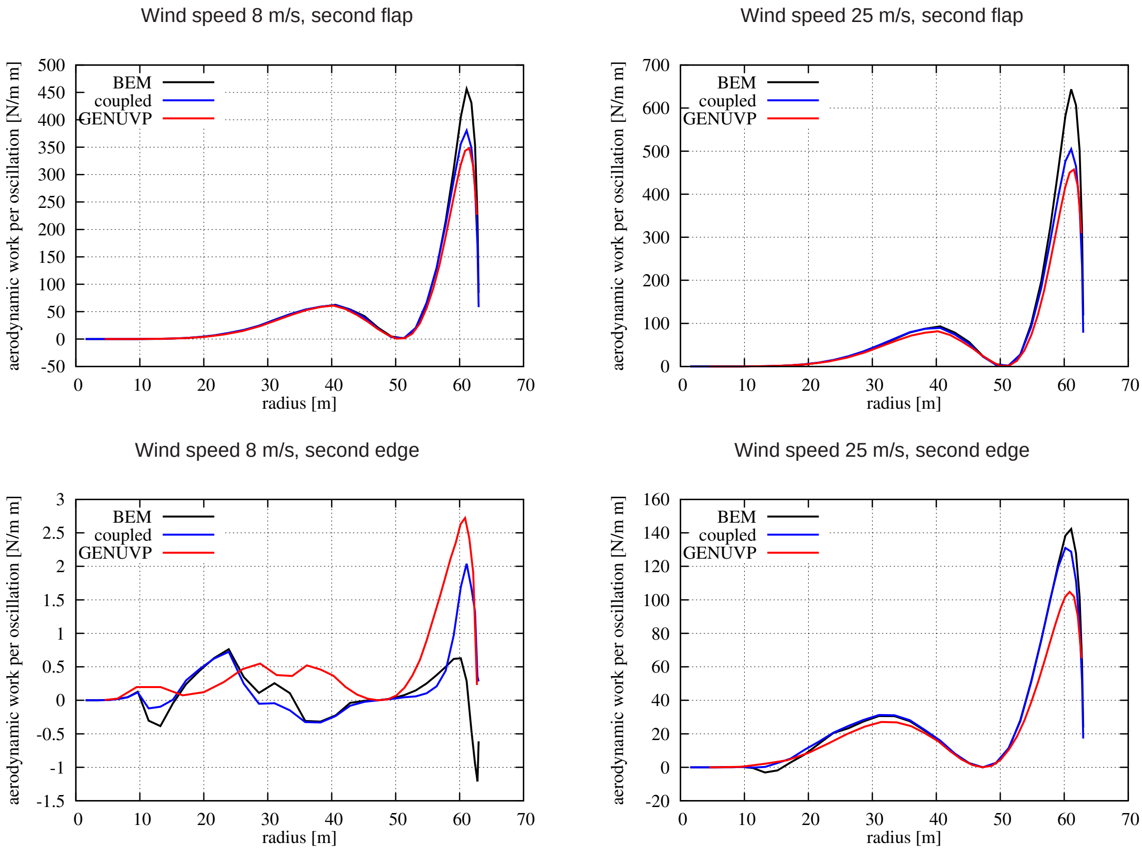

Figure 21. Comparison of aerodynamic work during one oscillation of second flap and edge motion at 0.25 m amplitude.

	$C'_L = 2\pi$, $C_D = 0$, no camber	$C'_L = 2\pi$, $C_D = 0$	NREL C_L, $C_D = 0$	NREL C_L and C_D
BEM	-1.13	-0.41	-0.52	-0.24
Coupled model	-1.00	-0.27	-0.37	-0.1
GENUVP	-	-0.25	-	0.22

Table II. Estimated logarithmic decrements [%] corresponding to the aerodynamic work of first in-plane vibrations at 8 m/s. The estimates are based on vibrations with an amplitude of 1 m. The values do not correspond to the damping of any aeroelastic mode, but are provided to evaluate the impact of the different aerodynamic models.

work distributions have been shown in Figure 20. Comparison of the first two cases of Table II shows that the induced drag caused by airfoil camber in the shed vorticity modeling is resulting in an aerodynamic damping of roughly 0.7 % logarithmic decrement. According to the BEM and coupled model results in case (3) and (4) the airfoil drag causes an estimated difference in logarithmic damping of about 0.3 % in this case with purely in-plane vibrations. The trailed vorticity consistently decreases the absolute value of the estimated logarithmic damping by roughly 0.14 %. Further, comparing columns (2) and (4), the combined influence of airfoil polars with lift coefficients other than 2π and drag is close to three times larger in the free wake code computations, which is caused by the different unsteady drag modeling. Although the differences in estimated logarithmic decrement are generally small, they might have an impact on loads computations for edgewise modes with an aeroelastic damping that is close to zero.

In the out-of-plane prescribed vibration cases investigated, the addition of the NWM leads to a reduction of the aerodynamic work. Further a previous study by Pirrung et al. [6] showed that the trailed vorticity effects will delay the onset of flutter towards higher rotor speeds. This is in agreement with findings on the influence of shed vorticity, which leads to both a decrease of the flapwise damping and increased flutter speeds of a vibrating 2D blade section [18].

9. CONCLUSIONS

In this paper, several modifications of a coupled model consisting of a trailed vorticity model for the near wake and a BEM-based model for the far wake have been presented and validated. Results from the coupled model are compared to free wake panel code and a BEM model to evaluate the benefits and limitations of the added trailed vorticity modeling.

It has been shown that the acceleration of the model by reducing the number of exponential functions in the trailing wake approximation from two to one is possible with negligible effect on the results. The approach presented here does not change the steady results predicted by the NWM.

An iteration scheme to stabilize the model has been presented. It applies a relaxation factor that is computed dynamically based on the blade discretization and the operating point of the turbine. To evaluate the computed relaxation factors, minimum necessary relaxation factors have been determined by trial-and-error and the estimated factors are found to be conservative. The iterative process enables stable computations without the need for very small time steps and reduces oscillations of the near wake induction.

The 2D shed vorticity modeling, based on thin airfoil theory, has been extended by including the unsteady effects on the bound circulation. Further it has been found that it is necessary to include airfoil camber in the modeling of the influence of varying inflow velocity on the dynamic angle of attack to obtain good results if the direction of vibration is close to parallel to the inflow direction.

A comparison of pitch step responses of the NREL 5 MW reference turbine using the coupled near and far wake model, a BEM model based on the aerodynamics model in HAWC2 and the free wake panel code GENUVP has been presented. The trailed vorticity modeling in the coupled model gives results closer to the free wake code than the BEM model during the pitching motion, and for a slow pitching rate a clear improvement is seen in the computation of the overshoot. Fast pitch rates resulted in oscillations due to the motion of the wake in the free wake code, which could not be achieved in the coupled model due to the prescribed wake assumption.

The coupled model agreed better than the BEM model with the free wake code in all prescribed vibration cases investigated. The main improvement due to the trailed vorticity is found close to the tip of the blade, even in case of the higher modes investigated. The work response to the edgewise vibrations has been found to be difficult to model if the direction of vibration is close to parallel to the inflow direction. The results in this case compare much better if no drag forces are computed. If drag is included, the coupled model still compares well with the free wake code close to the blade tip, but there are larger deviations in the results of all models further inboard. In general, the simulations agreed better for out-of-plane vibrations than in-plane vibrations.

The implementation of the coupled near and far wake model presented here delivers promising results and will be further investigated and validated against computational fluid dynamics results and measurements in future work. In particular the more accurate prediction of aerodynamic work for edgewise vibrations is considered to be important for stability analyses and load predictions due to the low aeroelastic damping typically associated with these vibrations.

REFERENCES

1. Beddoes TS. A near wake dynamic model. *proc. of the AHS national specialist meeting on aerodynamics and aeroacoustics* 1987; .
2. Madsen HA, Rasmussen F. A near wake model for trailing vorticity compared with the blade element momentum theory. *Wind Energy* 2004; **7**:325–341.
3. Andersen PB. *Advanced Load Alleviation for Wind Turbines using Adaptive Trailing Edge Flaps: Sensoring and Control*.
4. Pirrung GR, Hansen MH, Madsen HA. *Improvement of a near wake model for trailing vorticity*, Proceedings of the science of making torque from wind, Oldenburg, 2012.
5. Jonkman J, Butterfield S, Musial W, Scott G. Definition of a 5-mw reference wind turbine for offshore system development. *Technical Report*, National Renewable Energy Laboratory 2009.
6. Pirrung GR, Madsen HA, Kim T. The influence of trailed vorticity on flutter speed estimations. *Journal of Physics: Conference Series (Online)* 2014; **524**, doi:10.1088/1742-6596/524/1/012048.
7. Larsen TJ, Hansen AM. *How 2 HAWC2, the user's manual*. Denmark. Forskningscenter Risoe. Risoe-R-1597, 2007.
8. Larsen TJ, Madsen HA, Larsen GC, Hansen KS. Validation of the dynamic wake meander model for loads and power production in the egmond aan zee wind farm. *Wind Energy* 2013; **16**(4):605–624, doi:10.1002/we.1563.
9. Kim T, Hansen AM, Branner K. Development of an anisotropic beam finite element for composite wind turbine blades in multibody system. *Renewable Energy* 2013; **59**:172.
10. Voutsinas SG. Vortex methods in aeronautics: How to make things work. *International Journal of Computational Fluid Dynamics* 2006; **20**:3–18.

11. Wang T, Coton FN. A high resolution tower shadow model for downwind wind turbines. *Journal of Wind Engineering and Industrial Aerodynamics* 2001; **89**:873–892.
12. Pirrung GR, Madsen HA, Kim T, Heinz J. *A Coupled Near and Far Wake Model for Wind Turbine Aerodynamics*. submitted, 2014.
13. Sørensen NN, Madsen HA. *Modelling of transient wind turbine loads during pitch motion*. European Wind Energy Association (EWEA), 2006.
14. Hansen MH, Gaunaa M, Madsen HA. *A Beddoes-Leishman type dynamic stall model in state-space and indicial formulations*. Risø-R-1354: Roskilde, Denmark, 2004.
15. Madsen HA, Gaunaa M. *Udvikling af model for 3D induktions- og stallmodellering*. Risø-R-1509(DA): Roskilde, Denmark, 2004.
16. Petot D. Differential equation modeling of dynamic stall. *La Recherche Aerospatiale(English Edition)* 1989; (5):59–72.
17. Riziotis VA, Voutsinas SG. *Dynamic Stall on Wind Turbine Rotors: Comparative Evaluation Study of Different Models*, Proceedings of the 1997 European Wind Energy Conference and Exhibition, 1997.
18. Hansen MH. Aeroelastic instability problems for wind turbines. *Wind Energy* 2007; **10**:551–577.

DOI: 10.1002/we
Prepared using weauth.cls

[IV]

The influence of trailed vorticity on flutter speed estimations

The influence of trailed vorticity on flutter speed estimations

Georg R. Pirrung, Helge Aa. Madsen and Taeseong Kim
DTU Wind Energy, Frederiksborgvej 399, Roskilde, DK
E-mail: `gepir@dtu.dk`

Abstract. This paper briefly describes the implementation of a coupled near and far wake model for wind turbine rotor induction in the aeroelastic code HAWC2 and its application for flutter analysis of the NREL 5 MW wind turbine. The model consists of a far wake part based on Blade Element Momentum (BEM) theory, which is coupled with Beddoes' near wake model for trailed vorticity.

The first part of this work outlines the implementation in HAWC2, with a focus on the interaction of the induction from the blade based near wake model with the induction from the polar grid based BEM model in HAWC2.

The influence of the near wake model on the aeroelastic stability of the blades of the NREL 5 MW turbine in overspeed conditions is investigated in the second part of the paper. The analysis is based on a runaway case in which the turbine is free to speed up without generator torque and vibrations start building up at a critical rotor speed. Blades with modified torsional and flapwise stiffness are also investigated. A flutter analysis is often part of the stability investigations for new blades but is normally carried out with engineering models that do not include the influence of unsteady trailed vorticity. Including this influence results in a slightly increased safety margin against classical flutter in all simulated cases.

1. Introduction

Most of the aeroelastic codes used in the wind turbine industry are based on Blade Element Momentum (BEM) theory to model the induced wind speeds due to the aerodynamic forces at the rotor disc, cf. [1]. The trailed vorticity, which depends on the radial gradient of the bound circulation along the blade, is in these codes only implicitly included for the tip vortex in form of a tip loss correction, but the dynamic effects of the trailed vorticity are neglected. Hansen [2] names these near wake effects as one of the state-of-the-art issues in predicting flutter limits for wind turbines. In this paper the influence of these effects on the critical rotor speeds, the rotor speeds where blade vibrations with negative damping start to build up, is investigated for the NREL 5MW reference turbine [3].

Flutter instabilities for large turbines have been investigated by for example Hansen [2, 4] and Lobitz [5, 6]. Both found that including the unsteady shed vorticity effects in the aerodynamic models led to increased flutter speeds and that the rotor speeds in normal operation are closer to critical rotor speeds for modern turbines with larger, more flexible blades than for small turbines. Thus a more accurate prediction of flutter speeds might become more important for future turbines.

This study uses the aeroelastic wind turbine code HAWC2 [7, 8, 9], in which a polar grid based

BEM model enables azimuth dependent induction, such as in sheared inflow [10]. To this BEM model a near wake model developed by Beddoes [11] and suggested for wind turbine application by Madsen and Rasmussen [12], has been added. The near wake model is a numerically efficient prescribed wake lifting line model, which allows for trailed vorticity computation without drastically slowing down the aeroelastic code. The motivation for the trailed vorticity modelling is to obtain a more precise dynamic induction prediction compared to a purely BEM based model and to remove the need for an additional tip loss correction. The dynamic induction due to the shed vorticity is modelled by the Beddoes Leishman dynamic stall model [13] in HAWC2, which includes the unsteady effects in the linear lift slope region. The near wake model needs to be stabilized in an iterative procedure and the possibility of accelerating the model by taking less important parts of the model out of the iteration loop is shown in this work.

The critical rotation speeds are obtained by simulating runaway cases, where the turbine is operating without generator torque and at a fixed pitch angle of zero. The rotor is thus free to speed up and the rotor speed can be controlled by the wind speed. To approach a critical rotor speed, the wind speed is accelerated following a slow ramp. The influence of the wind speed gradient in that ramp is briefly investigated in this paper. The structural stiffnesses of the NREL 5MW blade regarding both flapwise bending and torsion are modified to show the influence of the near wake model for different blades.

The next section gives a brief description of the grid-based BEM HAWC2 model, followed by the implementation of the near wake model. Then the runaway cases and a simple method to approximate the mode shapes of the unstable vibrations in HAWC2 is explained. Finally, critical flutter speeds comparing the original HAWC2 model with the extended HAWC2 model including the near wake model, in the following denoted as HAWC2 NW, are presented.

2. Implementation of a near wake model in the aeroelastic code HAWC2

2.1. BEM in HAWC2

The classic BEM method divides the rotor disc into annular elements, where the quasi steady induction is calculated based on the local thrust at each radial section. To enable different inductions at different parts of the rotor disc, e.g. top and bottom in case of wind shear, the annular elements are in HAWC2 divided by azimuthal sections, leading to a non-rotating polar grid. Two first order filters with time constants depending on the loading and the radial position are applied on the quasi steady induction at each grid point to include the dynamic inflow effect. The grid-based computation of the induction is described by Madsen et al. in [10].

The induction and free wind speed, stored on the polar grid, are needed to compute the flow and resulting forces at the blades and the blade velocity and pitch angle are needed to compute the thrust coefficient on the grid. Azimuthal interpolation is therefore necessary both from the closest grid points to the blade and from the closest blades to the grid point.

2.2. Implementation of the near wake model in the HAWC2 aerodynamic model

The near wake model is used to compute the induction due to the trailed vorticity in a quarter rotation behind the blades. Vorticity is trailed from vortex trailing points at the root and tip of the blade, as well as between the aerodynamic sections that are used to compute the local forces on the blade. Each blade is only influenced by induction due to its own trailed vorticity.

In principle, the induction at each radial position on the blade would be computed as the result of a numerical integral of the Biot-Savart law over the trailed vortex elements, each at the length of one time step, behind the blade. Beddoes, [11], proposed to approximate the decreasing induction due to a vortex element as it moves away from the blade by two exponential functions. This approximation makes it possible to increase the computation speed, because the influence of all previously trailed elements decreases by the same factor in a time step. To obtain the induction in a following timestep, it is therefore sufficient to multiply the total induction of all previously trailed elements by this factor and add the contribution from the newest element trailed in the time step.

In the original form, the near wake model assumed the trailed vorticity to stay in the rotor plane, but in this paper a correction for downwind convection is included in the model. With this correction the vorticity moves along helical paths, where the pitch angle of the helix depends on the local flow at the respective radial blade section.

Because the near wake model gives the induction at the blade position due to the vorticity trailed from the respective blade, the induced velocity from the near wake is in HAWC2 treated in the same way as blade velocity and pitch angle, that is as a local blade parameter. This means that the total induction is consisting of one part that is computed in the fixed polar grid, the far wake induction, and one part that is rotating with the blades, the near wake induction. To obtain the far wake induction, the BEM induction is scaled by a coupling factor that is smaller than one. The coupling factor is determined so that the integral thrust force of HAWC2 NW matches the HAWC2 BEM model with tip loss correction. The near wake model needs to be iterated to ensure a stable operation. One call of the aerodynamic model HAWC2 NW is structured as follows:

(i) BEM induction
  (a) Find the two closest blades to each grid point
  (b) Calculate thrust coefficient using blade velocity, pitch angles and near wake induction of each of the two closest blades
  (c) Interpolate thrust coefficient at the grid point based on azimuth angle
  (d) Calculate far wake induction

(ii) Near wake induction
  (a) Find closest grid points to each blade section
  (b) Interpolate far wake induction and wind speed
  (c) Iterate until convergence:
    1. Compute angles of attack and relative velocity
    2. Compute length and helix pitch angle of trailed vorticity
    3. Compute quasi-steady circulation at each blade section
    4. Apply time lags to account for dynamic circulation buildup
    5. Compute induction from trailed vorticity in the near wake
    6. Apply relaxation factor on near wake induction

(iii) Calculate dynamic lift, drag and moment coefficients, using the dynamic stall model in [13]. These coefficients do not feed back back to the BEM induction, but are used to determine the forces on the structure.

3. Flutter speed prediction scheme

In this section, the flutter speed prediction scheme used in this work is described, together with the method used to extract the mode shapes of negatively damped vibrations from HAWC2 simulations.

3.1. Run away case

To find a critical speed at which an aeroelastic turbine mode becomes negatively damped, the turbine has been simulated in a runaway situation, where the generator torque and pitch angle are zero. The rotor will in this case approach a rotation speed where the aerodynamic torque is zero, due to negative torque from the outer part of the blade and positive torque from the in board sections. This terminal rotor speed depends only on the wind speed at the rotor. To approach the critical rotor speed where an instability occurs the wind speed can be slowly ramped up, thus continuously increasing the rotor speed until vibrations of the blades start to build up, cf. Figure 1. In general there is no disturbance other than numerical errors to start the vibration. In Section 4.1 the influence of turbulence as additional excitation on the flutter speed is evaluated.

Advantages of this approach compared to for example prescribing an increasing rotor speed through the generator torque at a fixed wind speed are:

- The runaway case is a better approximation of an overspeed situation because no artificial forcing is necessary.
- The edgewise blade deflections are small because the rotor torque is close to zero. Edgewise deflection will change the coupling between flapwise, edgewise and torsional blade modes and change the flutter speed, in the same way as sweeping the blades would [14].
- The influence of the wind speed slope, which is the only relevant parameter for the simulation, is small, cf. Results section.

In all observed cases, the instability will, since the rotor speed is free to change, first lead to small oscillations of the rotor speed and then to a significant decrease of the rotor speed, as energy from the rotation is transferred to vibrations of the blades. In the following flutter speed comparisons, the flutter speed has been determined at the time where the rotation speed in one time step is smaller than in the previous time step for the first time in the simulation except the transients at the start up, cf. Figure 2.

3.2. Mode shape extraction

To compare the unstable blade vibrations obtained in the HAWC2, a simple routine has been developed. It requires output of the time series of edgewise and flapwise deflection as well as torsion along the blade. The algorithm fits a cosine function, $g = a\cos(ft - \phi)$, with the variables amplitude a, frequency f and phase ϕ, to a short, moving window of 0.5 seconds of the time series of the flapwise tip deflection, minimizing the error of the cosine fit with the original time series data. When a flapwise amplitude of $a = 0.1m$ is found in a time window, the algorithm extracts the mode shape by fitting cosine functions to deflections and rotations at all available radial stations of the blade. The amplitude of $0.1m$ was chosen because it proved to be a good compromise between extracting the small vibrations at the start of the instability and having large enough amplitudes along the blade to ensure a good performance of the curve fitting algorithm. In this way, the radial distributions of both amplitudes and phases of the

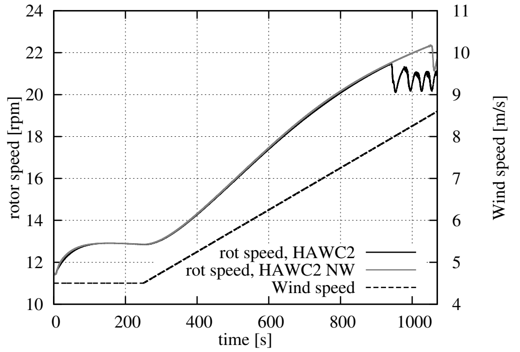

Figure 1. Principle of the runaway case: the wind speed is slowly ramped up and the rotor speed follows up to an instability. Comparison between HAWC2 with BEM and coupled near and far wake model.

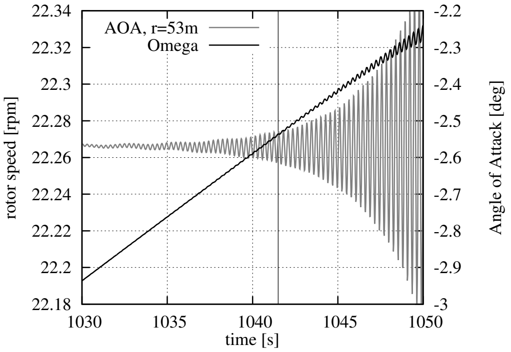

Figure 2. Zoom to the onset of vibrations. The black vertical line indicates the time interpreted here as the onset of flutter.

components of the blade vibration can be determined, leading to something similar to a mode shape. Because HAWC2 is able to capture the structural nonlinearities due to large deflections, the deflection shapes will vary with amplitude, so they are not equivalent to mode shapes in linear vibration theory. Still, they can be used to qualitatively compare the different instabilities obtained with the HAWC2 and HAWC2 NW models.

4. Results

In this section, flutter speeds of the NREL 5 MW turbine [3] and modified versions with stiffer and softer blades computed with HAWC2 and HAWC2 NW are compared. In all simulations the twist and cone of the turbine has been set to zero and there is no wind shear, yaw error and gravity. In the last part of the section the mode shapes of some of the observed vibrations are compared to obtain further insight in the effects of the trailed vorticity.

4.1. Sensitivity to ramping speed and disturbance

Figure 3 shows the sensitivity of the Flutter speeds predicted using the HAWC2 and HAWC2 NW models to changes in ramping speed. It can be seen that over the range of ramping speeds the flutter speeds are changing only slightly, by about 3% if the near wake model is included and 5% if the traditional HAWC2 BEM model is used. Note that this small change in flutter speed is a consequence of changing the ramping speed by a factor of 16 from 0.00125 m/s^2 to 0.02 m/s^2. The predicted flutter speeds are higher for faster ramping speed, which might be partially because the instabilities need some time to build up. At faster ramping speeds the rotor accelerates faster, leading to a bigger increase in rotor speed between the first small blade oscillations and a decrease in rotor speed that is used here to mark the onset of the instability. Because the difference between HAWC2 and HAWC2 NW results is similar for different ramping speeds and slow ramps require long computations, all further computations have been performed using a wind ramp with a slope of 0.005 m/s^2.

In Figure 4 the influence of added turbulence is shown for low turbulence intensities. Turbulence decreases the flutter speed when the original HAWC2 model is used, but has almost no influence in case of the near wake model. In Section 4.3 it is shown that the reason for this difference is that two different modes can become unstable in HAWC2 at slightly different relative speeds if the standard blade is used. It seems that the mode that becomes unstable at lower wind speeds, which is different than the mode observed in HAWC2 NW, cf. Section 4.3, is more affected by turbulence than the other mode. Even though there is a clear influence of turbulence intensity on the offset between the flutter speeds predicted by the near wake model and the original HAWC2 model in this particular case, it has been decided to run all following computations without turbulence to avoid introducing an additional parameter.

4.2. Sensitivity to structural stiffness variations of the blade

Figure 5 shows the influence of the variation of both flapwise stiffness and torsional stiffness on the flutter speed. The cross section parameters Ix, the flapwise area moment of inertia, and Ip the torsional stiffness constant, have been artificially varied from 70 to 130 % of the original values for the NREL 5 MW turbine, keeping all other parameters constant. Both models agree that an increase of torsional blade stiffness leads to an increased stability, as expected. The flutter speed increase due to increased torsional stiffness is comparable in both models.

The flapwise stiffness variation, however, leads to different results. In agreement with findings by Lobitz [6], the flapwise stiffness has a smaller influence on the flutter speed than the torsional stiffness. In the present work, the direction in which an increasing flapwise stiffness changes the flutter speed is found to depend on both the blade and the used aerodynamic model: For the blade with 130% torsional stiffness, both aerodynamics models agree on a reduced flutter speed for increasing the flapwise stiffness from 100% to 130%. The most interesting behavior can

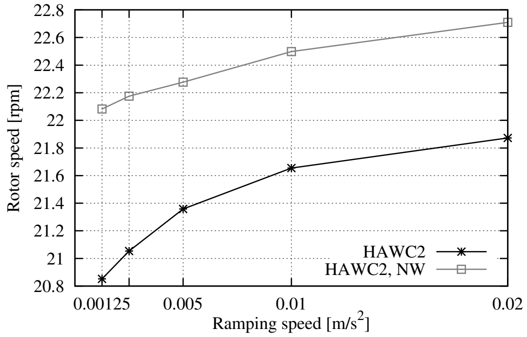

Figure 3. Sensitivity of flutter speed with respect to ramping speed.

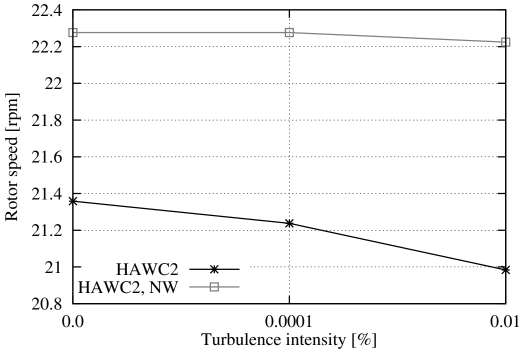

Figure 4. Sensitivity of flutter speed with respect to turbulence intensity.

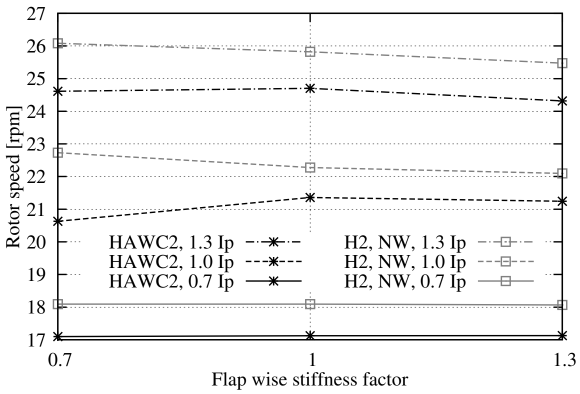

Figure 5. Sensitivity of flutter speed with respect to torsional and flapwise stiffness variations.

be seen when the flapwise stiffness is decreased from 100% to 70% for the otherwise unaltered blade. In this case the HAWC2 predicts a decrease in flutter speed, while HAWC2 NW shows an increased flutter speed. This case is further investigated in the next section based on the mode shapes of the vibrations simulated in HAWC2.

4.3. Vibration modes

The amplitudes and phases of deflections, axial induced velocity and aerodynamic forces of the blade vibrations are shown in Figures 6 and 7 for the cases with 70% and 130% flapwise stiffness and standard torsional stiffness. All amplitudes are normed by the flapwise tip amplitude and the plots show the mode shapes at a flapwise tip amplitude of 0.1 m. The phases are relative to the phase of the flapwise tip vibrations.

It can be seen that the vibrations of the softer blade, cf. Figure 6, agree well in the flapwise and torsional contents, but the HAWC2 computation predicts a much larger edgewise amplitude. In fact, the blade vibrates in different modes depending on the aerodynamic model; HAWC2 predicts a backward whirling mode with blade vibrations at 2.8 Hz, HAWC2 NW a symmetric flutter mode at 3.6 Hz. The frequency difference explains the different amplitudes of the aerodynamic forces, where HAWC2 NW predicts larger amplitudes even though the induction is responding much faster according to the near wake model.

In case of the stiffer blade, cf. Figure 7, both aerodynamic models predict the same unstable mode, a symmetric flutter mode at a frequency of 3.7 Hz. Magnitudes and phases of deflections and forces agree well between HAWC2 and HAWC2 NW, but the induced velocity is again

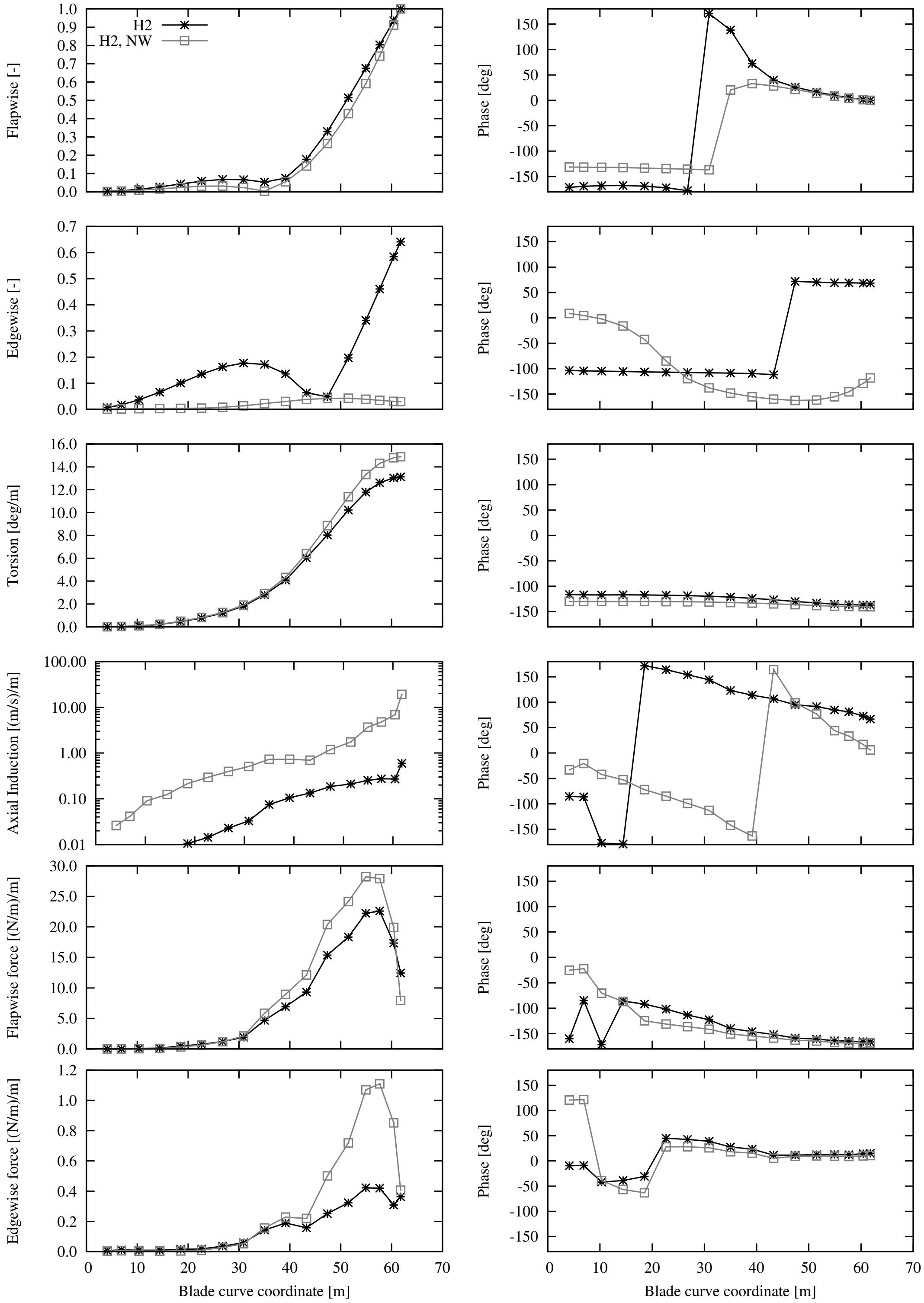

Figure 6. Comparison of unstable mode shapes of the turbine with blades at 70% stiffness, including the amplitudes and phases of induced velocity and aerodynamic forces. Different modes become unstable. The original HAWC2 model shows a backward whirling mode at a blade frequency of 2.8 Hz, the HAWC2 NW model a symmetric mode at 3.6 Hz.

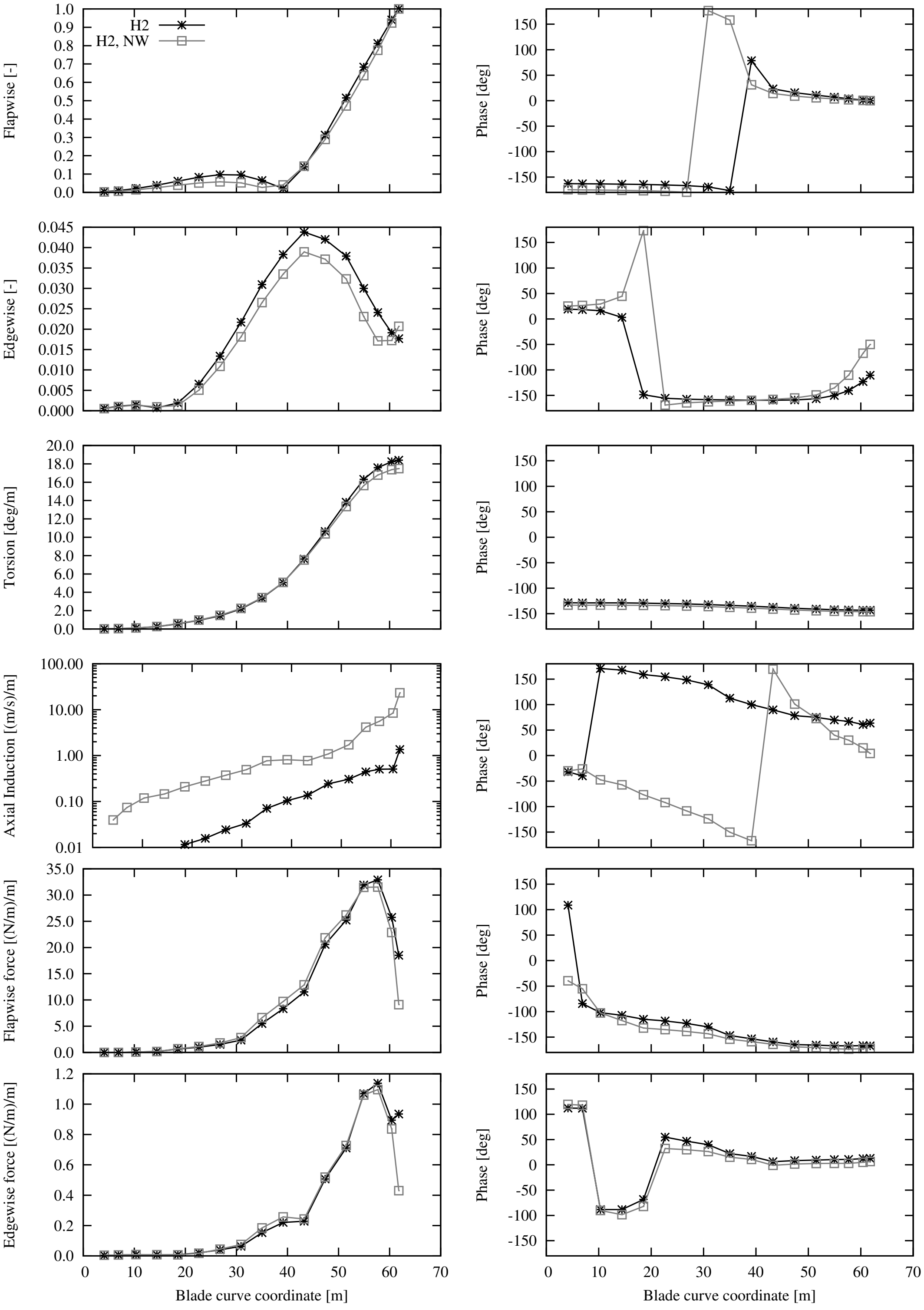

Figure 7. Comparison of unstable mode shapes of the turbine with blades at 70% stiffness, including the amplitudes and phases of induced velocity and aerodynamic forces. HAWC2 and HAWC2 NW agree on a symmetric mode with a very small edgewise component, at a frequency of 3.7 Hz. The large difference in induced velocity only has a small impact on the mode shape and the amplitudes and phases of aerodynamic forces.

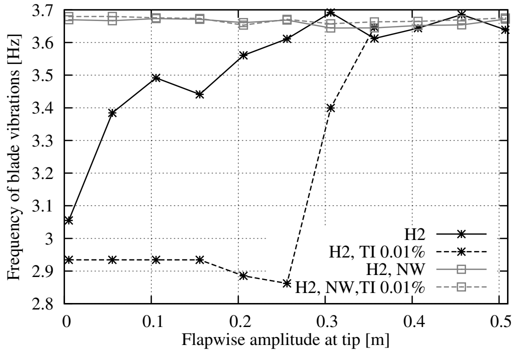

Figure 8. A shift of frequency can be observed on the standard NREL 5MW blade with the original HAWC2 aerodynamic model as the vibrations build up. Turbulence has a larger influence if the HAWC2 aerodynamic model is used.

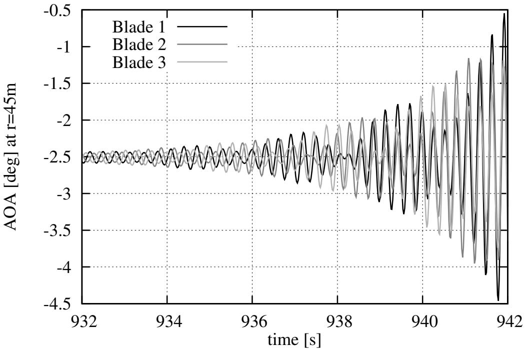

Figure 9. Time series of the AOA on the blades in the undisturbed case. At the onset of vibration, there is a 120 degree phase shift between blades, indicating a whirling mode. At small amplitudes, the vibrations start to synchronize.

computed with a larger amplitude by the near wake model.

The standard NREL 5MW blade with 100% flapwise and torsional stiffness exhibits an interesting behavior: if the original HAWC2 model is used, the frequency shifts from roughly 3.05 Hz at a very low flapwise amplitude of 5 mm to 3.65 Hz as the amplitude is increasing in the undisturbed case, cf. Figure 8. If turbulence is added to the HAWC2 computation, the vibrations start at lower rotation speed, cf. Figure 4, and stay at the low frequency also at higher amplitudes. An explanation for this behavior is that the whirling mode at the lower frequency might have a negative aeroelastic damping closer to zero than the symmetric mode. If that is the case, disturbance has a larger effect on the vibration buildup in the whirling mode because vibrations in the symmetric mode are growing faster starting from the very small numerical disturbance that is present in all the simulations.

Figure 9 shows in the time domain how the vibrations of the three different blades start out with a phase shift and synchronize during a short time in the undisturbed case. A comparison of the mode shapes predicted by HAWC2 and HAWC2 NW at small amplitude leads to a similar result as for the softer blade, cf. Figure 6, and at higher amplitudes the comparison is similar to the stiffer blade, cf. Figure 7, but the respective plots are not included in this paper for brevity.

A possible explanation for these findings is: the NREL 5 MW turbine can vibrate in overspeed in two modes with similar flapwise and torsional content, both in amplitude and phase. Depending on the aerodynamic model and the flapwise stiffness, either a backward whirling mode or a symmetric mode has a lower critical speed where the aeroelastic damping becomes negative. The trailed vorticity increases the critical speed of the whirling mode more than the critical speed of the symmetric mode, so that vibrations in the whirling mode are not observed in HAWC2 NW. In HAWC2, the whirling mode becomes unstable at lower rotation speed than the symmetric mode in case of the blade with reduced flapwise stiffness. This softer blade vibrates consistently in different modes depending on the aerodynamic model, which explains the larger difference in flutter speeds.

In case of the standard blade, the whirling mode seems to be unstable only at a small range of rotation speed and the observed vibrations quickly shift to the symmetric mode as the rotor accelerates. The stiffer blade vibrates in the same mode shape in the HAWC2 and HAWC2 NW computations, which may be a reason for the smaller difference in flutter speed predictions. This might only be a partial explanation of the observed phenomena, and further investigations are necessary for a more complete understanding.

5. Conclusions

The near wake model, originally developed by Beddoes, is implemented in the aeroelastic wind turbine code HAWC2. It is used to investigate the influence of trailed vorticity on the critical rotor speeds of the NREL 5 MW reference turbine with the original and modified blades, respectively. The critical rotor speeds are found by means of runaway cases, where the rotor is free to speed up at zero pitch angle and no generator torque.

It is shown that the critical rotor speed is almost independent of the slope of the wind speed ramp in the runaway cases. Including the trailed vorticity in the HAWC2 aerodynamic model has only slowed down the computation speed by a few percent. HAWC2 shows some dependence of the flutter speed on inflow turbulence, which can not be seen if the near wake model is used in the calculations.

The models agree that a torsional stiffness increase leads to an increase in flutter speeds. The influence of flapwise stiffness variations is smaller and less consistent. In some cases, the models disagree if an increased flapwise stiffness has a stabilizing or destabilizing effect.

More detailed investigations have shown that two different full turbine modes can be critical if the original torsional stiffness of the blade is used: a backward whirling mode and a symmetric mode. In near wake model computations only the symmetric mode can be observed. In case of the original HAWC2 model which of the two modes is critical depends on the flapwise blade stiffness. Further research is needed to understand in detail how the trailed vorticity stabilizes both modes.

In all cases investigated, the trailed vorticity in the near wake has a stabilizing effect and increases the flutter limit by roughly four to ten percent.

References

[1] Madsen H A, Riziotis V, Zahle F, Hansen M O L, Snel H, Grasso F, Larsen T J, Politis E and Rasmussen F 2012 Blade element momentum modeling of inflow with shear in comparison with advanced model results *Wind Energy* **15** 63–81

[2] Hansen M H 2007 Aeroelastic instability problems for wind turbines *Wind Energy* **10** 551–577

[3] Jonkman J, Butterfield S, Musial W and Scott G 2009 Definition of a 5-mw reference wind turbine for offshore system development Tech. rep. National Renewable Energy Laboratory

[4] Hansen M H and Madsen H A 2000 *Analyse af risikoen for flutter på vindmøllevinger* Denmark. Forskningscenter Risoe. Risoe-R-1196

[5] Lobitz D W 2004 Aeroelastic stability predictions for a MW-sized blade *Wind Energy* **7** 211–224

[6] Lobitz D W 2005 Parameter sensitivities affecting the flutter speed of a MW-sized blade *Journal of Solar Energy Engineering, Transactions of the ASME* **127** 538–543

[7] Larsen T and Hansen A 2007 *How 2 HAWC2, the user's manual* Denmark. Forskningscenter Risoe. Risoe-R-1597 ISBN 978-87-550-3583-6

[8] Kim T, Hansen A M and Branner K 2013 Development of an anisotropic beam finite element for composite wind turbine blades in multibody system *Renewable Energy* **59** 172 ISSN 09601481, 18790682

[9] Larsen T J, Madsen H A, Larsen G C and Hansen K S 2013 Validation of the dynamic wake meander model for loads and power production in the egmond aan zee wind farm *Wind Energy* **16** 605–624 ISSN 10954244, 10991824

[10] Madsen Aagaard H, Mikkelsen R, Sørensen N, Hansen M, Øye S and Johansen J 2007 *Influence of wind shear on rotor aerodynamics, power and loads* pp 101–116 Denmark. Forskningscenter Risoe. Risoe-R-1611 ISBN 978-87-550-3610-9

[11] Beddoes T S 1987 A near wake dynamic model *proc. of the AHS national specialist meeting on aerodynamics and aeroacoustics*

[12] Madsen H A and Rasmussen F 2004 A near wake model for trailing vorticity compared with the blade element momentum theory *Wind Energy* **7** 325–341

[13] Hansen M H, Gaunaa M and Madsen H A 2004 *A Beddoes-Leishman type dynamic stall model in state-space and indicial formulations* (Roskilde, Denmark: Risø-R-1354)

[14] Hansen M H 2011 *Aeroelastic properties of backward swept blades* Proceedings of 49th AIAA Aerospace Sciences Meeting Including The New Horizons Forum and Aerospace Exposition, Orlando